COMPOSITIONAL RESERVOIR SIMULATION-BASED REACTIVE-TRANSPORT FORMULATIONS, WITH APPLICATION TO CO_2 STORAGE IN SANDSTONE AND ULTRAMAFIC FORMATIONS

A DISSERTATION
SUBMITTED TO THE DEPARTMENT OF
ENERGY RESOURCES ENGINEERING
AND THE COMMITTEE ON GRADUATE STUDIES
OF STANFORD UNIVERSITY
IN PARTIAL FULFILLMENT OF THE REQUIREMENTS
FOR THE DEGREE OF
DOCTOR OF PHILOSOPHY

Sara Forough Farshidi
April 2016

This dissertation is online at: http://purl.stanford.edu/zj896rk1447

I certify that I have read this dissertation and that, in my opinion, it is fully adequate in scope and quality as a dissertation for the degree of Doctor of Philosophy.

Louis Durlofsky, Primary Adviser

I certify that I have read this dissertation and that, in my opinion, it is fully adequate in scope and quality as a dissertation for the degree of Doctor of Philosophy.

Hamdi Tchelepi, Co-Adviser

I certify that I have read this dissertation and that, in my opinion, it is fully adequate in scope and quality as a dissertation for the degree of Doctor of Philosophy.

Kate Maher

Approved for the Stanford University Committee on Graduate Studies.

Patricia J. Gumport, Vice Provost for Graduate Education

This signature page was generated electronically upon submission of this dissertation in electronic format. An original signed hard copy of the signature page is on file in University Archives.

Abstract

Chemical reactions are important in many simulation applications, including geological carbon storage. The incorporation of chemical reaction treatment in general compositional reservoir simulators is thus necessary to enable this modeling. In this work, we develop robust numerical schemes for modeling CO_2 sequestration. All of the methods developed are implemented into Stanford's Automatic Differentiation-based General Purpose Research Simulator (AD-GPRS). We first address a special case of crossing thermodynamic phase boundaries, i.e., aqueous phase disappearance and reappearance in the context of CO_2 sequestration. A specialized treatment for handling aqueous-phase components when the aqueous phase disappears (or reappears) is introduced under the natural set of variables. This variable set includes pressure, phase saturations, and phase compositions. We demonstrate the robustness of our fully-implicit natural-variable formulation for carbon storage simulations, even when the aqueous phase disappears in multiple grid blocks.

We also propose a novel reactive transport formulation based on overall-composition variables. This formulation effectively treats the aqueous phase disappearance phenomenon, because the overall-composition variables are valid for all fluid-phase combinations. Overall-composition variables, however, suffer from the high cost of thermodynamic calculations in two-phase grid blocks. This motivates the development of a hybrid numerical scheme which takes advantage of the favorable features of both the natural and overall-composition variable formulations. Simulation results for CO_2 sequestration scenarios with the three formulations demonstrate the stability of these schemes. A comparison of the numerical performance of these treatments suggests that the use of natural variables in general offers enhanced computational efficiency compared to overall-composition variables. Under the natural-variable formulation,

however, one of the special treatments proposed in this work should be considered for grid blocks with single-phase gas.

We next investigate the use of ultramafic rocks for geological carbon storage. These rocks are highly reactive and offer considerable CO_2 storage capacity. We begin by analyzing a weathering system in this type of rock, where our AD-GPRS implementation is validated against field observations. We then simulate idealized carbon storage projects in an ultramafic reservoir. The general features and patterns of carbonation are identified and discussed. This type of rock offers nearly complete conversion of the injected CO_2 to mineral forms in many cases, enhancing storage security. Sensitivity analyses are conducted to examine the impact of various reservoir properties and operation parameters on carbonation efficiency. We demonstrate that well control scenarios can be designed to improve the carbonation process substantially by providing a more effective distribution of the injected CO_2 in the formation.

Acknowledgments

I would like to express my most sincere gratitude to my academic and research advisors Professor Louis J. Durlofsky and Professor Hamdi A. Tchelepi for their support, patience, encouragement, and guidance throughout the past few years. Their wisdom and broad view of science, along with attention to details made this a very outstanding experience. My advisors are my role models in ethics, professionalism, and devotion, and it is a great privilege to be their student.

Special thanks go to Dr. Denis Voskov for his endless support, ideas, and coaching throughout the past few years which contributed to this research work in many ways. I am also grateful to Professor Kate Maher, Dr. Mohammad Karimi-Fard, Pablo García del Real, and Dr. Huanquan Pan for the many helpful discussions on various aspects of this work. I thank my defense committee, Professors Kate Maher, Dennis Bird, and Adam Brandt, for their insight and feedback on this dissertation. I have had the privilege of having many mentors from whom I received most valuable teaching over the years. These include in addition to my advisors, Professors Franklin Orr, Anthony Kovscek, Margot Gerritsen, Khalid Aziz, Dennis Bird, Adam Brandt, and Roland Horne. I am very thankful to all the faculty, students and staff (teaching, research, and administrative) of the Department of Energy Resources Engineering for providing a challenging and efficient learning experience. The financial support provided by the industrial affiliates of the SUPRI-B Consortium, as well as the Global Climate and Energy Project (GCEP) at Stanford University, is gratefully acknowledged.

Through my years at Stanford, I have been fortunate to be surrounded by a wonderful group of friends and colleagues. In particular, I would like to thank my officemates Karine Levonyan, Christin Strandli, Priscila Ribeiro, Carla Co, Leticia Acquaviva,

and Sanghui Ahn for the endless support and the shared experience of challenge and failure. Also, out of my many special friends and colleagues at Stanford, of special mention are Amir Salehi, Mehrdad Gharib-Shirangi, Maryam Fathi, Michael Connolly, Orhun Aydin, Alireza Iranshahr, Rustem Zaydullin, Mohammad Shahvali, Mehrdad Honarkhah, Markus Buchgraber, Ekin Ozdogan, Golnaz Alipour, Amir Delgoshaie, Guillaume Moog, Ana Suarez, Khalid Alnoaimi, Boxiao Li, Abdulrahman Manea, Sumeet Trehan, Pablo García del Real, and Dana Thomas.

Many thanks go to my family for their love and support. I am grateful to my parents, Kazem Farshidi and Masoumeh Seraj, for teaching me values in life. Without their love and devotion I certainly would not be where I am today. I thank my brothers, Reza, Amin, and Ali, for their love and friendship. I dedicate this dissertation to my husband, Amir Shahbazi, for whose endless love, support, and encouragement throughout my academic career I am sincerely thankful.

Contents

List of Tables

List of Figures

Chapter 1

Introduction

Since the industrial revolution, a 45% increase in the level of atmospheric CO_2 has occurred. Concerns regarding the consequences of this rise in CO_2, e.g., global climate change, have motivated research targeting CO_2 emission reduction or elimination. Carbon capture and sequestration has also received significant attention as a means for greenhouse gas reduction [85]. To facilitate the modeling of CO_2 storage in geological formations, various flow simulators have been developed [e.g., 61, 95]. In this work we focus on the development of robust simulation capabilities for the problem of geological carbon storage in saline aquifers as well as ultramafic formations.

Reservoir simulation entails modeling multiphase flow in porous formations. It is used for performance forecasting as well as for optimization of subsurface operations. Conventional compositional simulators treat complex phase behavior and dynamic fluid properties, but do not typically include chemical reactions [e.g., 35, 18, 80, 133, 15]. However, the accurate and efficient coupling of flow and chemical reactions is essential for many subsurface flow processes of interest, so models for specific applications have been developed in recent years. Application areas include unconventional resource recovery and CO_2 sequestration [27, 117, 104, 85]. For example, the thermal in-situ conversion process for hydrocarbon extraction from oil shale entails heating the formation to high temperatures, which facilitates the decomposition of heavy hydrocarbon components to lighter components [34, 27]. Reaction modeling is also important for the long-term geological storage of carbon dioxide [83, 116]. This application area is the focus of this thesis.

In previous work within our group, Fan [26] incorporated reaction modeling into a fully-implicit compositional simulation framework. He developed a general fully-implicit, chemical reaction modeling capability based on natural variables, which was implemented into Stanford's General Purpose Research Simulator (GPRS). In [26, 27], this model was applied to the in-situ conversion of oil shale driven by downhole electrical heaters, while in [28] it was employed for chemical reaction modeling of geological carbon sequestration in saline aquifers.

The work presented in this dissertation extends the work of Fan et al. [28] in several important directions. Specifically, we present a treatment under the natural-variable formulation for aqueous phase disappearance, which can occur during CO_2 sequestration. Moreover, we devise and implement a novel reactive transport formulation based on overall-composition variables, which can also be employed as a means for handling aqueous phase disappearance. To our knowledge, this is the first such formulation developed. Modeling capabilities have also been implemented to address the variations of porosity, permeability, and mineral reactive surface areas due to mineral dissolution and precipitation. These comprehensive treatments have been incorporated into the latest version of Stanford's Automatic Differentiation-based General Purpose Research Simulator (AD-GPRS). Our implementation is compatible with most of the capabilities that currently exist in this state-of-the-art compositional simulator, which include advanced well models, high-performance linear solvers, and the ability to use unstructured grids.

1.1 Literature review

The reaction paths observed during CO_2 sequestration in saline aquifers are similar to the ones experienced in natural weathering systems. In these systems, silicates act as a source of alkaline and alkaline-earth metal ions in aqueous solutions, which can react with dissolved CO_2 to form carbonates. The many aspects involved in the modeling of geological carbon storage have been addressed within different branches of science and engineering. In this section we elaborate on relevant previous work aimed at reaction modeling, multiphase flow simulation, and investigating the natural weathering processes in ultramafic rocks.

We begin with an introduction to reaction modeling and its integration into various flow and transport simulators. We then briefly review the reactive transport simulators developed by the groundwater flow and reservoir engineering communities. We follow with an overview of the different formulations used by the reservoir engineering community, namely the natural- and mass-variable formulations. We then discuss ultramafic rocks and explore their potential as host rocks for carbon storage.

1.1.1 Reaction modeling

Chemical reactions represent source/sink phenomena that contribute to component mass distributions. The reaction terms appearing in the mass balance equations involve, in general, reaction rates and stoichiometry coefficients for individual components. They introduce additional coupling and significant nonlinearity as the reaction rates are nonlinear functions of pressure, temperature and phase compositions [33]. Reactions which occur over time scales that are very different from other phenomena, e.g., saturation changes, result in a stiff system of equations. Such systems require the use of extremely small time steps. As a remedy, reactions that are sufficiently fast (relative to other effects) and reversible are treated as equilibrium reactions, i.e., they are assumed to reach chemical equilibrium instantaneously.

Equilibrium reactions

Equilibrium reactions are modeled through the law of mass action, which is usually represented by an algebraic relation among reactants and products and is consistent with minimizing Gibbs free energy. By definition, and in this limit, the reactions in both the forward and reverse directions are driven by changes in the equilibrium caused by additional phenomena, e.g., transport or other (kinetic) reactions [65, 86, 29]. This treatment is similar to the phase equilibrium assumption in reservoir simulators, where instantaneous thermodynamic equilibrium is imposed within grid blocks.

A substantial amount of work has been performed in the groundwater community to model equilibrium reactions. The fundamental idea is that mass balance equations should now be written in terms of the mass of entities that are conserved under

equilibrium reactions. The most basic such choice is the set of constituent chemical elements, which are in fact conserved under both kinetic and equilibrium reactions [26]. Historically, the groundwater community has followed a slightly different path, however, classifying species into primary and secondary sets, as we now describe.

Primary and secondary species

Each equilibrium reaction imposes a local constraint on the mathematical system. This provides a means to eliminate one unknown species concentration and its corresponding mass balance equation. As a result, the number of equations solved simultaneously for each grid block is reduced by the number of equilibrium reactions. This idea has been widely adopted and nearly all reactive transport simulators employ it, relying on the concept of primary species [65], also known as components [77], tenads [98] and reaction invariants [7], versus secondary species (noncomponents).

The primary species are by definition conserved under equilibrium reactions and may be defined as linear combinations of the physical species that fulfill this requirement. The choice of primary species is hence not unique. Once a set is specified, any (linearly-independent) linear combination is also a valid set of primary species. It is important to note that this is different from the primary and secondary variable concept in compositional reservoir simulators used to decouple local equations (at the level of the Jacobian matrix) in order to reduce the size of the global linear system. The concepts are related, however, in that fixing a smaller subset of variables can fully define the intensive and extensive state of the system.

Many groundwater codes are formulated based on the primary and secondary sets of variables described above. But, since existing compositional reservoir simulators are based upon physical species mass balances, in order to facilitate the efficient implementation of chemical reaction modeling, a slightly different approach for treating equilibrium reactions has been proposed in this community [28, 79]. Instead of defining equilibrium reaction invariant components, the mass balance equations are developed for physical species. A linear transformation is then applied to these equations, which yields a linear combination that is free of the impact of the equilibrium reactions. A more detailed discussion of this procedure will be given in Chapter 2.

Note that this approach yields the same system of equations as in groundwater formulations if equivalent linear combinations are used.

Terminology in groundwater and reservoir simulation

Terminology can be a source of confusion between the fields of groundwater flow and reservoir engineering, so it is worthwhile to carefully define terms. In the groundwater community, molecules with the same chemical identity are usually considered different species when in different fluid phases, whereas in reservoir engineering molecules with the same chemical identity in different phases are viewed as the same species. Moreover, phase equilibrium constraints are usually categorized as equilibrium reactions in the groundwater field [10, 131, 110].

Every mineral species is generally viewed as a phase in the groundwater geochemistry literature, whereas the concept of a mineral phase is not widely utilized in the reservoir engineering literature. In geochemistry settings, minerals are classified into two groups – primary and secondary. Primary minerals are those that were integrated into the igneous rock during the primary crystallization. Secondary minerals result from the subsequent weathering or hydrothermal alteration of the original minerals [59].

1.1.2 Groundwater flow simulators

As noted above, chemical reaction modeling has been addressed by both the reservoir simulation community and the groundwater flow/hydrogeology community. Developments in these areas proceeded somewhat independently and different physical effects have been emphasized by the two communities. As a result, a particular effect may be treated rigorously in one simulator, yet handled loosely or completely ignored in other simulators. In this section, a brief description of the simulators developed in the groundwater field is given. The related work in the reservoir simulation community will be discussed in the following section.

In the groundwater-based work, the numerical modeling of coupled multicomponent transport and reactions dates back to the mid-1980s, when the basic theory of the

continuum model for reactive transport was developed [65]. Numerous groundwater simulators emerged and continue to evolve [112], including HYDROGEOCHEM [132], TOUGHREACT [131], MIN3P [74], PFLOTRAN [67, 42], and CrunchFlow [110]. These codes have been used widely in research on contaminant migration and nutrient flux [108, 111, 124]. Modeling the coupled geochemical reactions and flow and transport in the near-well region has also gained interest, partially to address problems related to formation dry-out and undesired scaling or clay swelling [93].

TOUGHREACT, developed at Lawrence Berkeley National Laboratory, is a thermal multicomponent reactive transport code built upon TOUGH2 [131, 94, 129, 130]. It has been employed extensively for modeling the subsurface interactions of gas, mineral and water phases. A sequential iteration scheme is employed, which entails (1) finding the solution of the thermal multiphase flow equations to yield phase velocities and saturations, (2) using these updated values to calculate the aqueous component concentrations and gaseous component partial pressures, one component at a time, and (3) resolving the chemical reaction equations on a block-by-block basis. CrunchFlow [110] is another multicomponent reactive-flow software package. It allows for the fully-implicit treatment of one- or two-dimensional cases, though it does not treat multiphase flow.

PFLOTRAN, developed by Lichtner et al. [67], is a massively parallel thermal flow and transport model. The model is applicable for only a limited number of multicomponent multiphase flow scenarios, but it does include a fully-implicit formulation. Phase properties are either constant or calculated based on simple models. For the CO_2 phase, properties such as density, viscosity, and fugacity are read from a table derived from the Span-Wagner equation of state [106]. The treatment for phase behavior is based on Henry's law relations using these tabular values.

Numerical schemes

The groundwater and hydrogeology simulators often rely on the sequential iteration approach (SIA), or iterative operator splitting, where transport and reaction processes are treated separately [131, 109]. This allows these formulations to handle a large number of components. Lower memory requirements and greater speed at a given

time step are among the advantages of SIA over the fully-implicit scheme (though SIA may require smaller time steps, as discussed below). Other advantages of SIA are its lower numerical dispersion and the ease with which more accurate (and more complex) discretization techniques can be implemented.

These explicit approaches are, however, limited in terms of the Courant condition (CFL number) [21], which can significantly limit time step size. As a result, simulation of certain phenomena, such as water-rock interactions over geological time scales, may entail long computation times, especially in heterogeneous formations. In such cases, the fully-implicit approach is generally preferred. A potentially more significant issue with SIA is that it may suffer from a lack of convergence. This has prompted some work on the sequential noniterative approach (SNIA), which does nonetheless introduce splitting errors [109, 25]. Alternatively, a selective coupling approach, which is a hybrid of SIA and fully-implicit methods, has been investigated [96]. This approach improves SIA convergence by considering weak and strong coupling between the equations, and treating the higher levels of coupling implicitly [96].

A fully-implicit (FIM) solution is more difficult to implement, since it requires derivatives of all equations with respect to all unknown variables. It can be very demanding in terms of computation time per time step as well as memory requirements, especially for systems with large numbers of components. Yet it has been shown that when utilizing an efficient sparse direct solver (UMFPACK [22]), FIM is more efficient than both SIA and SNIA, even for a large number of unknowns and for relatively simple reaction systems [25]. This is primarily because FIM avoids stability issues and can take larger time steps [110, 15].

Advantages and limitations of groundwater simulators

A feature of some groundwater codes is the implicit assumption of constant fugacity gases and the use of simple models for the transfer/dissolution of species from one fluid phase to another [10]. For example, in some cases a unit fugacity coefficient is used under the assumption of ideal gases. In contrast, in compositional reservoir simulation, detailed treatment of the phase behavior, potentially through a cubic equation of state, is typically used.

While reservoir simulators are typically limited in terms of the types of reactions they treat, groundwater simulators often handle a wide range of thermo-physical-chemical processes. These may include, for example, aqueous complexation, acid-base, redox, gas dissolution/exsolution, cation exchange, surface complexation, and mineral dissolution and precipitation reactions [128]. The effect of reactions on porosity and permeability are modeled in most groundwater codes, and mineral surface area is also usually updated [126, 110, 112].

In most groundwater simulators, water is assumed to be the dominant species, with the aqueous phase present at all times. General (hydrocarbon) phase behavior, multiphase flow, and phase properties are often not treated in the detail required for reservoir modeling applications. In addition, in groundwater flow systems, some effects can be treated explicitly, or in a decoupled manner, while analogous effects in reservoir simulation would commonly be treated fully-implicitly. Thus, although great advances in reactive-transport modeling have been made in the groundwater community, the resulting models may not always be directly applicable for general purpose reservoir simulation.

1.1.3 Reaction treatment in reservoir simulators

In the context of reservoir simulation, reactive transport formulations have been applied to the modeling of unconventional resource recovery processes as well as CO_2 storage [78, 11, 32, 97, 69]. Examples include Stanford's General Purpose Research Simulator (GPRS) [26, 27, 28], UTCHEM [1], and the commercial simulators STARS and GEM developed by the Computer Modelling Group [2, 79].

The GPRS software package includes a three-dimensional, fully-implicit general treatment for kinetic and equilibrium reactions based on element balances. This implementation is discussed in detail in Chapter 2. The GPRS model allows for a combination of homogeneous and heterogeneous reactions among any number of components [26, 27, 28].

STARS is a generalized thermal-compositional simulator based on K-values and coupled with kinetic reaction treatment. Among other applications, it has been used for

modeling in-situ shale upgrading [117]. The implementation in GEM is similar to that in GPRS. It includes a fully-implicit treatment based on generalized equations of state, along with the treatment of kinetic as well as equilibrium reactions. The reaction modeling includes asphaltene precipitation and geological CO_2 sequestration. This package thus does not offer a fully flexible reaction modeling capability that can be used with arbitrary reaction systems, e.g., reactions in hydrocarbon systems are not modeled [79].

UTCHEM [1] is a three-dimensional simulator with a relatively complete treatment of chemical reactions within a multiphase flow setting. However, the coupling between the chemical reactions and transport is treated through a sequential iterative approach, with pressure handled implicitly [90]. Chemical reactions are then solved locally, after which concentrations are updated. This model can therefore encounter stability problems, which leads to very small time steps in cases with tight coupling and high degrees of nonlinearity [109, 99, 30, 43].

1.1.4 Nonlinear formulations in reservoir simulation

In reservoir simulation, energy and species mass conservation equations are coupled with thermodynamic equilibrium and other constraints to solve the problem of interest. Newton's method is usually applied to solve the resulting set of nonlinear equations. Strong nonlinearities and multiscale issues are common in reservoir engineering problems. Fluid phases may appear and disappear, which can also lead to numerical challenges with some formulations. Several different solution techniques have been developed, as we now describe.

Thermodynamic arguments based on Gibbs phase rule and Duhem's theorem prove that fixing a limited number of grid-block unknowns will suffice to fully define both the intensive and extensive state in each block. In thermal scenarios, the number of required unknowns is equal to the number of components (n_c) plus one, while in isothermal settings n_c unknowns are required. Partitioning the equations and variables into primary and secondary sets based on this observation is common practice. The global component mass balances are used as the primary set of equations, and

these are solved simultaneously (for all blocks). Various choices for the primary variables exist, and these yield different schemes with varying performance for particular problems.

Two main groups of solution techniques are the so-called natural- and mass-variable formulations. Variable decoupling is accomplished algebraically (through a Schur complement) in the natural-variable formulation, though it is more complicated in the mass-variable formulation. This impacts the computational time requirements. A brief discussion of these two procedures for isothermal systems is given below. These approaches will be discussed in detail in Chapters 2 and 3.

Natural- versus mass-variable formulations

The natural-variable formulation was first introduced by Coats [18]. Variables in this approach consist of phase pressures, phase saturations, and phase compositions. The governing equations are written (directly) in terms of these variables, which makes the construction of the Jacobian matrix efficient and straightforward. Also, the phase behavior computations can be performed very efficiently for blocks with the maximum number of phases present.

Several formulations based on mass variables have been presented. Fussell and Fussell [35] proposed, as the variable set, pressure, phase fractions, overall compositions, and the phase compositions from one fluid phase. The choice of phase compositions depends on the phase fraction values; any fluid phase that contains more than half of the overall component moles will have its mass fractions used as variables.

A subsequent formulation by Young and Stephenson [133] used pressure, phase fractions, overall compositions, and the gas phase compositions. This formulation treats an arbitrary number of components in hydrocarbon phases, but only water in the water phase. A modification proposed by Chien et al. [17] replaced the gas phase compositions with the phase equilibrium ratios, i.e., K-values. This was further modified by Wang et al. [121] to use the natural logarithm of the K-values in order to render the phase equilibrium constraints less nonlinear.

A major drawback of the formulations discussed above is the need for adaptive variable/equation selection, i.e., variable switching. The number and choice of variables and equations changes upon phase appearance or disappearance, which leads to code complexity. The overall-composition formulation avoids variable switching by using pressure and overall compositions as the variables of choice. In this model, the thermodynamic constraints are considered at convergence at all Newton iterations [119, 20]. After solving for the pressure and overall compositions, a stability test determines the number of fluid phases. If more than one phase is detected, a flash calculation follows. Note that all other formulations discussed thus far avoid the flash calculation for grid blocks that continue to remain in the two-phase state; this is achieved by explicitly tracking either saturations or phase fractions.

Alternatively, the work of Acs et al. [3] employed a volume balance formulation that used the extensive molar variables instead of overall compositions. Consequently, the constraint that the overall compositions should sum to one was replaced by a volume balance based on extensive molar variables, which requires that the fluid fills the pore volume. This work was later modified from an IMPES scheme to a sequential implicit procedure by Watts [122].

While several of the earlier mass variable-based formulations discussed so far have employed mixed-implicit treatment, e.g., IMPES, in this work we consider only fully-implicit treatments of reactive transport under both the natural- and mass-variable formulations. The stability and larger time steps associated with the FIM approach are desirable for the highly nonlinear systems that arise in many reservoir simulation applications.

Comparing the performance of various formulations

Stanford's General Purpose Research Simulator (GPRS), originally developed by Cao [15] and later extended by Jiang [50] and Fan [26], among others, enables the comparison of different formulations in a single simulator. The basic implementation is a natural-variable formulation, and a transformation matrix is used to relate any user-defined variable set to the natural variables. The Jacobian matrix is updated in terms of the new variables using the transformation matrix and the chain rule. Comparisons

are thus possible at the linear level only. Additionally, this transformation introduces numerical difficulties, especially in challenging nonlinear problems, such as those with phase disappearance/reappearance, and near-miscible displacements.

A new version of GPRS based on the automatic differentiation of the general residual equations, AD-GPRS, has since been developed at Stanford University [135, 134, 120]. Using AD-GPRS, the performance of several fully-implicit formulations has been compared for challenging multiphase multicomponent problems [119]. These formulations were analyzed under miscible and immiscible gas displacement scenarios for different CFL numbers and nonlinear solution techniques. It was observed that, for isothermal compositional problems and under appropriate variable updating strategies, the natural-variable formulation has advantages over the mass-variable formulations. This is primarily due to the fact that the nonlinear behavior in the scenarios considered was captured most readily in terms of fluid saturations. Also, the overall-composition formulation consistently experienced the highest thermodynamic equilibrium calculation costs. This was expected since this model requires flash calculations at all Newton iterations and for all the two-phase blocks.

1.1.5 Ultramafic rocks: application to CO_2 storage

An important application in reactive transport modeling is the simulation of CO_2 storage operations. Most previous work has focused on carbon sequestration in sandstone aquifers. The rocks forming these reservoirs, however, offer little potential for CO_2 mineralization due to their low reactivity. Ultramafic rocks, discussed in detail below, have been investigated recently as a better candidate for the safe, long-term storage of CO_2 in the form of solids [53, 54, 88, 36, 37, 51].

Best minerals for carbonation

Earth's crust is mainly composed of silicate minerals in various types of rocks. In natural systems, the reaction of calcium, magnesium, and iron silicates with dissolved CO_2 leads to the formation of calcium, magnesium, and iron carbonate minerals. This process has been a very strong natural CO_2 storage and regulation mechanism over geological time scales. In fact, the total mass of atmospheric carbon today is about

800 Gt, while around 39,000,000 Gt of carbon is stored in carbonate rocks in the Earth's crust [85].

Rocks are classified into three general types: igneous, sedimentary, and metamorphic. Igneous rocks form from the cooling of magma or lava, and can be subdivided based on their chemical properties into felsic, intermediate, mafic, and ultramafic rocks. Felsic (roughly the same as acid) rocks contain more than 63 wt% SiO_2. The SiO_2 content decreases successively through the categories, with ultramafic rocks having less than a 45 wt% content. Felsic rocks are abundant in the lighter elements such as silicon, oxygen, aluminum, sodium, and potassium. In other words, they are dominated by feldspar ($KAlSi_3O_8$-$NaAlSi_3O_8$-$CaAl_2Si_2O_8$) and quartz (SiO_2). In contrast, mafic rocks/minerals (roughly the same as basic) are ferromagnesian, i.e., they are rich in iron and magnesium.

The best candidates for CO_2 mineralization are mafic silicate minerals rich in Mg and Ca, and low in Na and K. Due to their high molar ratio of divalent cations, these minerals have the greatest potential to fix CO_2. The kinetics are also generally faster than in other minerals. Another key advantage of these rocks is their abundance. In fact, it is speculated that they may be capable of binding all fossil fuel-related carbon [85]. Olivine ($(Mg, Fe)_2\,SiO_4$) is the best candidate identified thus far. Other options are serpentine (e.g., chrysotile $Mg_3Si_2O_5(OH)_4$), pyroxenes (e.g., enstatite $MgSiO_3$), plagioclase, and basaltic glass [54].

Mineralization in saline aquifers

Saline aquifers in sedimentary basins have been frequently considered for CO_2 storage due to their potentially high porosity and permeability, as well as their wide distribution geographically. The total saline aquifer pore volume storage capacity is also much higher than other options, such as depleted oil and gas reservoirs. These aquifers consist of sandstones, siltstones, shale, and limestone, and they contain only small amounts of mafic silicate minerals. Consequently, in many sedimentary basins, the major CO_2 storage mechanisms are not mineralization but rather structural, residual, and solubility trapping [73, 127]. Carbonation is only attainable under specific sandstone mineral compositions, and even then it occurs to only a limited extent over

geological time scales. Field measurements have verified modest degrees of mineralization in sandstone settings [40, 57, 41].

Mafic mineral-bearing rocks

The Earth's mantle is composed of ultramafic rocks, which commonly have more than 90% mafic mineral content. They are igneous and meta-igneous (metamorphosed igneous) rocks containing less than 45 wt% SiO_2, and usually more than 18% MgO, high FeO and low potassium content. Peridotite, an ultramafic rock, signifies a rock type rich in the mineral olivine. Olivine is a magnesium iron silicate mineral, $(Mg, Fe)_2\,SiO_4$, with the two endmembers forsterite (Mg endmember: Mg_2SiO_4) and fayalite (Fe endmember: Fe_2SiO_4). The upper mantle consists of mostly olivine and pyroxene (e.g., enstatite $MgSiO_3$). Tectonically exposed mantle peridotite typically contains 70-85% olivine. These minerals are however unstable on the Earth's surface and usually experience at least partial hydration and/or carbonation, which involve conversion to serpentinite and carbonate minerals. Many tectonically emplaced mantle peridotites are for the most part altered to serpentine.

Rocks containing mafic minerals include basalts and peridotites. Basalts exist in the upper igneous layer in the oceanic crust, as well as in many continental accumulations [73], though they cover less than 10% of continental surfaces [85]. Ultramafic rocks, e.g., peridotites, are less dominant, but are still accessible. The largest peridotite volumes are located in Sultanate of Oman (350×40 km^2), New Caledonia (150×40 km^2), Papua New Guinea (200×50 km^2), and along the eastern edge of the Adriatic Sea (several 100×40 km^2 massifs) [73].

While basalts have higher permeability and porosity compared to peridotites, they offer a lower carbonation rate and capacity due to their mineral composition, as plagioclase ($NaAlSi_3O_8$-$CaAl_2Si_2O_8$) is the main constituent of basalt. In general, magnesium and calcium silicates have similar molar abundance in the Earth's crust. The magnesium-bearing silicates, however, have significant MgO concentration, up to 50 wt%, which yields a high theoretical CO_2 storage capacity. For example, 0.6 kg of aqueous CO_2 will react with 1 kg of forsterite to yield 1.6 kg magnesite ($MgCO_3$)

and quartz (SiO_2), based on the following reaction:

$$Mg_2SiO_4 + 2\,CO_2 \longrightarrow 2\,MgCO_3 + SiO_2. \tag{1.1}$$

In contrast, rocks such as basalt, containing Ca-bearing minerals, have a CaO concentration of 10 wt%, corresponding to consumption of 0.08 kg of CO_2 per 1 kg of rock [85]. Additionally, recent advances in hydraulic fracturing may offer a means of achieving sufficient permeability and injectivity in inherently low permeability and porosity rocks such as peridotites. These technologies are currently being deployed in other applications with similar complications; e.g., enhanced geothermal systems [75], so their application for CO_2 storage may be plausible.

To gain insight into the capacity offered by ultramafic rocks, we consider the Samail Ophiolite in Oman, which is a thrust-bounded slice of oceanic crust and upper mantle. This massif is about 350 km×40 km, with an average thickness of about 5 km, 30% of which consists of mantle peridotite [81]. For present purposes we consider forsterite (Mg_2SiO_4), the Mg endmember of olivine, as the main constituent of this peridotite. The addition of 1 wt% CO_2 to this massif amounts to 25% of all atmospheric CO_2, which is comparable to all of the additional CO_2 emitted into the atmosphere since the industrial revolution. If all Mg cations are converted to carbonates, some 7000 Gt of CO_2 will have been stored in solid form [53].

Reaction paths in ultramafic rocks

The reaction paths experienced during geological CO_2 storage are similar to those describing natural weathering of silicate. As a result, studying these natural analogs is directly relevant to forecasting the outcome of sequestration processes. We now discuss these reactions paths in ultramafic rocks.

The hydration and carbonation processes involving the interactions of water and CO_2 with silicates such as forsterite, enstatite (a pyroxene endmember), and serpentine (hydrated olivine), are thermodynamically favored at low temperatures [53, 85, 63, 62, 102]. The density difference between reactants and products of the hydration

and carbonation reactions results in an increase in solid volume. For example, carbonation of the main constituent of peridotite, olivine, results in (Mg,Fe)CO_3 (with endmembers magnesite and siderite), and is accompanied by about 44% volume increase for the magnesium endmember under isothermal conditions [53]. Similarly, solid volume also increases during hydration as the mineral converts to serpentine ($(Mg,Fe)_3Si_2O_5(OH)_4$), i.e., during serpentinization.

Implications of change in solid volume

There is much debate around the effect of this volume change, even in cases of natural weathering analogs of peridotites. Replacing minerals in the host rock by lower density minerals causes an increase in the solid volume. This may fill porosity and diminish reactive surface area and permeability due to plugging, as is observed in some lab experiments. For example, a decrease in permeability was observed following hydration and carbonation of basalt in [9]. Also, in a carbonation experiment on a natural peridotite sample, 50% of the porosity was plugged after 10% progress in carbonation [47]. Thus these reaction phenomena have been deemed by many researchers to be self-limiting [24, 127].

This, however, contradicts many observations in nature. Specifically, complete conversion of extensive outcrops of peridotite to serpentine or carbonates (listwanites) has been observed in many natural analogs around the world [36, 53]. Furthermore, alternative experimental data for carbonation of peridotites have indicated an increase in permeability despite increasing solid volume [5]. Macdonald and Fyfe [70] proposed that during olivine hydration, and in an elastically confined volume, the increase in stress due to volume increase causes fractures. These fractures introduce new surface area and increase permeability, creating a positive feedback in the overall process.

This idea has been investigated by various researchers, and it has been suggested that carbonation and hydration of olivine at shallow depths can cause enough stress to generate rock deformation. Microstructural observations, e.g., pervasive dense fracture networks with serpentine veins in peridotite host rocks, support this reaction-driven cracking hypothesis [52]. Also, repeated cycles of fracturing followed by hydration

are proposed as the reason for several generations of cross-cutting serpentine veins observed in nature [49]. Many carbonated outcrops also display hierarchical fracture networks down to the microscopic scale [54]. Because the pervasive fracture networks observed in carbonates and serpentines are not present in unaltered peridotite, and are inconsistent with tectonically induced deformations, they are considered a direct result of carbonation and hydration [55, 38, 36]. Examples of altered peridotite are shown in Fig. 1.1 [38].

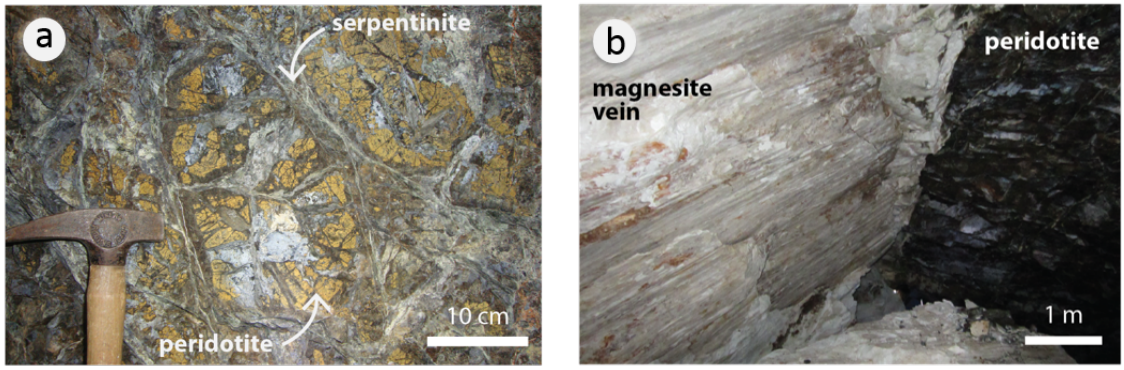

(a) A variably serpentinized peridotite (b) An example of carbonated peridotite

Figure 1.1: Examples of alteration in ultramafic rocks. In (a) the serpentine veins are evident. In (b), a massive magnesite vein, the white block on the left, is in contact with the (dark) peridotite on the right (Red Mountain magnesite mine, California). Photographs from the Del Puerto Ophiolite, California; reprinted from García del Real and Vishal [38].

In some lab experiments, however (e.g., [47]), no evidence of reaction-driven cracking was observed, and the carbonation process was again deemed to be self-limiting. This observation has prompted the idea that reactive fracturing may be more likely to occur during faster carbonation, and absent in the case of slower reactions. The reasoning is that during slower reactions, the increased stress caused by precipitation is countered by relaxation mechanisms such as the viscous deformation of the carbonate. This discrepancy has been observed experimentally in rapid versus slow crystallization of salt in porous media [68]. In any event, the issue of reaction-induced fracturing is clearly very complicated, and it will require additional research to resolve.

Mineral surface area alterations

Our final consideration in peridotite carbonation is the evolution of the mineral surface area. The secondary minerals, e.g., carbonates or forms of silica, may form on the surface of the primary silicate mineral. This could inhibit dissolution by reducing the surface area available for reaction. Boundaries have been observed in many experiments of peridotite carbonation between the host unreacted mineral and the fluid in the pore space [114, 13, 51]. This phenomenon is also supported by theory [4]. The effects of this layer are variable, however, and depend on the specific precipitation mechanism [47, 51].

1.2 Scope of work

In this thesis, we implement, analyze, and enhance chemical reaction treatments in AD-GPRS. We will apply our new treatments to carbon sequestration in saline aquifers. CO_2 storage in ultramafic formations will also be investigated in detail.

The key research goals of this work are as follows:

- Develop robust formulations for CO_2 storage problems. The detailed treatment of aqueous phase disappearance, which commonly occurs near the injection well, will be integrated into a fully-implicit natural-variable-based scheme.

- Establish a treatment that can be used under any fluid phase combination, namely the overall-composition formulation. Advantages and drawbacks of this treatment relative to the natural-variable formulations will be demonstrated through several numerical examples.s

- Develop a hybrid of the natural- and overall-composition variable formulations. The natural set of variables is used unless the water phase is absent, in which case mass variables are employed. We describe this hybrid formulation such that its integration into an existing natural variables-based simulator requires relatively minor modifications.

- Examine the effectiveness of the three formulations in treating various complications characteristic of CO_2 sequestration scenarios. The numerical performance of these schemes will be compared for a few case studies.

- Employ our implementation to analyze a natural analog in peridotites of Samail Ophiolite in Oman, using the work in [88] as a reference. This will enable validation of our implementation against field data.

- Forecast the outcome of carbon storage in ultramafic rocks, and examine storage security. Conduct a sensitivity analysis with respect to various formation properties and operation criteria. This will yield insight into the key design parameters of a storage project in an ultramafic setting.

1.3 Dissertation outline

This dissertation proceeds as follows. In Chapter 2 we present the governing equations for reactive transport in porous media. A detailed discussion of how an existing compositional reservoir simulator can be modified to account for chemical reaction phenomena is provided. Treatment of both equilibrium and kinetic reactions will be described for an arbitrary system of components and reactions in a fully-implicit setting. The formulation uses natural variables and the implications of this choice are discussed. A treatment is introduced for handling aqueous-phase components when the aqueous phase disappears or reappears in the natural-variable formulation. Our approach entails the use of a kinetic model for tracking this so-called 'deposited phase.' Our new treatment for aqueous-phase components is first demonstrated using a very simple single-cell model. We then assess convergence behavior for a one-dimensional model. Finally, we present simulation results for a three-dimensional (40,000-cell) CO_2 storage model involving 12 components.

In Chapter 3 the reactive-transport problem is posed in terms of overall-composition formulation variables. This approach employs pressure and overall component mass fractions as the variables. Since the mass conservation equations involve phase compositions, this choice of variables introduces additional complexity in the Jacobian matrix manipulations [17, 119]. A full description of the simulation approach based on

this variable set, along with the steps necessary to account for both kinetic and equilibrium reactions, is provided. We discuss the advantages and drawbacks of this method relative to the natural-variable formulation, both in general and for the problem of CO_2 sequestration (specifically in the context of aqueous phase disappearance). Subsequently, a hybrid formulation is proposed which is equivalent to the natural-variable formulation, except that it accommodates water phase disappearance by switching to overall-composition variables, thus rendering deposition modeling unnecessary. A detailed comparison of the numerical performance of the three formulations is then presented.

In Chapter 4 we develop a reaction model for CO_2 mineralization in ultramafic rocks. This model includes 13 fluid components and ten solid phases, along with five equilibrium and ten kinetic reactions. Our implementation is validated against a natural weathering analog in peridotites. We then forecast mineralization results for geological CO_2 storage in this type of rock. A sensitivity study is conducted to assess the impact of various parameters in a field-scale carbon storage project. These parameters include pressure and temperature, which are defined by the choice of reservoir location and depth, and permeability and porosity, which can potentially be influenced by hydraulic fracturing or other reservoir stimulation procedures. We also consider different engineering strategies for designing and managing such a storage operation.

In Chapter 5, we summarize our findings and draw conclusions. Recommendations for future work in this general area are then provided.

In Appendix A, we introduce basic aspects of reaction modeling, including treatment of reaction sets. The discussion covers concepts commonly encountered in geochemical setups. Finally, in Appendix B we discuss techniques for modeling porosity and permeability change.

Chapter 2

Natural-Variable Formulation

Geological storage of CO_2 involves the injection of supercritical CO_2 into brine. The modeling is complicated by brine-rock chemical interactions. Injecting carbon dioxide into a saline aquifer leads to the dissolution of CO_2 into the brine, increasing water acidity. This change in water pH promotes mineral precipitation/dissolution. Silicates dissolve in brine, providing cations, which along with the dissolved CO_2 precipitate as carbonate minerals. Although carbonates are thermodynamically favorable compared to silicates, the process of dissolution/precipitation is governed by very slow kinetics. On the other hand, homogeneous reactions involving only aqueous components reach chemical equilibrium quickly, and can thus be treated as equilibrium reactions.

A robust reactive transport model using natural variables was developed by Fan et al. [28], and implemented into Stanford's existing compositional simulator, General Purpose Research Simulator (GPRS), as described in Sections 2.1.1-2.1.5. In the present work, this formulation was integrated in Stanford's Automatic Differentiation-based General Purpose Research Simulator (AD-GPRS) to facilitate further development. A key complication treated in this work is the fate of aqueous components when the aqueous phase disappears or reappears.

While the discussion in this chapter is comprehensive, additional details may be found in Appendices A and B. In Appendix A, we briefly introduce the basics of our reaction treatment, and further elaborate on reactive-transport modeling techniques including the concepts employed by the geochemistry community. In Appendix B, we propose

methodologies for the modeling of permeability and porosity variations resulting from mineral dissolution and precipitation.

The work presented in this chapter has been previously published in Farshidi et al. [31].

2.1 Generalized chemical-compositional framework

In this section we present the equations governing reactive flow and transport and then describe details of the numerical treatments. These include reduction of the full set of equations to a system of primary equations and variables, and our treatment of aqueous species in blocks where the aqueous phase disappears. This formulation can be viewed as an extension of existing compositional simulation capabilities. Compositional reservoir simulators have been presented by many investigators; see, e.g., [35, 18, 80, 133, 15, 48, 118, 119]. In the following, we use the terms components and species interchangeably. Both terms are used to denote physical species as opposed to geochemistry components.

2.1.1 Governing equations

The full set of governing equations for chemical-compositional modeling includes statements of mass conservation, chemical reaction equations, fugacity equalities, and other constraints. Phase equilibrium is assumed among all the fluid phases. We consider a system of n_f fluid species and n_m solid species. A fluid species may be a hydrocarbon component, or pseudo-component, an inorganic gas component, an ion, water, or a dissolved solid species. A solid species refers to a mineral component or an adsorbed fluid species that is immobile, for instance adsorbed cations (e.g., Ca^{2+}) on the rock surface.

The general mass conservation equations for fluid species i and solid species m are

(adapted from [109, 64]):

$$\frac{\partial}{\partial t}\left(\sum_{j=1}^{n_p}(\phi\rho_j S_j X_{ij})\right) + \nabla\cdot\mathbf{L} + q_i^W = \sum_{k=1}^{n_k}\upsilon_{ik}r_k + \sum_{q=1}^{n_q}\upsilon_{iq}r_q, \tag{2.1}$$

$$\frac{\partial C_m}{\partial t} = \sum_{k=1}^{n_k}\upsilon_{mk}r_k + \sum_{q=1}^{n_q}\upsilon_{mq}r_q, \tag{2.2}$$

where,

$$\mathbf{L} = \sum_{j=1}^{n_p}\left(\rho_j X_{ij}\mathbf{u}_j - \rho_j\phi S_j\mathbf{D}_{ij}\nabla X_{ij}\right). \tag{2.3}$$

In these equations, t is time, n_p is the number of fluid phases, ϕ is porosity, ρ_j is the density of fluid phase j, S_j is the saturation of phase j, X_{ij} is the molar fraction of fluid component i in phase j, $\mathbf{u}_j$ is the Darcy velocity of phase j (defined below), $\mathbf{D}_{ij}$ is the dispersion tensor for component i in fluid-phase j, q_i^W is the well rate of component i, C_m is solid species concentration, υ_{ik} are the stoichiometric coefficients of component i in kinetic reaction k, υ_{iq} are the stoichiometric coefficients in equilibrium reaction q, r_k and r_q are the rates of kinetic reaction k or equilibrium reaction q, respectively, and n_k and n_q are the numbers of kinetic and equilibrium reactions. We designate the total number of reactions as n_r, where $n_r = n_k + n_q$, and the total number of species as n_s, where $n_s = n_f + n_m$.

The Darcy velocity for phase j is given by:

$$\mathbf{u}_j = -\mathbf{k}\frac{k_{rj}}{\mu_j}(\nabla p_j - \rho_j g\nabla D), \quad j = 1,\cdots,n_p, \tag{2.4}$$

where $\mathbf{k}$ is the permeability tensor, k_{rj} is the relative permeability for phase j, μ_j is the viscosity of phase j, p_j is the pressure of phase j, g is gravitational acceleration and D is depth. We use the natural variable set [19], expanded to include solid species. The unknown variables are thus p_j, S_j, X_{ij}, and C_m. If more than one fluid phase is present, the gas phase pressure, p_g, is treated as a primary unknown, and the pressures of the other fluid phases (oil and water) are eliminated through use of capillary pressure relations, $p_o = p_g - P_{c,go}$ and $p_w = p_g - P_{c,go} - P_{c,ow}$. Here $P_{c,go}$

and $P_{c,ow}$ are gas-oil and oil-water capillary pressures, respectively.

Kinetic reactions are modeled based on the mineral dissolution/precipitation rate law given in Eq. (A.5). The equilibrium reaction rates, by contrast, are typically not defined explicitly. Because the reactants and products reach the state of chemical equilibrium quickly, a thermodynamic approach is normally taken to characterize these reactions. As explained in Section A.1.2, the general mass action law is written as:

$$Q - K^{eq} = 0. \tag{2.5}$$

In a system with two fluid phases, the phase-equilibrium and composition constraints for two-phase thermodynamic equilibrium are:

$$f_{ig} - f_{il} = 0, \tag{2.6}$$

$$\sum_{i=1}^{n_f} X_{ij} - 1 = 0, \tag{2.7}$$

where f_{ig} and f_{il} are the fugacities of fluid component i in the gas and liquid phases. These fugacities can be obtained from cubic equations of state (e.g., [89]) or from correlations (e.g., Henry's law in [78]).

2.1.2 Reduction of reaction rates

The set (vector) of reaction rates in a given chemical system, $\mathbf{r}_k$ and $\mathbf{r}_q$, can span a wide range of reaction time scales, which may cause Eqs. (2.1) and (2.2) to be quite stiff [30]. Moreover, due to the assumption of instantaneous equilibrium, reaction rates are generally not defined for equilibrium reactions. An effective strategy is to linearly transform the mass balance equations to eliminate equilibrium reaction rates [28, 65, 66]. In previous work in our group [26, 28], this transformation resulted in the element mass balance equations. The same linear transformation was then presented using an 'extended element stoichiometric matrix,' designated $\mathbf{E}$, which eliminates the equilibrium rates and also minimizes the number of times the kinetic rates appear in

the transformed mass balance equations [31].

For conciseness, we write the mass balance equations in a matrix-vector format. Assembling the stoichiometric coefficients in a stoichiometric matrix $\mathbf{S}$ leads to the following representation of Eqs. (2.1) and (2.2):

$$\frac{\partial \mathbf{N}}{\partial t} + \mathbf{L} = \mathbf{S}_{n_s \times n_r} \mathbf{r}_{n_r \times 1}, \tag{2.8}$$

where $\mathbf{N}$ is the vector of total component concentrations, $\mathbf{L}$ is the vector of flux terms, and $\mathbf{r}$ is the vector of all reaction rates; i.e., $\mathbf{r} = (\mathbf{r}_k, \mathbf{r}_q)^T$. The dimensions of $\mathbf{N}$ and $\mathbf{L}$ are $n_s = n_f + n_m$. Each column of $\mathbf{S}$ represents a reaction (the column entries provide the stoichiometric coefficients), with the first n_k columns corresponding to kinetic reactions and the remaining columns to equilibrium reactions. We will give the components of $\mathbf{S}$ for a simple example below.

Kinetic and equilibrium reactions can both be represented in a form where some species are expressed in terms of other species. A canonical form for the stoichiometric matrix, referred to as $\bar{\mathbf{S}}$, can then be defined [77]:

$$\bar{\mathbf{S}}_{n_s \times n_r} = \left[\begin{array}{c:c} \mathbf{S}_{1,(n_s - n_r) \times n_k} & \mathbf{S}_{2,(n_s - n_r) \times n_q} \\ \hdashline -\mathbf{I}_{2,n_k \times n_k} & \mathbf{S}_{3,n_k \times n_q} \\ \mathbf{0}_{n_q \times n_k} & -\mathbf{I}_{1,n_q \times n_q} \end{array}\right]. \tag{2.9}$$

Here $\mathbf{S}_1, \mathbf{S}_2$ and $\mathbf{S}_3$ are submatrices of the canonical stoichiometric matrix $\bar{\mathbf{S}}$, and $\mathbf{I}_1$ and $\mathbf{I}_2$ are identity matrices. The vertical dashed line separates kinetic reactions (on the left) and equilibrium reactions (on the right). The horizontal dashed line clarifies the various submatrices in the example below. The $\bar{\mathbf{S}}$ matrix is typically straightforward to derive once the chemical system is defined. Otherwise, the methodology proposed in Section A.2.3 may be used to yield $\bar{\mathbf{S}}$ for any set of chemical reactions.

As an example, consider the chemical system with eight species and four independent reactions shown in Table 2.1. Note that this reaction set is the canonical form of the one given in Table A.1; the two reaction systems are thus equivalent. The (canonical) stoichiometric matrix representing Table 2.1 is given as follows (the component

Table 2.1: Chemical system describing calcite dissolution.

Reaction #	Type	Reactions
1	Kinetic	$CaCO_3 \longrightarrow Ca^{2+} + {CO_3}^{2-}$
2	Equilibrium	${HCO_3}^- = H^+ + {CO_3}^{2-}$
3	Equilibrium	$H_2O = H^+ + OH^-$
4	Equilibrium	$CO_2 + OH^- = H^+ + {CO_3}^{2-}$

corresponding to each row is shown on the right):

$$\bar{\mathbf{S}} = \left[\begin{array}{c:ccc} 0 & 1 & 1 & 1 \\ 1 & 1 & 0 & 1 \\ 1 & 0 & 0 & 0 \\ 0 & 0 & 1 & -1 \\ \hdashline -1 & 0 & 0 & 0 \\ 0 & -1 & 0 & 0 \\ 0 & 0 & -1 & 0 \\ 0 & 0 & 0 & -1 \end{array}\right] \begin{array}{l} H^+ \\ {CO_3}^{2-} \\ Ca^{2+} \\ OH^- \\ \\ CaCO_3 \\ {HCO_3}^- \\ H_2O \\ CO_2 \end{array} . \tag{2.10}$$

In the following we assume that the stoichiometric matrix is in canonical form, so we use $\mathbf{S}$ in place of $\bar{\mathbf{S}}$.

To further simplify Eq. (2.8), we define a $(n_e + n_k) \times n_s$ matrix $\mathbf{E}$, where n_e is the number of elements (note that $n_e = n_s - n_r$), as:

$$\mathbf{E} = \left[\begin{array}{c} \mathbf{E}_1 \\ \mathbf{E}_2 \end{array}\right]. \tag{2.11}$$

Here, $\mathbf{E}_1$ is the $n_e \times n_s$ element stoichiometric matrix consisting of the stoichiometric values for each element in the formula of each species; i.e., $\mathbf{E}_1 = (E_{ei})$, where E_{ei} is the number of element e in species i. The matrix $\mathbf{E}_1$ for an example system is given in Eq. (A.10) (where it is referred to as $\mathbf{F}$). Note that the elements can be defined

as atoms or any compound that does not get decomposed under the reaction system. We further define $\mathbf{E}_2$ as:

$$\mathbf{E}_2 = [\mathbf{0}_{n_k \times (n_s - n_r)} \quad -\mathbf{I}_{2,n_k \times n_k} \quad -\mathbf{S}_{3,n_k \times n_q}], \tag{2.12}$$

where the subscripts denote the dimensions of the submatrix (note that $n_r = n_q + n_k$).

Element conservation in chemical systems can be expressed as follows [28]:

$$\mathbf{E}_{1,n_e \times n_s} \mathbf{S}_{n_s \times n_r} = \mathbf{0}_{n_e \times n_r}. \tag{2.13}$$

We can additionally write:

$$\mathbf{E}_2 \mathbf{S} \mathbf{r} = [\mathbf{0} \quad -\mathbf{I}_2 \quad -\mathbf{S}_3] \begin{bmatrix} \mathbf{S}_1 & \mathbf{S}_2 \\ -\mathbf{I}_2 & \mathbf{S}_3 \\ \mathbf{0} & -\mathbf{I}_1 \end{bmatrix} \begin{bmatrix} \mathbf{r}_k \\ \mathbf{r}_q \end{bmatrix} = [\mathbf{I}_2 \quad \mathbf{0}] \begin{bmatrix} \mathbf{r}_k \\ \mathbf{r}_q \end{bmatrix} = \mathbf{r}_k. \tag{2.14}$$

Therefore, premultiplying Eq. (2.8) by $\mathbf{E}$ eliminates all of the equilibrium rates:

$$\frac{\partial (\mathbf{EN})}{\partial t} + \mathbf{EL} = \mathbf{ESr} = \begin{bmatrix} \mathbf{E}_1 \mathbf{S} \mathbf{r} \\ \mathbf{E}_2 \mathbf{S} \mathbf{r} \end{bmatrix} = \begin{bmatrix} \mathbf{0} \\ \mathbf{r}_k \end{bmatrix}_{(n_e + n_k) \times 1}. \tag{2.15}$$

The first n_e equations in the transformed mass balances in Eq. (2.15) represent element balances. Our formulation is in fact based on these element balances. It should be noted that the 'elements' defined here are analogous to the 'components' used widely in hydrogeological formulations [65, 30, 79, 28]. The last n_k equations are linear combinations of the original species conservation equations. By combining the conservation equations in this way, each kinetic reaction rate only appears in one equation, as seen in Eq. (2.15).

In summary, the number of equations in the full set of transformed equations, which include Eqs. (2.5), (2.6), (2.7) and (2.15), is $n_e + n_k + n_q + n_f(n_p - 1) + n_p = n_p + n_m + n_f n_p$. The number of unknown variables, n_u, in this (isothermal) system is also $n_u = n_p + n_m + n_f n_p$. These consist of one pressure, $(n_p - 1)$ saturations, n_m solid

species concentrations, and $n_f n_p$ fluid phase molar fractions. The full set of governing equations can be algebraically reduced to a primary set, with only primary unknowns appearing. This system is then solved using Newton's method, as discussed below. We note finally that the number of primary equations (and unknowns) is equal to the number of equations in Eq. (2.15) that contain flux terms.

2.1.3 Jacobian-level transformation

Though it is possible to directly discretize the full set of governing equations [i.e., Eqs. (2.5), (2.6), (2.7) and (2.15)], this level of effort is not required. If the chemical reaction treatment is being implemented into an existing compositional simulator, the chemical reaction module can be incorporated into the Jacobian matrix constructed without reaction terms, as described below. Other features of the compositional simulator, such as the discretization techniques, phase behavior models, linear solver, etc., can thus be used for the chemical-compositional model with no modifications.

Before explaining the required manipulations, we emphasize that, at each iteration, the full component-based Jacobian matrix is constructed. We will apply Newton's method; i.e., we solve $\mathbf{J}(\delta\mathbf{x}) = -\mathbf{R}$, where $\mathbf{J}$ and $\mathbf{R}$ are the Jacobian matrix and residual vector and $\delta\mathbf{x}$ is the solution update. We now present the steps required for integration of chemical reactions into the compositional formulation. Additional details are provided after the description of the overall procedure.

1. Construct the compositional Jacobian matrix (without reaction terms). This matrix will contain the derivatives of n_s (discretized) species mass balance equations, $n_f(n_p - 1)$ phase equilibrium constraints, and n_p phase composition constraints, with respect to $n_u = n_p + n_m + n_f n_p$ unknowns. Build the corresponding residual vector.

2. Premultiply the first n_s rows (species mass balances) in each nonzero Jacobian block by matrix $\mathbf{E}$ defined in Eq. (2.11). Apply the same multiplication to the residual vector. The result is $n_e + n_k$ equations, corresponding to Eq. (2.15). This gives matrix blocks of dimension $(n_e + n_k) \times n_u$.

3. To the above $n_e + n_k$ equations, add derivatives of n_q mass actions laws (one

for each equilibrium reaction). This gives a total of n_s equations (recall that $n_s = n_e + n_k + n_q$), constituting a matrix block of dimension $n_s \times n_u$.

4. Replace the first n_s rows in each Jacobian block by the n_s equations obtained in step 3. Note that the last $n_f(n_p - 1) + n_p$ equations corresponding to the phase equilibrium and phase composition constraints remain unchanged from step 1.

5. Perform Schur-complement reductions (as is usual in compositional simulation) to reduce the $n_u \times n_u$ Jacobian blocks to $n_s \times n_s$ blocks [15].

6. Perform the chemical reaction Schur-complement reduction to further reduce the $n_s \times n_s$ blocks to $n_{pr,f} \times n_{pr,f}$ blocks, where $n_{pr,f}$ is the final number of primary variables in the chemical-compositional system. This reaction reduction procedure is explained in detail in the next section.

7. Proceed with linear solution, with Jacobian blocks of size $n_{pr,f} \times n_{pr,f}$, to provide $\delta\mathbf{x}$.

8. Update the primary unknowns ($\mathbf{x}^{\nu+1} = \mathbf{x}^{\nu} + \delta\mathbf{x}$, where ν is the iteration index). Update the secondary variables based on primary variables, as usual in compositional simulation ([18, 15]). Proceed to the next Newton iteration or time step after proper convergence check.

Steps 2, 3, 4 and 6 describe the additional calculations required for the chemical reaction module. Eq. (2.16) illustrates the transformation of the Jacobian matrix

from step 1 to 4:

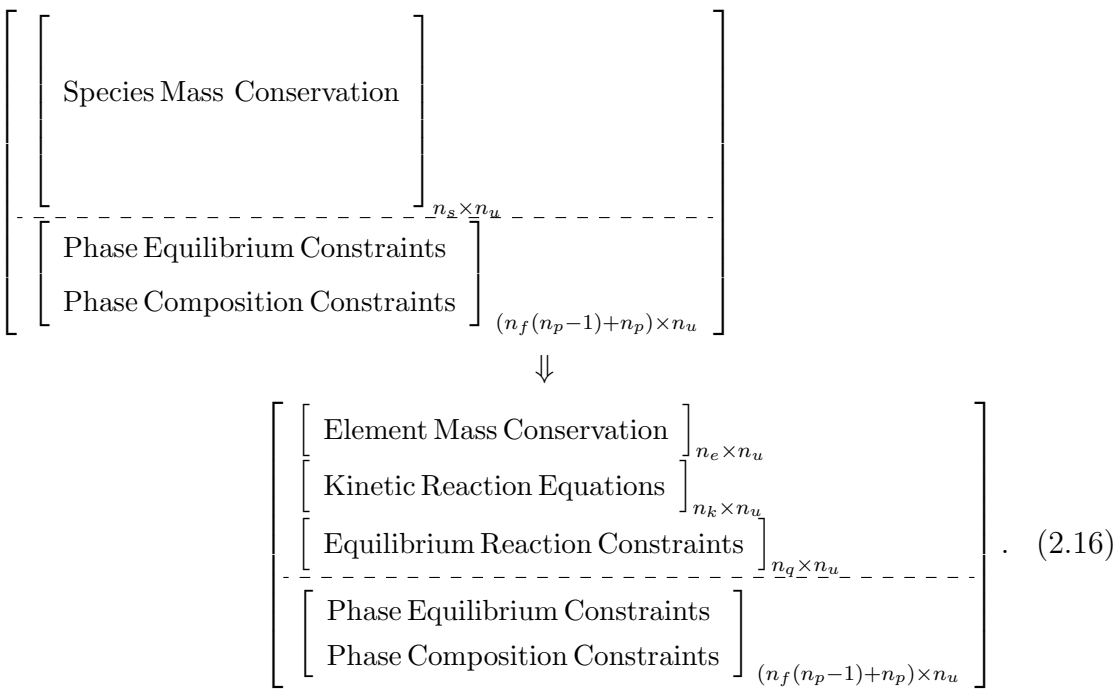

$$\Downarrow$$

. (2.16)

Here, we see that the component mass balances are transformed to element balances along with reaction equations. It is evident that the portions of the Jacobian matrix corresponding to phase equilibrium and phase-composition constraints are unchanged. We note finally that steps 5 and 6 can be integrated into a one-step Schur-complement reduction. The Schur complement procedure is described in the next section.

2.1.4 Treatment of primary and secondary equations

It is standard practice in compositional reservoir simulation to divide the governing equations into primary and secondary equations [19, 133]. This reduces the total number of variables in the linear solver stage and improves the computational efficiency significantly. In this section we briefly describe this decoupling procedure. The treatment presented here is strictly applicable to two-point flux approximations. The extension of this procedure to our reactive-transport formulation is then discussed.

The full set of residual equations can be split into primary equations, $\mathbf{R}_p = \mathbf{0}$, and secondary equations, $\mathbf{R}_s = \mathbf{0}$. We thus write $\mathbf{R}(\mathbf{x}) = [\mathbf{R}_p(\mathbf{x}),\ \mathbf{R}_s(\mathbf{x})]^T = \mathbf{0}$. Similarly,

the set of unknown variables is split into primary and secondary sets: $\mathbf{x} = (\mathbf{x}_p,\ \mathbf{x}_s)^T$. In general, equations that depend only on variables local to the control volume (i.e., equations without flux terms) are considered to be secondary equations.

Consider a pair of adjacent control volumes, which we designate as cells 1 and 2. The portion of the Jacobian matrix $\mathbf{J}$ corresponding to these two cells can be written as follows:

$$\begin{bmatrix} \mathbf{A}_{11} & \mathbf{B}_{11} & \mathbf{A}_{12} & \mathbf{B}_{12} \\ \mathbf{C}_{11} & \mathbf{D}_{11} & \mathbf{0} & \mathbf{0} \\ \mathbf{A}_{21} & \mathbf{B}_{21} & \mathbf{A}_{22} & \mathbf{B}_{22} \\ \mathbf{0} & \mathbf{0} & \mathbf{C}_{22} & \mathbf{D}_{22} \end{bmatrix} \begin{bmatrix} \delta\mathbf{x}_p^1 \\ \delta\mathbf{x}_s^1 \\ \delta\mathbf{x}_p^2 \\ \delta\mathbf{x}_s^2 \end{bmatrix} = - \begin{bmatrix} \mathbf{R}_p^1 \\ \mathbf{R}_s^1 \\ \mathbf{R}_p^2 \\ \mathbf{R}_s^2 \end{bmatrix}, \tag{2.17}$$

where $\mathbf{R}_p^1$ and $\mathbf{R}_s^1$ are the primary and secondary residual vectors for cell 1, $\mathbf{x}_p^1$ and $\mathbf{x}_s^1$ are the primary and secondary variables for cell 1, etc. The rows containing the $\mathbf{A}$ and $\mathbf{B}$ matrices correspond to primary equations, and those with the $\mathbf{C}$ and $\mathbf{D}$ matrices correspond to secondary equations. We designate n_{pr} to be the number of primary variables ($n_{pr} = n_s$ in isothermal compositional simulation) and n_{sec} as the number of secondary variables. It follows that the $\mathbf{A}$ matrices are of dimensions $n_{pr} \times n_{pr}$, the $\mathbf{B}$ matrices are $n_{pr} \times n_{sec}$, the $\mathbf{C}$ matrices are $n_{sec} \times n_{pr}$, and the $\mathbf{D}$ matrices are $n_{sec} \times n_{sec}$. The zero submatrices appear because the secondary equations for each cell are only functions of the variables in that block. Note that the Jacobian block discussed in the preceding section corresponds to the entries for a single cell; i.e., the submatrices $\mathbf{A}_{11}$, $\mathbf{B}_{11}$, $\mathbf{C}_{11}$ and $\mathbf{D}_{11}$.

The Schur reduction entails the application of Gaussian elimination to Eq. (2.17) to eliminate the $\mathbf{B}$ matrices. This step is a local operation that can be applied cell by cell. To accomplish this, $\mathbf{D}_{11}$ and $\mathbf{D}_{22}$ are inverted, and a linear transformation is applied on the first and third rows, resulting in the following system:

$$\begin{bmatrix} \bar{\mathbf{A}}_{11} & \mathbf{0} & \bar{\mathbf{A}}_{12} & \mathbf{0} \\ \mathbf{C}_{11} & \mathbf{D}_{11} & \mathbf{0} & \mathbf{0} \\ \bar{\mathbf{A}}_{21} & \mathbf{0} & \bar{\mathbf{A}}_{22} & \mathbf{0} \\ \mathbf{0} & \mathbf{0} & \mathbf{C}_{22} & \mathbf{D}_{22} \end{bmatrix} \begin{bmatrix} \delta\mathbf{x}_p^1 \\ \delta\mathbf{x}_s^1 \\ \delta\mathbf{x}_p^2 \\ \delta\mathbf{x}_s^2 \end{bmatrix} = - \begin{bmatrix} \bar{\mathbf{R}}_p^1 \\ \mathbf{R}_s^1 \\ \bar{\mathbf{R}}_p^2 \\ \mathbf{R}_s^2 \end{bmatrix}, \tag{2.18}$$

where $\bar{\mathbf{A}}_{11} = \mathbf{A}_{11} - \mathbf{B}_{11}\mathbf{D}_{11}^{-1}\mathbf{C}_{11}$ (similar transformations provide submatrices $\bar{\mathbf{A}}_{12}$, $\bar{\mathbf{A}}_{21}$ and $\bar{\mathbf{A}}_{22}$). It is evident from Eq. (2.18) that the primary equations are now decoupled from the secondary unknowns at the level of the Jacobian matrix. Thus, the system can be solved for primary variables. Once these values are computed, the secondary variables can be calculated efficiently.

As described by Fan et al. [28], there are two types of reduction that can be performed with our chemical reaction treatment, and we refer to these as the 'reactions-coupled' and 'local-reactions-decoupled' approaches. In the 'reactions-coupled' method, we apply the Schur complement procedure described above, treating element-conservation and reaction equations as primary equations, and phase equilibrium and phase constraints as secondary equations. We refer to this approach as 'reactions-coupled,' since the reaction equations are coupled with the conservation equations at the linear solution stage. The implementation of this treatment is quite straightforward in an existing compositional simulator.

In the second approach, we classify each of the last n_k equations in Eq. (2.15) based on the presence or absence of flux terms. Of relevance is the fact that both the equilibrium and kinetic mineral reaction equations treated are local (no flux terms). Thus, the equations corresponding to these reactions (see Eq. (2.16)) can be treated as secondary equations. We refer to this approach as the 'local-reactions-decoupled' method because these reaction equations are eliminated (using Gaussian elimination) prior to solving the linear system. This method thus entails a two-step reduction. The Jacobian matrix after the first reduction step is exactly the same as the reduced Jacobian in the reaction-coupled method.

We reiterate that both approaches are fully coupled and fully implicit; the use of the terms 'coupled' and 'decoupled' here just refers to the treatment at the Jacobian (i.e., linear solution) level. The number of (final) primary equations/variables, $n_{pr,f}$, in the reactions-coupled method is $n_{pr,f} = n_s = n_e + n_k + n_q$, and in the local-reactions-decoupled method it is $n_{pr,f} = n_e + n_{kf}$, where n_{kf} is the number of kinetic reaction equations (out of the last n_k equations in Eq. (2.15)) that include flow terms. In many cases, n_{kf} is significantly less than $n_k + n_q$, which renders the decoupled approach much less expensive in the linear solution stage than the reaction-coupled treatment.

See [28] for further discussion and for performance results using the two approaches.

2.1.5 Generalized reaction modeling

The chemical reaction treatments described above are applicable to general reactive-transport modeling. Reactions can, however, be classified in different ways. More specifically, the reactions encountered in groundwater applications are generally characterized in terms of activities [59], while the reactions in oil and gas applications are usually expressed in terms of concentrations [33, 27]. It is desirable to treat all of these reactions in the same framework. In our formulation, we treat the reaction-related terms, r_k and Q_q, in a generalized form:

$$r_k = f(p_j, S_j, C_s, X_{ij}, f_{ij}, a_{ij}, C_{ij}), \tag{2.19}$$

$$Q_q = f(p_j, S_j, C_s, X_{ij}, f_{ij}, a_{ij}, C_{ij}), \tag{2.20}$$

where f is fugacity, a is activity, and C is concentration. Note that not all of these parameters are required to characterize a reaction. For example, the equilibrium constraint for $HCO_3{}^- = H^+ + CO_3{}^{2-}$ is given based on aqueous activities as $(a_{H^+})(a_{CO_3{}^{2-}})(a_{HCO_3{}^-})^{-1} = K^{eq}$, while for $2\,NO = N_2O_2$ it is expressed in terms of fugacities as $(f_{N_2O_2})(f_{NO})^{-2} = K^{eq}$.

2.1.6 Treatment of phase disappearance and reappearance

In some simulations of CO_2 storage, we observe the disappearance of the brine phase, typically at or near the injection well, which is due to the evaporation of all the residual water into the injected gas stream. This aqueous phase disappearance can cause significant computational problems, such as time step cuts and lack of convergence. This occurs because certain components (so-called aqueous species, such as ions) are linked to the aqueous phase, and the implementation in [28] was based on the assumption that some amount of brine was always present. Here, we describe a general approach for handling the aqueous phase and aqueous species that is applicable when the aqueous phase disappears and/or reappears.

In Fan et al. [28], when the water saturation reaches zero, the entries in the columns

of the Jacobian matrix corresponding to the aqueous species (other than water and CO_2) also become zero. This results in singular Jacobian matrices, and that leads to time step cuts, or convergence challenges for the nonlinear (Newton) solver. It might be expected that the supersaturation that results when water saturation becomes very small would drive precipitation reactions, and thus consume the dissolved aqueous species. If this were indeed the case, the mass conservation problems could be resolved, in theory, by taking very small time steps. Mineral dissolution and precipitation reaction rates can, however, be such that some of the so-called aqueous species will be deposited through mechanisms not represented by these rates; i.e., the reaction kinetics are not sufficiently fast to ensure that all of the mass has reacted to form minerals before water disappears [71]. A simple physical analogy is the evaporation of sea water in contact with a surface that can react with the dissolved salt. If the sea water evaporates fast enough, the salt will not have time to react with the surface, and we will be left with a pile of salt. This is the 'deposited phase' to which we refer below. The 'precipitant' is generated by the reactions accounted for in the formulation.

The detailed chemistry of this deposited phase, which could itself then react with the rock, can be very complicated [101] and may not be fully characterized. Even if a reaction model for the deposited species is available, the large number of species involved may render the model overly complex and time consuming to evaluate. This, combined with the fact that the deposited phase typically involves only a very small amount of mass, motivates us to pursue a simpler treatment.

Our approach for handling the aqueous species (other than CO_2 and H_2O) entails the addition of a new stationary solid phase – which we call the deposited phase – to account for these components when the aqueous phase disappears. We consider this deposited material to be readily soluble in the presence of water, which means the aqueous species will redissolve to the extent possible when the water phase reappears. We model this deposition and dissolution by introducing a new source term in the mass conservation law for aqueous species.

Specifically, the source term ($-q_i^D$) is added to the right hand side of Eq. (2.1) for fluid species other than CO_2 and H_2O. This term is related to the mass of fluid

species i in the deposited phase (designated M_i^D) via:

$$\frac{\partial M_i^D}{\partial t} = q_i^D. \tag{2.21}$$

Thus, the aqueous species can exist in the brine phase as well as in the deposited phase within the block. The source term q_i^D represents the transfer of mass between these two phases. This transfer can be modeled as an instantaneous phenomenon, with deposition occurring at the point of water disappearance. Upon water reappearance, instantaneous dissolution of the deposited phase into a small water volume can, however, change the water composition significantly. Because this can cause problems for our phase behavior computations, we choose to relate q_i^D to system variables, as described below.

The quantity that characterizes the ability of the aqueous phase to maintain charged species (ions) in solution is the ionic strength, introduced in Section A.1.1:

$$I = \frac{1}{2}\sum_{i=1}^{n_c} m_{i,w} Z_i^2, \tag{2.22}$$

where $m_{i,w}$ and Z_i are, respectively, the molality and charge of the aqueous species i. In this work, a maximum attainable ionic strength I_{max} for the aqueous phase is prescribed, and if this is reached, ions are transferred to the deposited phase. The mass transfer between the aqueous phase and the deposited phase can be represented in our formulation as either an equilibrium (instantaneous) reaction, or as a kinetic reaction, though the equilibrium treatment may result in the phase behavior issues noted above. For this reason we apply a kinetic approach. We will demonstrate later that our large-scale results appear to be insensitive to the details of this kinetic treatment.

For our kinetic treatment of dissolution, we first define a general dissolution rate r^D:

$$r^D = k^D \phi S_w (I_{max} - I), \tag{2.23}$$

where k^D (moles/volume/time) is the dissolution rate constant. Although it may be

possible to obtain k^D experimentally, this should not be necessary in general. The above expression results in dissolution only if $I < I_{max}$, consistent with our discussion of ionic strength above. The dissolution rate for aqueous species i (q_i^D) is now given by:

$$q_i^D = -\alpha_i r^D, \tag{2.24}$$

where α_i is simply the molar fraction of species i in the deposition phase:

$$\alpha_i = \frac{M_i^D}{\sum_{k=1}^{n_{aq}} M_k^D}, \tag{2.25}$$

where n_{aq} is the number of aqueous species other than CO_2 and H_2O. Note that this treatment for α_i keeps constant the relative fractions of the various ions in the deposited phase throughout dissolution. If experimental evidence indicates otherwise, α_i can be modified accordingly.

This treatment for the deposited phase has been implemented into our chemical-compositional simulator, AD-GPRS. Although the amount of deposited mass is generally small, by tracking this phase, and by applying other variable switching as necessary, we are able to maintain mass conservation and simulator robustness even in cases where the aqueous phase completely disappears in multiple grid blocks. With the implementation in [28], which lacked a treatment for this phenomenon, we observed convergence problems as the grid was refined. This limited the size of the models that could be simulated. The problems with more refined models appear to be due to the fact that water disappearance tends to occur in more cells as the grid is refined.

2.2 Results for CO_2 storage simulations

We now present a series of results that demonstrate the capabilities of our chemical reaction treatment in CO_2 storage problems, including cases with aqueous phase disappearance. All cases are run using the chemical-compositional module described above, which has been implemented into Stanford's Automatic Differentiation-based

General Purpose Research Simulator (AD-GPRS), except for the first example involving a single-block model.

2.2.1 Phase disappearance and reappearance in a single block

We first apply a single-block model to study the deposition and dissolution of aqueous species. The purpose of this is to (1) demonstrate and quantify deposition and dissolution in a simple set up, and (2) assess the performance of a kinetic model for treating these effects. The kinetic model is useful because it leads to improved numerical performance in AD-GPRS, and in the results here we demonstrate that quantities of interest are only minimally impacted by this treatment.

The problem set up is displayed in Fig. 2.1. The block is initially filled with the brine (aqueous) phase, which contains three components: H_2O, CO_2, and an aqueous component, c_3. The latter converts into a solid mineral phase through an irreversible first-order kinetic reaction:

$$c_3 \xrightarrow{r_M} c_{3,mineral}. \tag{2.26}$$

This precipitation reaction is governed by the following reaction rate:

$$r_M = k_M \phi S_w \rho_w x_{c_3}, \tag{2.27}$$

where r_M is in moles/volume/time, and k_M is the reaction rate constant, with units of time^{-1}.

Pure CO_2 is injected into the block for a long period of time. This causes water to vaporize (phase equilibrium is modeled using K-values [12], as described below) and eventually the water phase disappears. This in turn causes c_3 to deposit (in a 'deposited phase,' as explained earlier) in the block. After all of the c_3 has been deposited, pure H_2O is injected, which leads to the dissolution of the deposited material. The quantity of interest in this problem is the distribution of c_3, over the various phases, as a function of time. We define the dimensionless Damköhler number to

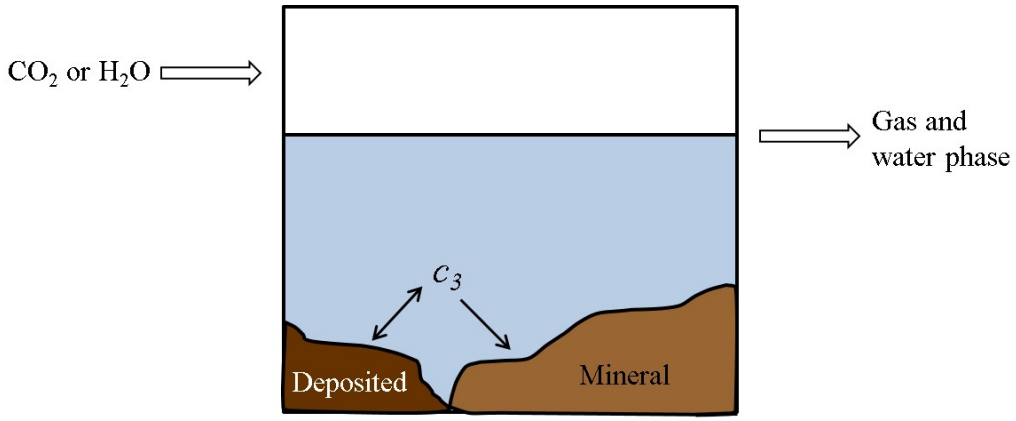

Figure 2.1: Schematic of the single-block model.

quantify the ratio of the characteristic times of transport and reaction as follows:

$$Da = \frac{V_b \rho k_M}{q}, \tag{2.28}$$

where V_b is the volume of the block, ρ is the density of the phase at the inlet in moles/volume (we assume single-phase inlet flow), and q is the molar flow rate at the inlet in moles/time.

The equilibrium between fluid phases is modeled using K-values. The pressure and temperature are kept constant in time, so fluid must be removed from the block to balance the injection. The solid phases are assumed to have negligible volumes. The brine and gas phase flow rates are taken to be directly proportional to their saturations, which can be interpreted as using linear relative permeability functions. We further assume that there is a limit on the amount of c_3 that can exist in the brine phase (consistent with I_{max}), and any c_3 beyond this limit will be deposited instantaneously. Here we specify the maximum molar fraction of c_3 in water to be 0.3.

The following equations describe the mass distribution at any time:

$$M_i = \phi V_b (S_w \rho_w x_i + S_g \rho_g y_i), \tag{2.29}$$

$$y_i = k_i x_i, \tag{2.30}$$

where i indicates one of the three components, M_i is the number of moles of component i in the block, ρ_w and ρ_g are phase densities in moles/volume, and x_i and y_i are water and vapor phase molar compositions respectively. This single-block model is simulated using two different approaches. In the first approach, which is 'exact' (given the assumptions above), c_3 is instantaneously deposited when it reaches its maximum molar fraction in the aqueous phase. Upon water reappearance, it will be instantaneously dissolved into water until I_{max} is reached.

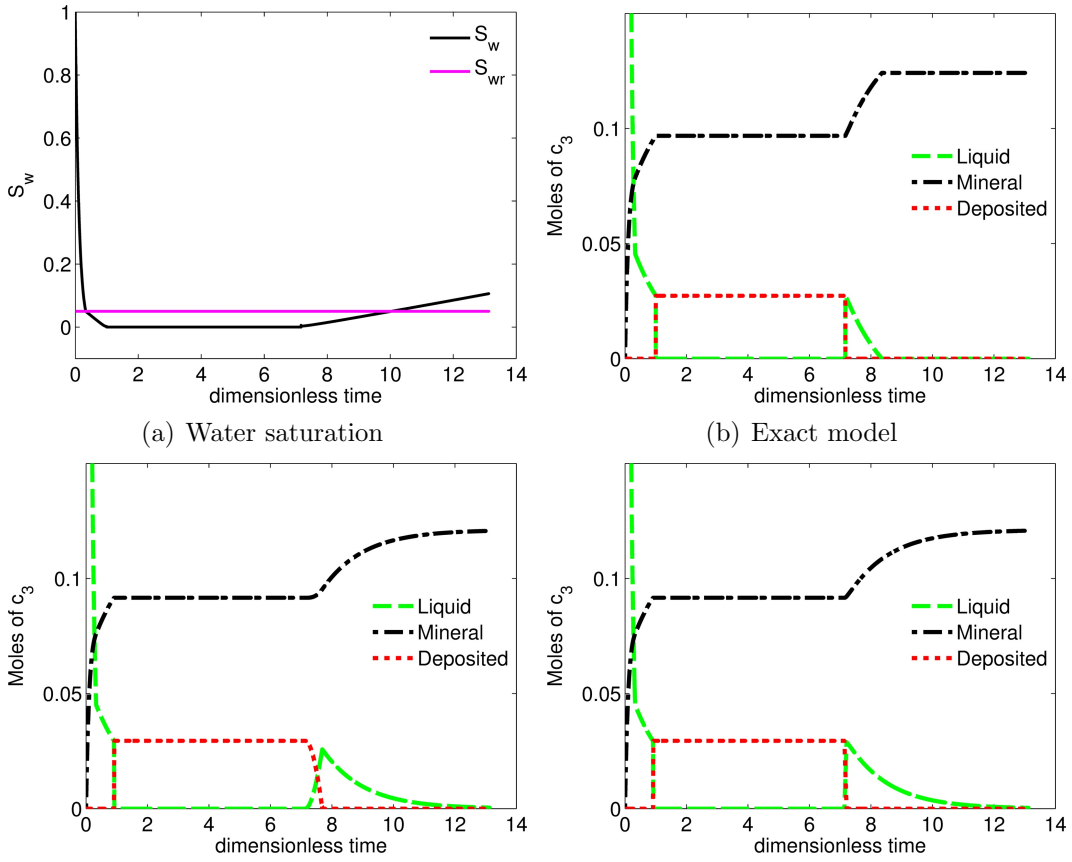

(a) Water saturation (b) Exact model

(c) Approximate model, k_D/k_M=1 (d) Approximate model, k_D/k_M=1000

Figure 2.2: Water saturation and distribution of component c_3 as a function of time.

In the second, 'approximate,' approach, deposition and dissolution do not occur instantaneously, but instead are treated as a kinetic reaction. This model also does not treat the thermodynamics as rigorously as the exact model, i.e., the flash is performed by ignoring the c_3 component, and the aqueous phase compositions are subsequently

scaled to account for the mass of dissolved c_3. The following reaction rate governs the mass transfer between the brine and the deposited phase:

$$r_D = k_D \phi S_w \rho_w (x_{c_3} - x_{c_3,max}), \tag{2.31}$$

where r_D, with units of moles/volume/time, is analogous to the rate defined in Eq. (2.23), and k_D is the reaction rate constant with units of time^{-1}. A positive reaction rate applies for deposition and a negative value for dissolution. Note that we use r_D and k_D here, instead of r^D and k^D as used in Eq. (2.23), since the model is now simpler and the terms are not exactly the same.

The block initially contains 49 moles of H_2O, 5.5 moles of CO_2 and 1 mole of c_3, which gives an initial molar fraction of 0.018 for c_3 (recall that $x_{c3,max} = 0.3$) . The K-values for CO_2, H_2O and c_3 are 9, 0.12 and 0, respectively. The block is initially at 100% brine saturation. Pure CO_2 is injected at a fixed Damköhler number of 0.1. Water then flows out of the system until the residual water saturation (S_{wr}) of 0.05 is reached. Although the brine phase no longer flows, as CO_2 is injected water continues to vaporize into the gas phase, which in turn increases the molar fraction of c_3 in water, causing c_3 deposition. The water phase eventually disappears, and time is nondimensionalized such that water disappearance corresponds to a dimensionless time of 1. At a dimensionless time of about 7, water is injected (at very low rate) into the system.

Results for water saturation and the mass distribution for c_3 are shown in Fig. 2.2(a). Water saturation reaches zero at a time of 1, and then increases when water injection starts (at a time of about 7). Mineralization (precipitation) is seen to occur as long as c_3 is in the water phase, but once the water phase disappears, the c_3 is immediately deposited. When the water phase reappears, the deposited c_3 redissolves, and the c_3 can then either mineralize, or reside in the water phase.

We next simulate this system using the approximate model, with the kinetic treatment of c_3 deposition and dissolution. Two different values of the rate constant k_D are considered: $k_D = k_M$ and $k_D = 1000 k_M$ (recall that k_M is the rate constant for the mineralization/precipitation reaction). Results for the mass distribution of c_3 as a

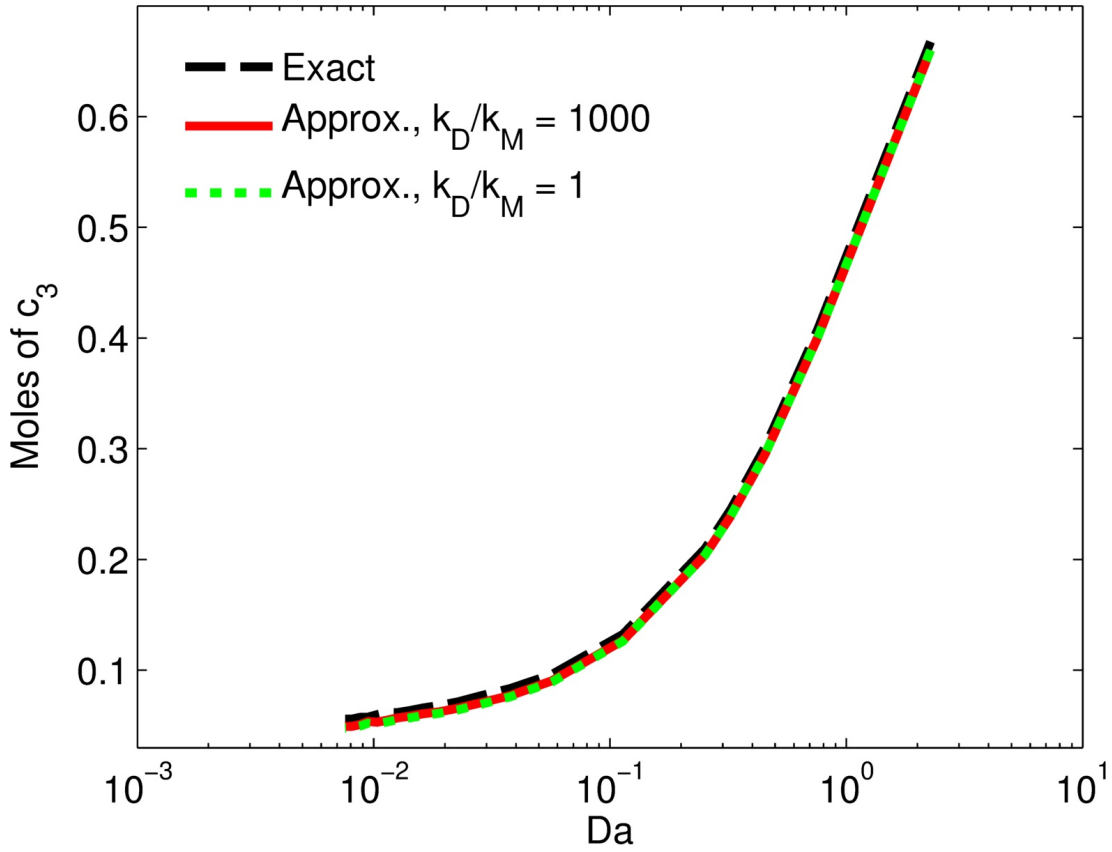

Figure 2.3: Amount of component c_3 that is mineralized after water disappearance and reappearance as a function of Damköhler number.

function of time are presented in Figs. 2.2(b) and (c). There are differences between these models and the exact solution when water injection occurs, starting at around a time of 7, but the long-time results for mineralized c_3 are very similar for all three cases. As expected, the results for the approximate model with $k_D = 1000k_M$ are closer to those of the exact model. Note that the models perform very similarly around the time of water disappearance, indicating that the kinetic treatment accurately captures this effect.

The results above were all for CO_2 injection rates corresponding to $Da = 0.1$. We repeat these simulations for Da ranging from 0.008 to 2.27. Results for the amount (moles) of component c_3 that is mineralized at the end of the run (after water disappearance and reappearance), as a function of Da, are shown in Fig. 2.3. The plot

displays results for the exact solution and for the different values of k_D considered above. It is evident that the results for the three cases are in close agreement.

The results in this section are encouraging as they demonstrate that the approximate kinetic treatment for modeling deposition and dissolution does not lead to significant errors in the key quantities of interest, such as the amount of c_3 that is mineralized after long times. We next assess the performance of this approach in AD-GPRS models.

2.2.2 One-dimensional AD-GPRS simulations

We now consider a one-dimensional AD-GPRS model that displays phase disappearance and reappearance. The model represents an aquifer that is $10,000$ ft $\times$ 1000 ft $\times$ 20 ft. Flow is in the x-direction and a total of 1000 grid blocks are used. The injector and producer are located in blocks 1 and 11 respectively. The wells are spaced closely in this case to allow reappearance of the water phase in the grid blocks experiencing water disappearance. The permeability is 100 md, porosity is 18%, and the initial reservoir pressure is 1711 psi. The reactions, shown in Table 4.6, and the rock and aquifer compositions and other system properties, are taken from [26]. This case involves a total of 12 components, six elements, and six reactions.

Table 2.2: Chemical reaction system used in mineralization examples

Reaction #	Type	Reactions
1	Equilibrium	$CO_2(aq) + H_2O = H^+ + HCO_3^-$
2	Equilibrium	$CO_3^{2-} + H^+ = HCO_3^-$
3	Equilibrium	$H_2O = H^+ + OH^-$
4	Kinetic	$\text{Anorthite} + 8\,H^+ = 4\,H_2O + Ca^{2+} + 2\,Al^{3+} + 2\,SiO_2(aq)$
5	Kinetic	$\text{Calcite} + H^+ = Ca^{2+} + HCO_3^-$
6	Kinetic	$\text{Kaolinite} + 6\,H^+ = 5\,H_2O + 2\,Al^{3+} + 2\,SiO_2(aq)$

CO_2 is injected at a constant rate of 5000 Mscf/d for 200 days. Over this time the producer is open, with a bottomhole pressure of 1000 psi. During the injection period the water phase disappears in the injection (and neighboring) blocks. After 200 days

both wells are shut in. At a later time, as a result of capillary pressure effects, water reappears.

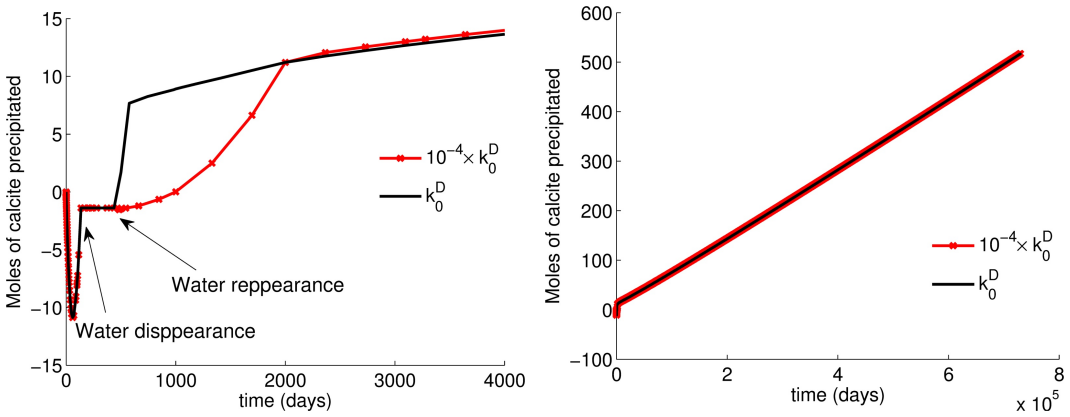

(a) Calcite profile over 4000 days (b) Calcite profile over 2000 years

Figure 2.4: Moles of calcite precipitated in the injection block over time. Results are shown for two k^D values of different orders of magnitude.

The deposition and dissolution are modeled using our approximate kinetic treatment. This case is more complicated than the single-block model because here we have a set of reactions (which are impacted by the choice of k^D) and flow from block to block. Results for the amount of precipitated calcite in the entire aquifer after 2000 years, for various k^D values, are shown in Table 2.3. In the table, $k_0^D = 10^{-10}$ moles/ft^3/day. Note that calcite is the only carbonate mineral in the system, and its precipitation is the sole means for mineral trapping of CO_2 in this problem. It is evident from the table that the choice of k^D has essentially no impact on the mineralization results. This is encouraging and suggests that k^D can be chosen based on numerical performance considerations.

Table 2.3: Mass of precipitated calcite (lb-moles at 2000 years) for different values of the deposition rate constant

k^D value (moles/ft^3/day)	$10^{-7}k_0^D$	$10^{-4}k_0^D$	$10^{-2}k_0^D$	k_0^D
Calcite (lb-moles), all reservoir	29075	29078	29081	29078

In Fig. 2.4 we show the progression in time of calcite precipitation, in the injection

block, for $k^D = k_0^D$ and $k^D = 10^{-4}k_0^D$. The right plot displays the full time period (730,000 days) and the left plot zooms in to the first 4000 days. On the scale of the right plot, we do not see any difference between the two cases, though differences are evident in the left plot during the first 2000 days. Specifically, in the case of $k^D = k_0^D$, material dissolves more rapidly in water (once water reappears, at around 500 days), which promotes earlier calcite precipitation. By 2000 days, however, the two solutions track closely. We note finally that the decrease in calcite at very early time results from a decrease in the pH due to the dissolution of carbon dioxide in water. However, the dissolution of anorthite ($CaAl_2Si_2O_8$) regulates the pH while providing Ca^{2+} cations in the brine phase, which leads to calcite precipitation.

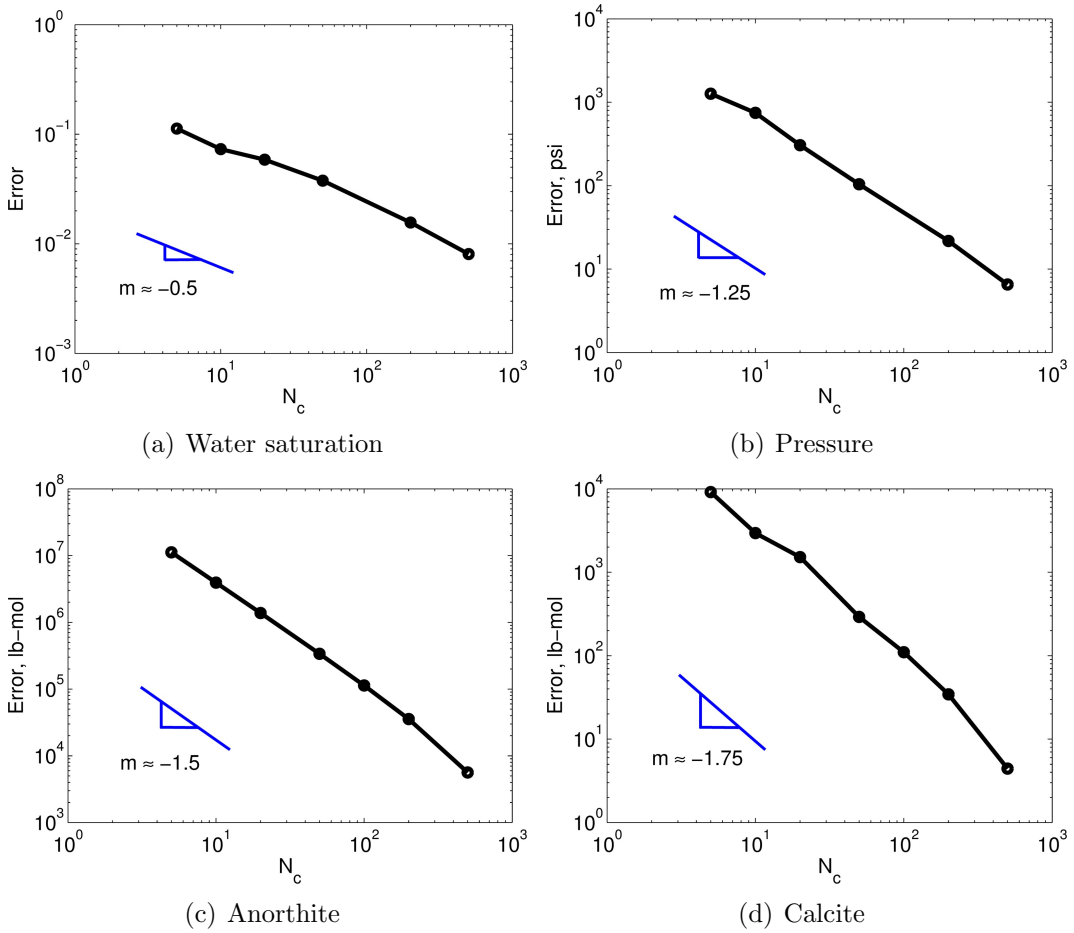

(a) Water saturation

(b) Pressure

(c) Anorthite

(d) Calcite

Figure 2.5: Convergence behavior at 2000 days for various quantities in one-dimensional model.

Because we are dealing with a complicated system that involves many interacting effects, it is of interest to assess the numerical convergence behavior of our GPRS implementation. This is most easily accomplished with a one-dimensional model. We thus consider the same system modeled above, except now we move the production well to the last grid block (far right of the model). The injection well remains at the far left (block 1). CO_2 is injected at the rate of 5000 Mscf/d for 6000 days. The wells are then shut in, and the simulation is run for 2000 years. In all but the most coarse model, water disappearance and reappearance occur in at least one grid block. Here, we specify $k^D = 10^{-20}$ moles/ft^3/day.

We consider models ranging from 5 blocks to 1000 blocks. Error is computed with respect to the 1000-grid-block model; i.e., we assume that the fine model represents the exact solution. Results for each coarse model are projected onto a 1000-block model to enable straightforward calculation of error (other approaches are also possible). This means that in the case of the 10-block model, the simulated quantities do not vary over each group of 100 blocks in the error calculation. Error (in the Euclidean norm) is computed as follows:

$$E_{2,z} = \left[\frac{1}{1000} \sum_{i=1}^{1000} (z_i^f - \bar{z}_i^c)^2 \right]^{\frac{1}{2}}, \tag{2.32}$$

where z is any variable, e.g., pressure, saturation or composition, z_i^f is the result in the 1000-block model, and $\bar{z}_i^c$ is the coarse-grid result projected onto a 1000-block model.

Convergence results, for quantities evaluated at 2000 years, are shown in Fig. 2.5. These (log-log) plots display the error, computed using Eq. (2.32), versus the number of blocks in the coarse model (N_c). Lines of slope that approximately match the error behavior (convergence rate) are shown in each plot. Although the convergence rate for saturation is relatively low, the convergence rates for anorthite and calcite are well above unity. This is satisfactory and demonstrates that our procedure is indeed convergent.

2.2.3 Simulation of a heterogeneous three-dimensional aquifer

Having illustrated our general modeling capability on simple models, we now consider a more realistic case. In this example, CO_2 is injected into the center of a three-dimensional aquifer for 40 years, and the system is simulated for another 1960 years. The 10.9 km $\times$ 10.9 km $\times$ 97.5 m system is the central part of the aquifer model used by [14] in an optimization study. To enhance resolution, we introduce $2 \times 2 \times 2$ refinement of each grid block of their model (keeping porosity and permeability constant over the eight cells). This results in a model of dimensions $50 \times 50 \times 16$ (total of 40,000 blocks). The permeability field is shown in Fig. 2.6.

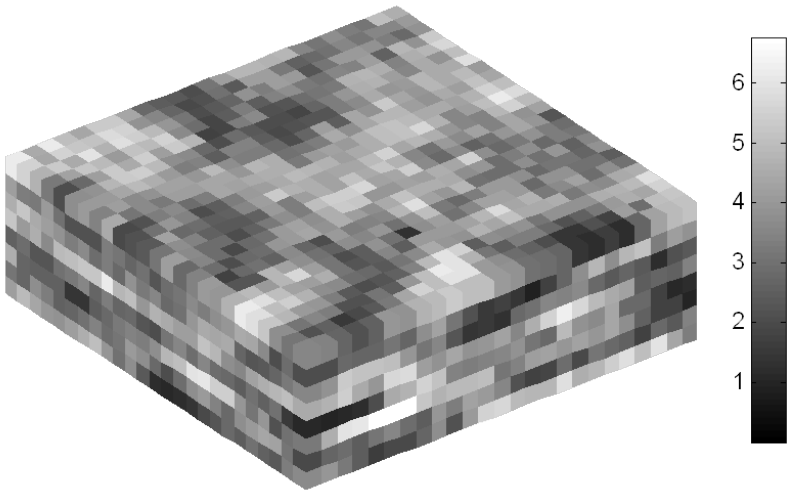

Figure 2.6: Permeability field (in md, log scale) for three-dimensional model.

The reaction set (Table 4.6), as well as the rock and aquifer compositions and other model properties, are the same as in the previous (one-dimensional) example. In this case we set $k^D = 10^{-20}$ moles/ft^3/day (this value was determined through numerical experimentation). The total injected CO_2 corresponds to about 1% of the aquifer pore volume, which is in the 1-4% range specified by the Intergovernmental Panel on Climate Change [105].

Fig. 2.7 displays the CO_2 in the supercritical 'gas' phase at the end of the injection period (for clarity, the model is sliced at the well block, and only the central portion is

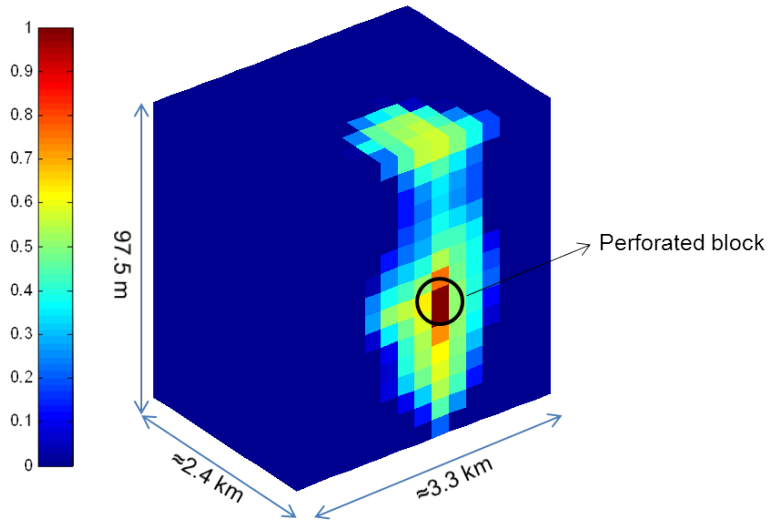

Figure 2.7: CO_2 phase saturation after 40 years of injection (central portion of the model shown).

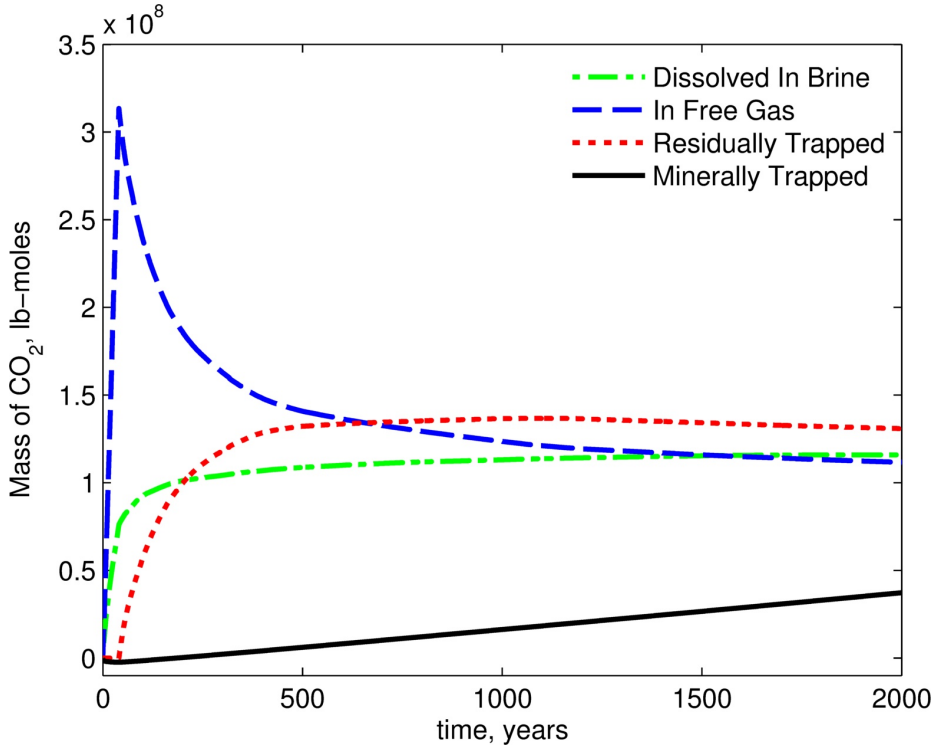

Figure 2.8: Distribution of the injected CO_2 over time.

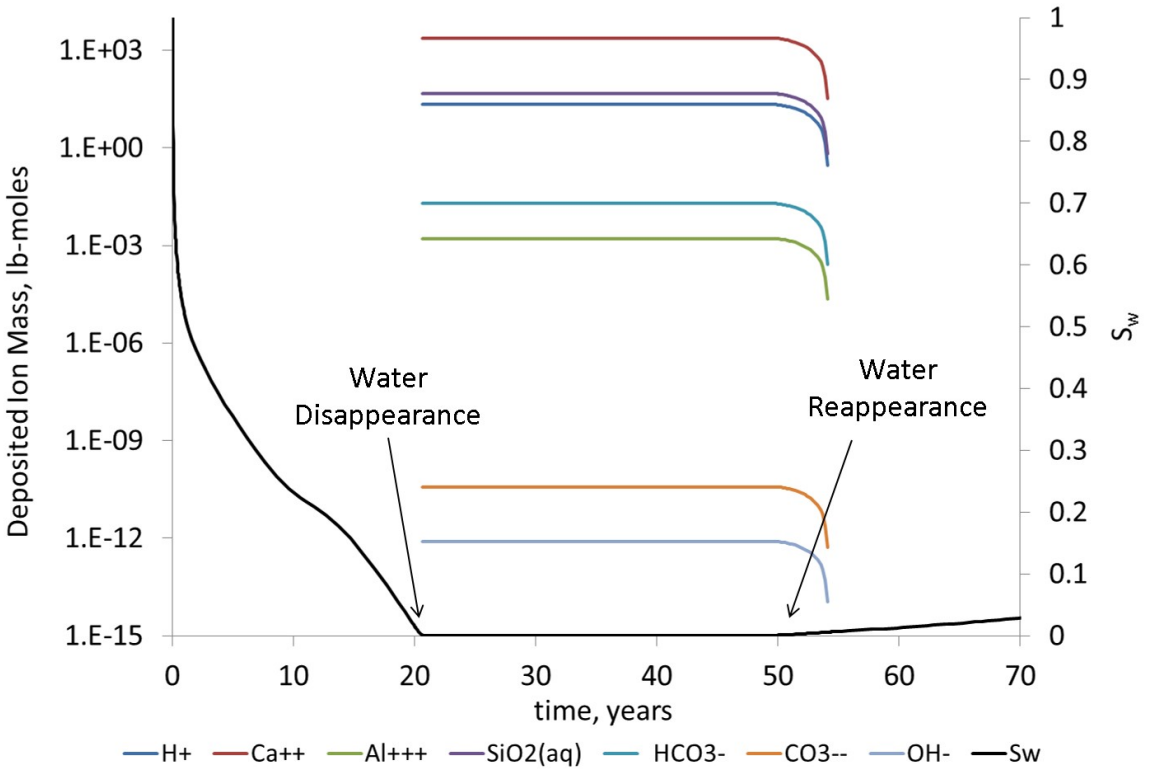

Figure 2.9: Evolution with time of the deposited ion mass (left axis) and water saturation (right axis) in the injection block.

shown). We see that CO_2 has migrated to the top of the aquifer and has also spread laterally. The fate of the injected CO_2 as a function of time is shown in Fig. 2.8. After 2000 years, more than half of the CO_2 is in the gas phase and only 10% has been mineralized. It is also apparent that there is very little mineralization for the first 200 years.

The distribution of the deposited mass in the well block, along with water saturation in this block, are shown in Fig. 2.9. We see that, after about 20 years of injection, the well-block water saturation reaches zero. In the absence of our deposition model (or some other treatment), the simulator would fail to converge, and the run would terminate at this point. With our deposition model, we see that deposited ions appear in the injection block when water disappears. This deposited mass begins to dissolve back into the water upon aqueous-phase reappearance at around 49 years (it

is difficult to see the slow decrease in deposited mass in Fig. 2.9 due to the log scale). The deposited mass has fully dissolved into the water phase by 54 years.

The 2000-year simulation for this case required about 14 hours of computation time employing two cores of a compute node with dual Quad-core Nehalem CPUs (Intel E5520 2.26 GHz), and 24 GB of memory. The model used 2300 time steps and required an average of only about 1.5 Newton iterations per time step.

2.3 Concluding remarks

In this chapter, we based our work on a general approach for incorporating chemical reaction modeling into a compositional reservoir simulator developed by Fan et al. [28]. The overall procedure is fully coupled and fully implicit. This framework handles kinetic, equilibrium, homogeneous and heterogeneous reactions. Jacobian-level transformations eliminate equilibrium reaction rates and provide equations describing element mass balances rather than the original (usual) component mass balances. Further manipulations at the level of the Jacobian matrix allow for efficiently reducing the size of the linear system that must be solved to compute the primary unknowns. Depending on the specifics of the problem, substantial savings at the linear solver level can be achieved through this transformation.

In this work we developed a new approach for treating components dissolved in the aqueous phase, such as ions, when the aqueous phase disappears or reappears. Specifically, we introduce and track an additional phase, referred to as the deposited phase. This phase contains deposited (as opposed to precipitated or mineralized) aqueous species and exists whenever the ionic strength of the aqueous phase would otherwise exceed its physical maximum. The model applies a kinetic treatment for transferring species from the aqueous phase to the deposited phase (and vice versa). In the absence of our model for the deposited phase, the simulator would fail to converge when the water phase disappears.

Numerical results were presented for several cases. These included a single-block model to illustrate our treatment of the deposited phase, a one-dimensional model, which allowed us to assess numerical convergence, and a three-dimensional model.

The latter contained 40,000 grid blocks and was characterized by a heterogeneous permeability field. Results demonstrated the ability of our procedure to simulate a complicated and somewhat realistic system, which included 12 components and six reactions, over a 2000-year time frame.

Chapter 3

Formulation Based on Overall-Composition Variables

Various compositional formulations have been developed based on the choice of the primary unknowns, which in turn impacts the solution algorithm. The multicomponent multiphase reactive displacement problem presented in terms of natural variables in Chapter 2 may be addressed using alternate nonlinear formulations. In this chapter, we propose a fully-implicit formulation to express this problem based on overall-composition variables. This scheme avoids variable switching, since the equations and variables are valid for all phase combinations, leading to less complexity in algorithm implementation. This formulation is thus inherently suitable for treating the water disappearance phenomenon encountered during simulation of CO_2 sequestration in aquifers discussed in Chapter 2. A drawback, however, is the higher cost of phase equilibrium calculations, as discussed in the following.

3.1 Chemical-compositional simulation

In this section the reactive transport model described in Chapter 2 is presented in terms of the overall-composition variables. The scheme is discussed in a manner that illustrates the extension of an existing compositional simulator to a reactive transport model.

3.1.1 Governing equations

To formulate the reactive transport system in terms of overall compositions, we first introduce the relevant variables. In contrast to the volume fractions (saturations) used in the natural-variable formulation, the phases are quantified in terms of the phase molar fractions, ν, in mass-variable formulations:

$$\nu_j = \frac{\rho_j S_j}{\sum_{k=1}^{n_p} \rho_k S_k}, \tag{3.1}$$

where ρ_k is the molar density of phase k. Fluid saturations may be consequently derived:

$$S_j = \frac{\nu_j/\rho_j}{\sum_{j=1}^{n_p} \nu_j/\rho_j}. \tag{3.2}$$

Fluid component masses are denoted primarily in terms of the overall compositions, which relate to phase compositions as follows:

$$z_i = \frac{\sum_{j=1}^{n_p} \rho_j S_j X_{ij}}{\sum_{k=1}^{n_p} \rho_k S_k} = \sum_{j=1}^{n_p} \nu_j X_{ij}, \quad i = 1, ..., n_f, \tag{3.3}$$

where X_{ij} is the molar fraction of fluid component i in phase j. The overall density for fluid phases is defined as a volume-averaged density:

$$\rho_T = \sum_{j=1}^{n_p} \rho_j S_j = \left(\sum_{j=1}^{n_p} \frac{\nu_j}{\rho_j} \right)^{-1}. \tag{3.4}$$

The mass conservation equations can now be written in terms of the overall compositions:

$$\frac{\partial}{\partial t} (\phi \rho_T z_i) + \nabla \cdot \mathbf{L} + q_i^W = \sum_{k=1}^{n_k} \upsilon_{i,k} r_k + \sum_{q=1}^{n_q} \upsilon_{i,q} r_q, \tag{3.5}$$

$$\frac{\partial C_i}{\partial t} = \sum_{k=1}^{n_k} \upsilon_{i,k} r_k + \sum_{q=1}^{n_q} \upsilon_{i,q} r_q, \tag{3.6}$$

where the nomenclature follows from Chapter 2, specifically $\mathbf{L}$ is the flux term given

in Eq. (2.3). Note that the statement of solid species mass conservation is the same as in the case of the natural-variable formulation.

Phase equilibrium and phase constraint equations are stated as in the natural-variable formulation. The reaction modeling terms and equations also follow directly from the discussion in Chapter 2. Specifically, a linear combination of the mass conservation equations is introduced in order to eliminate the equilibrium reaction rates. Consistent with our discussion on the natural-variable formulation, the reduction of reaction rates is performed utilizing the 'extended element stoichiometric matrix,' **E**, introduced in Eq. (2.11).

The mass concentration per bulk volume for fluid components and solids may be expressed in terms of the new variables as:

$$N_i = \phi \sum_{j=1}^{n_p} \rho_j S_j X_{ij} = \phi \rho_T z_i, \quad i = 1, ..., n_f, \tag{3.7}$$

$$N_{n_f+m} = C_m, \quad m = 1, ..., n_m, \tag{3.8}$$

which allows for framing the mass conservation equations in a matrix-vector format (equivalent to Eq. (2.8)):

$$\frac{\partial \mathbf{N}}{\partial t} + \mathbf{L} = \mathbf{S}_{n_s \times n_r} \mathbf{r}_{n_r \times 1}. \tag{3.9}$$

Following the methodology applied in the natural-variable treatment, the equilibrium rate annihilation matrix (**E**) given in Eq. (2.11) is utilized to eliminate the equilibrium reaction rates:

$$\frac{\partial (\mathbf{EN})}{\partial t} + \mathbf{EL} = \mathbf{ESr} = \begin{bmatrix} \mathbf{E}_1\mathbf{Sr} \\ \mathbf{E}_2\mathbf{Sr} \end{bmatrix} = \begin{bmatrix} \mathbf{0} \\ \mathbf{r}_k \end{bmatrix}_{(n_e+n_k)\times 1}. \tag{3.10}$$

This reduced set of equations consists of n_e element balance equations that are independent of any reaction rates, followed by n_k equations modeling the kinetic reactions.

The above $n_e + n_k = n_s - n_q$ equations are supplemented with n_q mass action law

equations governing the equilibrium reactions:

$$Q - K^{eq} = 0, \tag{3.11}$$

yielding the set of $n_{pr} = n_s$ primary equations, where n_{pr} stands for the number of primary equations/unknowns. This transformation is described in the following:

$$\left[\begin{array}{l} \text{Species Mass Conservation} \end{array}\right]_{n_s \times n_s} \Rightarrow$$

$$\left[\begin{array}{l} \left[\begin{array}{l} \text{Element Mass Conservation} \end{array}\right]_{n_e \times n_s} \\ \left[\begin{array}{l} \text{Kinetic Reaction Equations} \end{array}\right]_{n_k \times n_s} \\ \left[\begin{array}{l} \text{Equilibrium Reaction Constraints} \end{array}\right]_{n_q \times n_s} \end{array}\right]. \tag{3.12}$$

The n_s primary equations are solved simultaneously for all grid blocks (using the global Jacobian matrix and Newton iterations). The corresponding primary variables, $\mathbf{x}_p$, for isothermal problems are pressure, mineral concentrations, and all but one fluid species overall compositions, z_i, resulting in n_{pr} unknowns:

$$p, z_1, ..., z_{n_f-1}, C_1, ..., C_{n_m}. \tag{3.13}$$

The remaining constituent constraints and unknowns form the secondary set of equations and variables. Namely, the secondary variables, $\mathbf{x}_s$, include the remaining overall composition, phase molar fractions, and fluid phase compositions:

$$\begin{aligned} & z_{n_f}, \nu_1, ..., \nu_{n_p}, \\ & X_{ij}, \qquad i = 1, ..., n_f, \ j = 1, ..., n_p, \end{aligned} \tag{3.14}$$

yielding $n_{sec} = n_f n_p + n_p + 1$ variables, where n_{sec} is the number of secondary equations/unknowns. The following constraints are assembled and utilized as the set of

secondary equations:

$$z_i - \sum_{j=1}^{n_p} \nu_j X_{ij} = 0, \qquad i = 1, ..., n_f, \tag{3.15}$$

$$\sum_{i=1}^{n_f} (X_{ij} - X_{ik}) = 0, \qquad j, k = 1, ..., n_p, \quad j \neq k, \tag{3.16}$$

$$\sum_{j=1}^{n_p} \nu_j - 1 = 0, \tag{3.17}$$

$$\sum_{i=1}^{n_f} z_i - 1 = 0, \tag{3.18}$$

$$f_{ij} - f_{ik} = 0, \qquad i = 1, ..., n_f, \ j, k = 1, ..., n_p, \quad j \neq k, \tag{3.19}$$

resulting in $n_{sec} = n_f n_p + n_p + 1$ equations. Note that the reaction treatment entails a transformation of the n_s mass balance equations (see Eq. (3.10)), while the above set of secondary equations are not impacted by reaction modeling. An alternative choice of primary and secondary equations, where local reactions are classified as secondary equations, is discussed in Section 3.1.4.

The residuals of the primary equations are functions of both primary and secondary variables. For example, the mass balance equations depend on secondary variables, e.g., phase compositions. The chain rule is thus used to derive the entries of the Jacobian matrix:

$$\frac{d\mathbf{R}_p(\mathbf{x}_p, \mathbf{x}_s)}{d\mathbf{x}_p} = \frac{\partial \mathbf{R}_p}{\partial \mathbf{x}_s} \frac{d\mathbf{x}_s}{d\mathbf{x}_p} + \frac{\partial \mathbf{R}_p}{\partial \mathbf{x}_p}, \tag{3.20}$$

where $\mathbf{R}_p$ designates residuals corresponding to the primary equations, and $\mathbf{x}_p$ and $\mathbf{x}_s$ again represent the sets of primary and secondary variables.

In the fully-implicit scheme, the solution is computed for each time step as follows: In each Newton iteration, the global system of primary equations and variables is solved. Subsequently, the secondary, local equations are resolved on a grid-block basis for secondary variables, keeping the primary variables fixed. This is also interpreted as applying the flash algorithm, which entails finding the solution of small local nonlinear

problems. Once the secondary equations are solved, all fluid and solid properties are updated. The derivatives of the secondary unknowns with respect to the primary unknowns, required in Eq. (3.20), are also computed at this stage. In the following section, we outline a methodology for the calculation of these derivatives.

3.1.2 Treatment of the secondary constraints

In formulations based on overall compositions, the secondary equations are assumed to be fully converged for all Newton iterations. This is achieved by subjecting the solution of the primary equations (in the global stage) to constraints based on the secondary equations:

$$d\mathbf{R}_s(\mathbf{x}_p, \mathbf{x}_s) = \mathbf{0}, \tag{3.21}$$

where $\mathbf{R}_s$ denotes the vector of secondary residuals corresponding to Eqs. (3.15) through (3.19), and $\mathbf{x}_p$ and $\mathbf{x}_s$ are the primary and secondary unknowns introduced in Eqs. (3.13) and (3.14). Since at the beginning of each Newton iteration the secondary residuals are at convergence, the above criteria ensure that they remain within the range of tolerances while the primary variable space is searched in order to reach convergence of the primary equations. In contrast, the secondary equations are solved along with the primary equations in the natural-variable formulations, and consequently might not be at convergence during some Newton iterations. The solution path, along which the solution is sought, is thus different between the two formulations. Eq. (3.21) may be further expanded:

$$d\mathbf{R}_s(\mathbf{x}_p, \mathbf{x}_s) = \frac{\partial \mathbf{R}_s}{\partial \mathbf{x}_s}\frac{\partial \mathbf{x}_s}{\partial \mathbf{x}_p} + \frac{\partial \mathbf{R}_s}{\partial \mathbf{x}_p} = \mathbf{0}, \tag{3.22}$$

yielding the following equation as a means for computing $\partial \mathbf{x}_s / \partial \mathbf{x}_p$:

$$\frac{\partial \mathbf{x}_s}{\partial \mathbf{x}_p} = -\left(\frac{\partial \mathbf{R}_s}{\partial \mathbf{x}_s}\right)^{-1}\frac{\partial \mathbf{R}_s}{\partial \mathbf{x}_p}, \tag{3.23}$$

where $\partial \mathbf{x}_s / \partial \mathbf{x}_p$ and $\partial \mathbf{R}_s / \partial \mathbf{x}_p$ are $n_{sec} \times n_{pr}$ matrices and $\partial \mathbf{R}_s / \partial \mathbf{x}_s$ is an $n_{sec} \times n_{sec}$ matrix.

3.1.3 Jacobian-level transformation

Similar to our discussion for the natural-variable formulation, the implementation of reactive transport using the overall-composition variables does not require direct discretization of the full set of equations, if a compositional framework is already in place. Chemical reaction modeling may be integrated by modifying the Jacobian matrix and solution strategy. Many aspects of the compositional model will not be modified in this process, including the discretization techniques, phase behavior models, linear solver, and solution strategy for the treatment of nonlinear secondary equations.

In our fully-implicit algorithm, the component-based Jacobian matrix is fully constructed at each iteration, and a solution is found using Newton's method, similar to the natural-variable formulation. The following steps indicate the changes necessary for incorporation of chemical reactions into the simulator:

1. Construct the compositional Jacobian matrix (without reaction terms). This matrix will contain the derivatives of n_s (discretized) species mass balance equations with respect to $n_u = n_s = n_m + n_f$ unknowns. Build the corresponding residual vector.

2. Premultiply the rows of each nonzero Jacobian block by matrix $\mathbf{E}$ defined in Eq. (2.11). Apply the same multiplication to the residual vector. The result is $n_e + n_k$ equations, corresponding to Eq. (3.10). This gives matrix blocks of dimension $(n_e + n_k) \times n_u$.

3. To the above $n_e + n_k$ equations, add derivatives of n_q mass action laws (one for each equilibrium reaction). This gives a total of n_s equations (recall that $n_s = n_e + n_k + n_q$), constituting a matrix block of dimension $n_s \times n_s$.

4. Replace the rows in each Jacobian block by the n_s equations obtained in step 3.

5. Perform the chemical reaction Schur-complement reduction to reduce the $n_s \times n_s$ blocks to $n_{lpr} \times n_{lpr}$ blocks, where n_{lpr} is the number of primary variables at the linear level in the chemical-compositional system. This reduction procedure is explained in detail in the next section.

6. Proceed with linear solution, with Jacobian blocks of size $n_{lpr} \times n_{lpr}$, to obtain $\delta \mathbf{x}$.

7. Update the linear primary unknowns ($\mathbf{x}^{\nu+1} = \mathbf{x}^{\nu} + \delta \mathbf{x}$, where ν is the iteration index). Update the linear secondary variables based on linear primary variables, as usual in compositional simulation [18, 15].

8. Solve the nonlinear secondary equations for the values of corresponding secondary variables one grid block at a time, using local Newton iterations.

9. Using the updated variables, calculate the derivatives of nonlinear secondary variables, $\mathbf{x}_s$, with respect to $\mathbf{x}_p$.

10. Proceed to the next Newton iteration or time step after proper convergence check.

Steps 2 through 7 correspond to the additional calculations required for the chemical reaction module. The transformation of the Jacobian matrix in steps 1 to 4 is illustrated in Eq. (3.12), where the species mass balance equations are converted to element balance and chemical reaction equations.

3.1.4 Linear-level decoupling

As discussed earlier, in compositional reservoir simulation, the governing equations are often divided into primary and secondary equations [19, 133]. In our overall-composition variable formulation, we have thus far discussed a scheme for splitting the parameters and equations at the nonlinear level. An additional step of decoupling is possible at the linear level in reactive transport modeling due to the local nature of some chemical reactions. This is similar to the procedure discussed in Section 2.1.4 for the natural-variable formulation, although there are some key differences for the overall-composition formulation. A comprehensive comparison of the decoupling strategies for natural and overall-composition formulations will be provided later in this section.

In fact, the n_{pr} nonlinear primary equations, $\mathbf{R}_p$, can be further divided into global and local sets at the level of the Jacobian matrix, allowing additional decoupling. To distinguish between the two decoupling stages, we choose the following convention: the (nonlinear) primary and secondary unknowns denoted as $\mathbf{x}_p$ and $\mathbf{x}_s$ and

introduced in Eqs. (3.13) and (3.14) correspond to Eq. (3.10) and Eqs. (3.15)-(3.19), respectively. The linear primary and linear secondary variables are subsets of the nonlinear primary variables. Theses variables and their corresponding linear-level primary and secondary equations are explained in the following.

The full set of nonlinear primary residual equations, $\mathbf{R}_p$, may be divided into linear primary equations, $\mathbf{R}_{lp} = \mathbf{0}$, and linear secondary equations, $\mathbf{R}_{ls} = \mathbf{0}$. In other words $\mathbf{R}_p(\mathbf{x}) = [\mathbf{R}_{lp}(\mathbf{x}),\ \mathbf{R}_{ls}(\mathbf{x})]^T = \mathbf{0}$. The equations with no flux terms depend only on local variables of the grid block and are considered secondary equations. Accordingly, the nonlinear primary unknowns are split into linear primary and secondary sets: $\mathbf{x}_p = (\mathbf{x}_{lp}, \mathbf{x}_{ls})^T$.

The portion of the Jacobian matrix $\mathbf{J}$ corresponding to two adjacent cells 1 and 2 is written as follows:

$$\begin{bmatrix} \mathbf{J}_{11} & \mathbf{J}_{12} \\ \mathbf{J}_{21} & \mathbf{J}_{22} \end{bmatrix} \begin{bmatrix} \delta\mathbf{x}_p^1 \\ \delta\mathbf{x}_p^2 \end{bmatrix} = - \begin{bmatrix} \mathbf{R}_p^1 \\ \mathbf{R}_p^2 \end{bmatrix}. \tag{3.24}$$

Following the terminology introduced in Chapter 2, this can be rewritten as:

$$\begin{bmatrix} \mathbf{E}_{11} & \mathbf{F}_{11} & \mathbf{E}_{12} & \mathbf{F}_{12} \\ \mathbf{G}_{11} & \mathbf{H}_{11} & \mathbf{0} & \mathbf{0} \\ \mathbf{E}_{21} & \mathbf{F}_{21} & \mathbf{E}_{22} & \mathbf{F}_{22} \\ \mathbf{0} & \mathbf{0} & \mathbf{G}_{22} & \mathbf{H}_{22} \end{bmatrix} \begin{bmatrix} \delta\mathbf{x}_{lp}^1 \\ \delta\mathbf{x}_{ls}^1 \\ \delta\mathbf{x}_{lp}^2 \\ \delta\mathbf{x}_{ls}^2 \end{bmatrix} = - \begin{bmatrix} \mathbf{R}_{lp}^1 \\ \mathbf{R}_{ls}^1 \\ \mathbf{R}_{lp}^2 \\ \mathbf{R}_{ls}^2 \end{bmatrix}, \tag{3.25}$$

where for example, $\mathbf{R}_{lp}^1$ and $\mathbf{R}_{ls}^1$ are the linear primary and linear secondary residual vectors for cell 1, and $\mathbf{x}_{lp}^1$ and $\mathbf{x}_{ls}^1$ are the linear primary and linear secondary variables for cell 1. The rows of the Jacobian matrix corresponding to the $\mathbf{E}$ and $\mathbf{F}$ matrices represent the linear primary equations, and the $\mathbf{G}$ and $\mathbf{H}$ matrices hold the linear secondary equations. By definition, the linear (and nonlinear) secondary equations for a grid block are only functions of the unknowns in that specific cell, resulting in the zero submatrices seen in Eq. (3.25). The Jacobian block discussed in Section 3.1.3 corresponds to a single grid block, e.g., the submatrices $\mathbf{E}_{11}$, $\mathbf{F}_{11}$, $\mathbf{G}_{11}$ and $\mathbf{H}_{11}$.

Let n_{lpr} and n_{lsec} signify the number of linear primary and linear secondary variables.

Thus the $\mathbf{E}$ matrices have dimensions of $n_{lpr} \times n_{lpr}$, the $\mathbf{F}$ matrices are $n_{lpr} \times n_{lsec}$, the $\mathbf{G}$ matrices are $n_{lsec} \times n_{lpr}$, and the $\mathbf{H}$ matrices are $n_{lsec} \times n_{lsec}$.

Performing Schur reduction on the Jacobian matrix eliminates the $\mathbf{F}$ matrices through the application of Gaussian elimination. This step is generally a local operation and is accomplished one grid block at a time. The $\mathbf{H}_{11}$ and $\mathbf{H}_{22}$ matrices are inverted, followed by a linear transformation to yield:

$$\begin{bmatrix} \bar{\mathbf{E}}_{11} & \mathbf{0} & \bar{\mathbf{E}}_{12} & \mathbf{0} \\ \mathbf{G}_{11} & \mathbf{H}_{11} & \mathbf{0} & \mathbf{0} \\ \bar{\mathbf{E}}_{21} & \mathbf{0} & \bar{\mathbf{E}}_{22} & \mathbf{0} \\ \mathbf{0} & \mathbf{0} & \mathbf{G}_{22} & \mathbf{H}_{22} \end{bmatrix} \begin{bmatrix} \delta \mathbf{x}_{lp}^1 \\ \delta \mathbf{x}_{ls}^1 \\ \delta \mathbf{x}_{lp}^2 \\ \delta \mathbf{x}_{ls}^2 \end{bmatrix} = - \begin{bmatrix} \bar{\mathbf{R}}_{lp}^1 \\ \mathbf{R}_{ls}^1 \\ \bar{\mathbf{R}}_{lp}^2 \\ \mathbf{R}_{ls}^2 \end{bmatrix}, \tag{3.26}$$

where $\bar{\mathbf{E}}_{11} = \mathbf{E}_{11} - \mathbf{F}_{11}\mathbf{H}_{11}^{-1}\mathbf{G}_{11}$, and the submatrices $\bar{\mathbf{E}}_{12}$, $\bar{\mathbf{E}}_{21}$ and $\bar{\mathbf{E}}_{22}$ are derived in a similar manner.

Through the transformation in Eq. (3.26), the linear primary equations are decoupled from the linear secondary unknowns at the level of the Jacobian matrix. Subsequently, the global system is solved for linear primary equations/unknowns only. Once the global solution is computed, the linear secondary variables can be calculated locally, potentially in parallel and thus more efficiently.

In order to perform the linear-level equation classification, let n_{kf} signify the number of kinetic modeling equations involving flow terms. The linear secondary equations are the local ones representing chemical reactions in Eq. (3.26), and include all equilibrium reaction constraints as well as the kinetic reaction modeling equations independent of flux terms. The number of linear secondary equations is thus given by $n_{lsec} = n_q + n_k - n_{kf}$, and the number of primary equations is $n_{lpr} = n_e + n_{kf}$, since $n_s = n_e + n_q + n_k$. Generally, n_{kf} is significantly less than $n_k + n_q$, leading to a considerably smaller linear system that is far less expensive to solve. A discussion is given in [28] on the impact of a similar decoupling approach on solution performance under the natural-variable formulation. Note that in the problem of CO_2 sequestration in saline aquifers, all the equilibrium and kinetic mineral reaction equations are local (no flux terms), i.e., $n_{kf} = 0$.

Following Fan et al. [28], we introduced two different decoupling scenarios under the natural-variable formulation in Section 2.1.4, namely the 'reaction-coupled' and the 'local-reactions-decoupled' methods. In the overall-composition variable formulation discussed here, Eq. (3.24) is equivalent to the global/primary portion of the problem under the 'reaction-coupled' scheme. In other words, the nonlinear decoupling discussed in Sections 3.1.1 and 3.1.2 is generally achieved purely algebraically and at the level of the Jacobian matrix under the natural-variable formulation. The linear decoupling scheme in Eq. (3.26) further reduces the global system of equations to one equivalent to the 'local-reactions-decoupled' model. We emphasize that the nonlinear solution path trajectories under the natural and overall-composition variable formulations are generally not the same, as discussed in Section 3.1.2. Unlike linear-level decoupling, which does not influence the nonlinear solution path, the nonlinear-level decoupling in the overall-composition variable formulation implies convergence of the secondary equations at all Newton iterations, which causes a deviation in the nonlinear solution path from that observed under the natural-variable formulation.

The approach discussed in this work is fully coupled and fully implicit. The decoupling at the level of the Jacobian matrix does not influence the performance of the nonlinear solver. This linear-level reduction, however, allows for decoupling of the global set of equations from the local equations, shrinking the linear problem, and thus significantly enhancing the computational efficiency.

Various solutions can be formulated where some or all of the linear decoupling discussed above is accomplished at the nonlinear level [107]. As an example, the n_q equations governing the equilibrium reactions, Eq. (3.11), may be added to the set of nonlinear secondary equations, Eqs. (3.15) through (3.19), leaving the $n_e + n_k$ equations in Eq. (3.10) as the only (nonlinear) primary equations. In this scenario, the linear-level decoupling of the $n_k - n_{kf}$ local kinetic reaction modeling equations is recommended. In fact, all local chemical reactions may be decoupled at the nonlinear level, leaving the linear-level decoupling unnecessary. Note that any reaction decoupled at the nonlinear level is solved along with flash calculations when resolving the secondary set of equations. However, these models have the fundamental drawback of making the size and structure of the Jacobian matrix dependent on the chemistry,

as we now illustrate.

Consider the problem of CO_2 sequestration in saline aquifers modeled with any of the reaction sets given in this work. At zero water saturation, the (homogeneous) equilibrium as well as the (heterogeneous) kinetic reactions no longer apply ($r_k = r_q = 0$). Under these circumstances, the transformation in Eq. (3.10) is invalid. The original n_s species balance equations given in Eqs. (3.5) and (3.6) hold and will be used directly. If the equilibrium reactions are decoupled at the nonlinear level, in the absence of the water phase the number of Jacobian rows/columns corresponding to the grid block would increase from $n_e + n_k$ to $n_s = n_e + n_k + n_q$. This, however, defeats a primary advantage of the overall-composition variable formulation; namely, avoiding variable substitution by employing fixed equations and unknowns for all grid blocks for all phase combinations. We thus do not recommend decoupling chemical reactions at the nonlinear level, even though it was briefly investigated in this work.

In our experience, the classification of the equilibrium reaction constraints as nonlinear secondary equations, which requires their full convergence at all Newton iterations, has a negative impact on the convergence of a fully-implicit multiphase overall-composition variable formulation applied to geochemistry problems. However, we were able to establish satisfactory convergence behavior under simplifying assumptions, e.g., small reaction systems, more basic reaction rates, and the assumption of solution ideality.

In the following section, we investigate a new formulation which allows us to take advantage of the favorable features in both the natural and overall-composition variable formulations.

3.1.5 A hybrid formulation

Thus far, two distinct reactive transport formulations have been discussed in this work. The first is the natural-variable formulation, along with a deposition modeling technique introduced as a treatment for phase disappearance. The second is the overall-composition variable formulation introduced in this chapter. Each of these

schemes has advantages and drawbacks. For example, the natural-variable formulation is far less expensive in terms of thermodynamic calculations in grid blocks experiencing a multiphase regime, while the overall-composition variable formulation treats phase disappearance in a more straightforward fashion. In fact, because some aqueous species, e.g., ions, exist only in the aqueous phase, in the absence of this phase, no subset of natural variables can fully represent mass conservation. Overall compositions, on the other hand, are a valid set of variables to describe the physics for any fluid phase combination.

A combination of the two methods is thus favorable in the context of CO_2 sequestration. The most basic approach to accomplish this is to use natural variables throughout the reservoir, except for the blocks likely to experience phase disappearance, which utilize overall compositions. This, however, can prove cumbersome to implement in an existing simulator due to the major contrasts between the two approaches, e.g., in the treatment of the secondary equations and variables.

We thus propose a hybrid of the two formulations as an alternative, more feasible, technique. In this setup, natural variables are employed by all grid blocks except for those in single-phase gas mode, which use overall-composition variables. In other words, once single-phase gas is detected, the grid block switches to overall compositions. If a two-phase state is detected subsequently, the algorithm switches back to natural variables.

In the single-phase gas mode, the nonlinear-level secondary equations and operations are unnecessary for the overall-composition variable formulation. Moreover, in the CO_2 sequestration problems considered in this work, all reactions involve the aqueous phase. No reaction treatment is thus necessary in the absence of the water phase. This absence of chemical reactions renders the linear-level Schur-complement, discussed in Section 3.1.4, unnecessary in our problem and in the single-phase gas mode. The hybrid approach thus requires only a minimal modification of the natural-variable formulation. This new formulation has been integrated into our simulator and will be assessed in select case studies.

3.1.6 Implementation considerations

In this section we describe details of the numerical implementation that are of particular importance for geological CO_2 sequestration applications. A distinct characteristic of these problems is the significant scale variations in the aqueous component concentrations, i.e., the presence of trace amounts of mass in the aqueous phase. To enhance the nonlinear solver performance, we have opted to employ the logarithm of the mass fractions $(\log(X_{iw}), \log(z_i))$ as the variables of choice, as opposed to the mass fractions themselves (X_{iw}, z_i). In order to maintain simplicity, we have avoided integrating this extra step within the description of the formulations. The implementation in AD-GPRS, however, offers the flexibility to incorporate the logarithm of mass fractions for an arbitrary set of components as specified by the user. In our case studies, mass faction variables corresponding to all aqueous components undergo the logarithm transformation, except for CO_2 and H_2O.

For all the case studies in this work, phase behavior is modeled through a modified Peng-Robinson equation of state [60, 26]. In the flash calculations, we account for the masses of all the aqueous species. In the absence of such consideration, the inconsistency at the nonlinear level can negatively impact the convergence behavior, especially when crossing the phase boundaries. Moreover, taking this mass into account when updating the derivatives of the primary variables with respect to secondary variables (Eq. (3.23)), has proven critical in maintaining the convergence of the overall-composition variable formulation.

The introduction of aqueous species results in slight deviations in aqueous CO_2 and H_2O concentrations compared to the two-phase, two-component CO_2-H_2O system. In the natural-variable formulation, the saturations and phase compositions are resolved at the global level. The global solution is thus impacted by deviations in the aqueous concentrations. These deviations, though generally small, may lead to nonphysical values as the water saturation diminishes. Moreover, phase disappearance requires variable switching under the natural-variable formulation. The combination of these two complications may hinder the Newton iterations, and even lead to convergence failure. As a result, when experiencing water disappearance and reappearance in this formulation, the tolerances on the phase equilibrium residuals given in Eq. (2.6) might

need to be slightly relaxed for grid blocks experiencing the change in phase status. Note that this is only a consideration in the presence of the aqueous species, and not in the two-component CO_2-H_2O system.

Calculations concerning flash and thermodynamic phase stability tests are, however, never subject to tolerance relaxation. In other words, in the case of the overall-composition variable formulation, the phase equilibrium calculations are performed with consistent accuracy at all times. In the overall-composition variable formulation, the aqueous concentration deviations are encountered only during the local flash calculations, where they are easier to overcome. Moreover, the absence of variable switching ensures consistency across the nonlinear solver iterations. Superior convergence is thus observed during water disappearance and reappearance under the overall-composition variable formulation compared to the natural-variable formulation.

Kinetic reaction rates generally do not take into account all the aspects of multiphase flow in porous media, and should be modified accordingly. As an example, the reaction rate in Eq. (A.5) should be multiplied by porosity and water saturation when integrated into the mass balance equations. Moreover, all reaction modeling is turned off at trace water saturation values of 1-2%. At such trace amounts, the water is likely to exist as a disconnected phase, where the assumptions behind the kinetic and equilibrium reactions may not hold [78].

3.2 Results for CO_2 storage simulations

The treatment presented in this chapter may be applied to a variety of reactive transport phenomena. In this chapter, we focus on the problem of CO_2 sequestration in saline aquifers. We examine the performance of the proposed treatment based on our fully-implicit implementation in Stanford's Automatic Differentiation-based General Purpose Research Simulator (AD-GPRS).

3.2.1 Comparison of reactive-transport formulations

We start with a comparison of the natural-variable formulation introduced in Chapter 2 and the overall-composition variable formulation discussed in this chapter. The two models offer different treatments to solve the same nonlinear problem.

We consider a two-dimensional model in the x-y plane consisting of 10×10 grid blocks, each of dimensions 10 m $\times$ 10 m $\times$ 10 m. The water-rock interactions are modeled through three equilibrium and three kinetic reactions. This chemical system, shown in Table 3.1, was also used in Chapter 2. It is expressed in terms of nine aqueous species and three minerals, and involves six chemical elements in total.

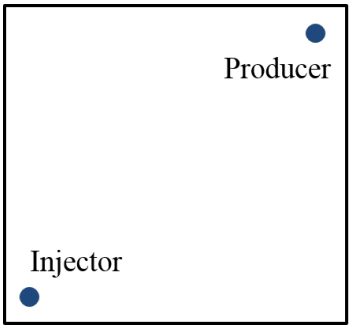

Figure 3.1: Schematic of the two-dimensional model with an injection and a production well.

Table 3.1: Chemical reaction system used in case studies

Reaction #	Type	Reactions
1	Equilibrium	$CO_2(aq) + H_2O = H^+ + HCO_3^-$
2	Equilibrium	$CO_3^{2-} + H^+ = HCO_3^-$
3	Equilibrium	$H_2O = H^+ + OH^-$
4	Kinetic	$\text{Anorthite} + 8\,H^+ = 4\,H_2O + Ca^{2+} + 2\,Al^{3+} + 2\,SiO_2(aq)$
5	Kinetic	$\text{Calcite} + H^+ = Ca^{2+} + HCO_3^-$
6	Kinetic	$\text{Kaolinite} + 6\,H^+ = 5\,H_2O + 2\,Al^{3+} + 2\,SiO_2(aq)$

Pure CO_2 is injected at 10,000 m^3/d into the brine-filled aquifer in the lower left

corner, as seen in Fig. 3.1. A production well produces at constant bottomhole pressure in the opposite corner of the reservoir, preventing pressure buildup. The reservoir has porosity of 18% and permeability of 100 md, and the initial pressure is 118 bar.

The model is simulated using both the natural and overall-composition reactive-transport formulations, with a maximum time step of 1 day and the same time stepping scheme. The pressure and saturation profiles after 100 days of injection (0.15 pore volume injected) are presented in Fig. 3.2. The negligible difference between the results from the two formulations, shown in Fig. 3.2, is consistent during the entire simulation and is observed for all physical properties, indicating a very close match.

The numerical performance of the two schemes is compared in Table 3.2, both for the reactive-transport problem described in Table 3.1 and a two-component (CO_2 and H_2O) compositional simulation free of reactions. In the two-component simulation, the overall-composition variable formulation requires 60% more phase equilibrium calculations compared to the natural-variable formulation. This cost difference is due to the difference in the treatment of phase equilibrium. The overall-composition variable formulation requires flash calculations at all Newton iterations for all grid blocks where a two-phase state is detected in the phase stability test [76]. The natural-variable formulation, however, skips the flash calculations when a block remains in the two-phase state, as it tracks the phase fractions directly in terms of the phase saturations.

Integrating chemical reactions into this multiphase problem introduces significant nonlinearity. Moreover, complexity arises due to physical phenomena occurring at very different time scales. As observed in Table 3.2, the overall-composition variable formulation requires 2.3 times the flash computations necessary for the natural-variable formulation. This formulation utilizes a more restricted solution space because it keeps the secondary equations at convergence in all Newton iterations, which may render the numerical cost more sensitive to nonlinearity.

Finally, in Table 3.3, the numerical performance of a spatially refined version of the

Table 3.2: Numerical performance of the algorithms when applied to the reactive transport system described in Table 3.1. The model was simulated for 100 days. No wasted time steps are experienced.

Numerical scheme	Time steps	Newton iterations	Avg. linear solver iters. per Newton iter.	Avg. flash iters. per Newton iter. per block
Compositional simulation (2 components)				
Natural variables	117	1019	1.86	0.47
Mass variables	117	1022	1.86	0.76
Reactive compositional simulation described in Table 3.1 (12 components)				
Natural variables	117	1023	1.92	0.48
Mass variables	117	1031	1.99	1.10

Table 3.3: Numerical performance of the algorithms for a spatially refined case of the problems considered in Table 3.2. The models were simulated for 100 days. No wasted time steps were experienced.

Numerical scheme	Time steps	Newton iterations	Avg. linear solver iters. per Newton iter.	Avg. flash iters. per Newton iter. per block
Compositional simulation (2 components)				
Natural variables	117	1095	1.92	0.50
Mass variables	117	1096	1.95	0.73
Reactive compositional simulation described in Table 3.1 (12 components)				
Natural variables	117	1103	2.07	0.53
Mass variables	117	1095	2.10	1.01

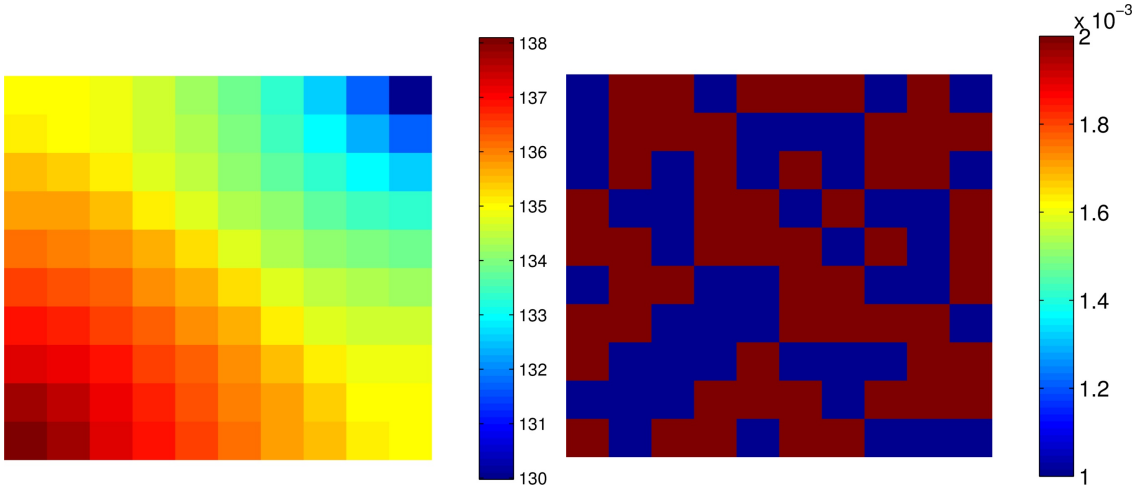

(a) Pressure profile at 100 days (bar) (b) Difference between the pressure profiles (bar)

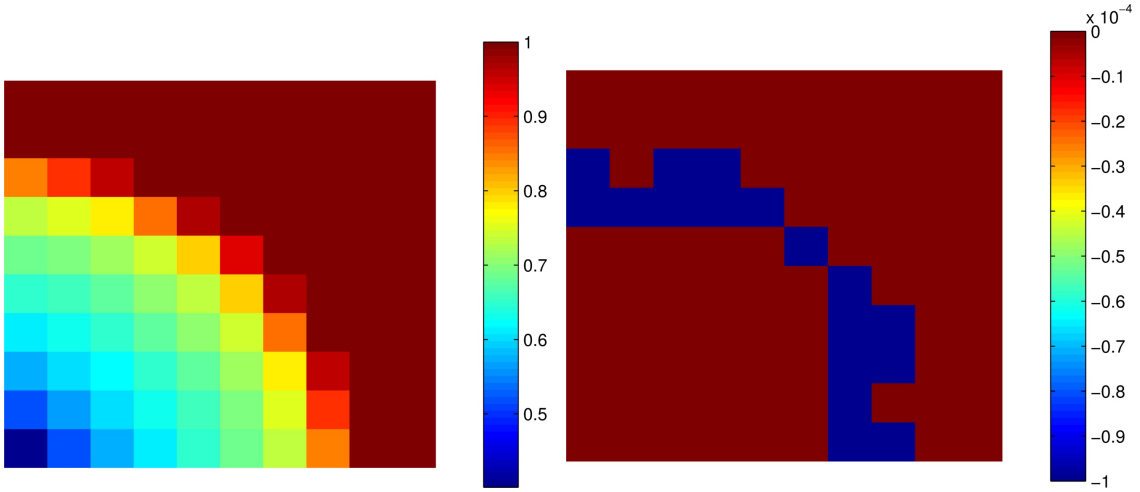

(c) Saturation profile at 100 days (d) Difference between the saturation profiles

Figure 3.2: Pressure (top) and saturation (bottom) responses calculated for the reactive transport system described in Table 3.1.

model considered in Table 3.2 is presented. Each grid block in the original model is divided into four blocks, yielding 20×20 blocks of 5 m $\times$ 5 m $\times$ 10 m. All other parameters are unchanged. Observations in this case are consistent with those for the 10×10 model. The overall-composition variable formulation again has more intensive flash calculation requirements, particularly in the presence of chemical reactions. In the next section, we will examine our implementation of the various reactive transport models when crossing thermodynamic phase boundaries in a geochemical system.

3.2.2 Crossing phase boundaries in reactive transport

We now introduce the additional complication of (aqueous) phase disappearance and reappearance to the reactive transport problem. A one-dimensional, 10-block model is used. Pure CO_2 is injected from one end, while a production well located on the opposite end operates at constant bottomhole pressure. Grid blocks are of dimensions 10 m $\times$ 10 m $\times$ 10 m. The initial reservoir pressure is 118 bar, porosity is 18%, and permeability is 100 md.

The reactive-transport model is simulated employing three distinct numerical formulations. The first is the natural-variable formulation with the deposition model discussed in Chapter 2 used to treat phase disappearance. The second is the overall-composition variable formulation introduced in this chapter. The third scheme is a hybrid of the two treatments as discussed in Section 3.1.5. This formulation uses natural variables in all phase combinations, except for single-phase gas (critical CO_2 phase). In the case of single-phase gas, the overall-composition variables are applied.

A maximum time step of 2.5 days, and similar time stepping schemes are used in all the cases. Pure CO_2 is injected for 290 days (average CFL number of 3.7), at which point both wells are shut-in. The aqueous phase saturation reaches zero in the injection well grid block before 290 days (at about 21.5 reservoir pore volume fluid injected). As the reservoir equilibrates after the wells are shut-in, water imbibes back into the injection well grid block due to capillary pressure effects.

Two-component compositional model

As in the previous example, in order to distinguish between the impact of different physical effects on the numerical behavior, we start with a two-phase, two-component, CO_2-H_2O compositional model free of chemical reactions. A comparison of the time stepping behavior for the natural and overall-composition variable formulations is given in Fig. 3.3. In Fig. 3.3(a) the time step sizes (days) and injection well grid block water saturation are given over a 400 day period. The middle portions of these plots are magnified in Fig. 3.3(b). As is evident from the figures, the two methods closely follow the same trend of time step size. The first time step cut at approximately 55 days is associated with breakthrough of the CO_2 injection stream, and the second

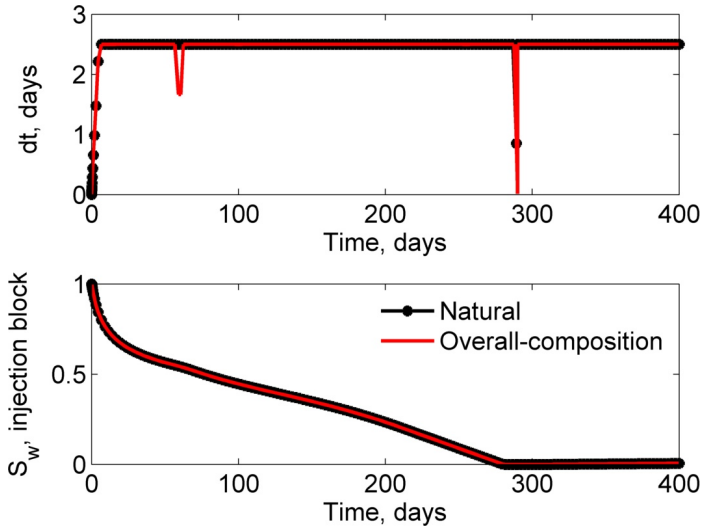

(a) Time step sizes and the injection block aqueous saturation

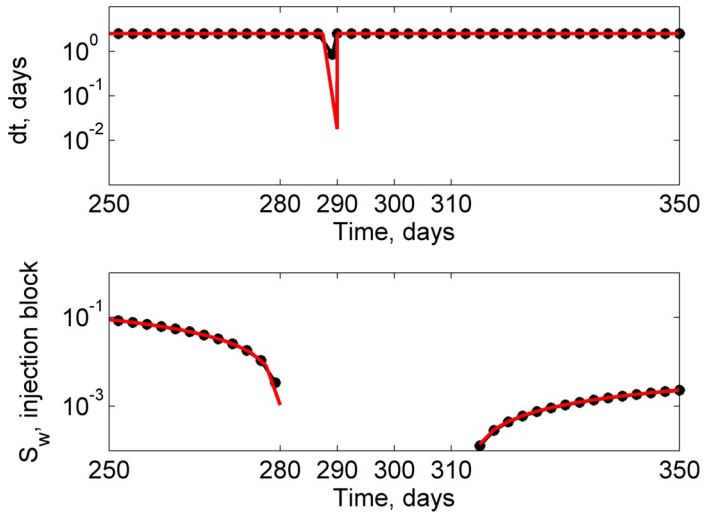

(b) Magnified plot of time stepping and injection block aqueous saturation

Figure 3.3: Comparison of the time stepping behavior for natural and overall-composition variable formulations when crossing phase boundaries in a two-phase, two-component problem. The components are CO_2 and H_2O and no chemical reactions are included.

one at approximately 290 days is due to water disappearance in the injection well grid block.

Nine-component compositional model

To investigate the impact of trace amounts of dissolved mass on the nonlinear behavior, we introduce seven aqueous species into the water phase. These aqueous species are H^+, OH^-, HCO_3^-, CO_3^{2-}, Ca^{2+}, Al^{3+}, and SiO_2(aq). The corresponding geochemical reactions are not incorporated at this stage. The only reaction included is the deposition reaction if necessary (see Chapter 2). The aqueous species are present in trace amounts and at different concentration scales with respect to each other. The concentrations of these species are initialized to values that are typical of geochemical systems of interest, and they vary from 8.47×10^{-11} to 2.52×10^{-2} mol/kg.

Fig. 3.4 presents the results using the natural, overall-composition, and hybrid formulations. As before, the plots in Fig. 3.4(b) magnify a portion of the data shown in Fig. 3.4(a). It is apparent from the data that the overall-composition variable formulation suffers from significant time step cuts when crossing the phase boundary (going from two-phase to single-phase gas). This problem, absent in the base compositional case in Fig. 3.3, is due to the presence of trace amounts of aqueous species.

To further clarify the observed behaviors, the overall molar fraction in the water phase assigned to the aqueous species (species other than CO_2 and H_2O) is plotted versus time in Fig. 3.5 for the overall-composition variable formulation. As the water phase disappears, the CO_2 and H_2O masses in this phase decrease proportional to the water saturation. By contrast, in the absence of any reactions, the mass of ions is left behind in the residually small volume of water. This leads to the total molar fraction of aqueous species reaching a value of one at the limit of zero water saturation, as seen in Fig. 3.5 at 290 days.

Mass conservation at or near water disappearance is achieved through deposition modeling when using the natural-variable formulation. On the other hand, the overall-composition variable formulation needs no additional modification to handle this phenomenon. Nonetheless, time step cuts might be necessary, as observed in this example, and may be explained as follows. While in our implementation the aqueous species concentrations are accounted for in the flash calculations, the equation of state was not originally developed to model the aqueous solution under study, and has only

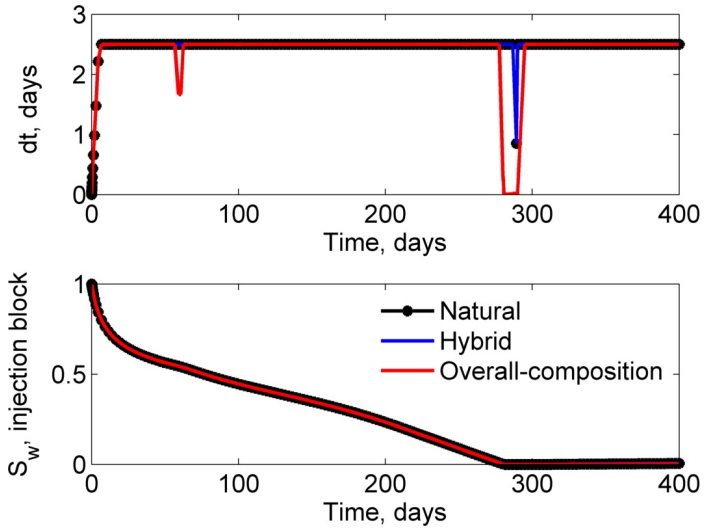

(a) Time step sizes and the injection block aqueous saturation

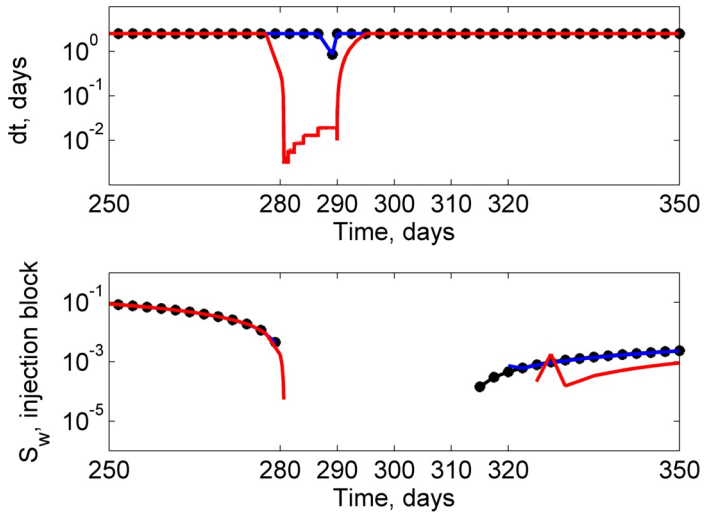

(b) Magnified plot of time stepping and injection block aqueous saturation

Figure 3.4: Time stepping behavior of three compositional numerical treatments when crossing thermodynamic phase boundaries. The components include H_2O, CO_2 and seven ions at very small concentrations. No chemical reactions are included.

been modified subsequently for such scenarios. In fact, at the point of water disappearance, alternative physical phenomena may govern the fate of the aqueous species. As a result, our model experiences complications at the limit of water disappearance.

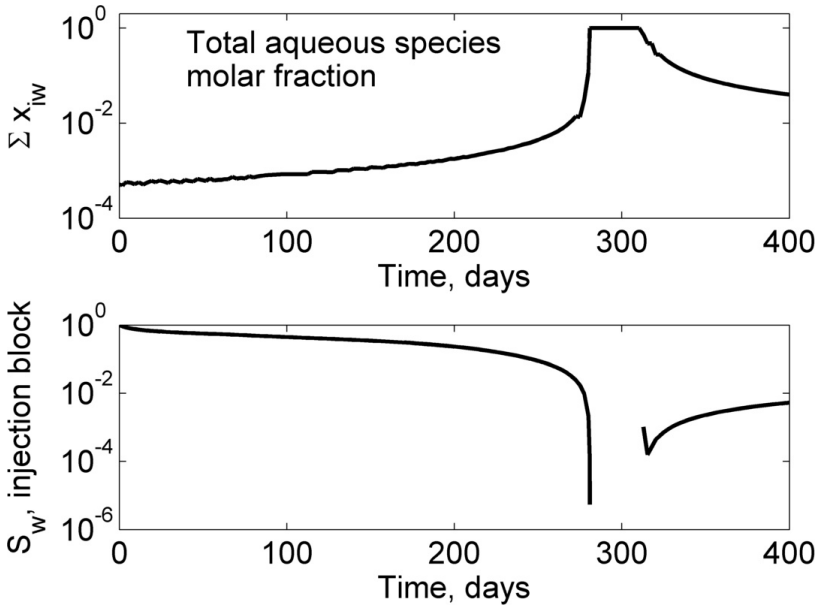

Figure 3.5: Total molar fraction in the water phase assigned to aqueous species (species other than CO_2 and H_2O), designated ΣX_{iw} (top), and water saturation (bottom). Data are shown for the injection well grid block. Overall-composition variable formulation is applied.

From Fig. 3.4, it appears that the natural variables handle the water disappearance more easily than the other formulations. This formulation, however, applies slightly relaxed tolerances on the phase equilibrium equations for residual water saturations smaller than 2%, as discussed in Section 3.1.6. In the absence of such a relaxation, the algorithm may be unable to converge. As a result, the overall-composition variable formulation in fact offers improved capabilities in handling water disappearance/reappearance. See Section 3.1.6 for further discussion.

Finally, as is apparent from Fig. 3.4, the hybrid formulation is able to instantaneously dissolve the aqueous material back into the water phase at the time of water reappearance, with no convergence problems. As mentioned in Chapter 2, complications may be observed under the natural-variable formulation when attempting to instantaneously dissolve ions at the point of water reappearance. In fact, these issues prompted the introduction of the deposition reaction rate, Eq. (2.23), to gradually

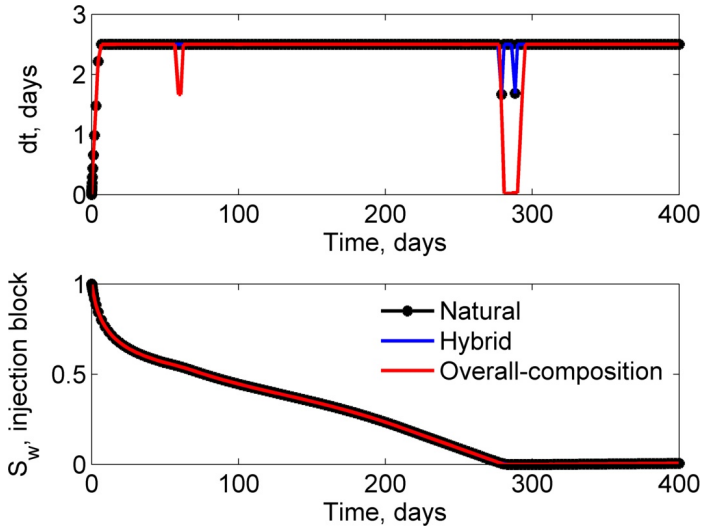

(a) Time step sizes and the injection block aqueous saturation

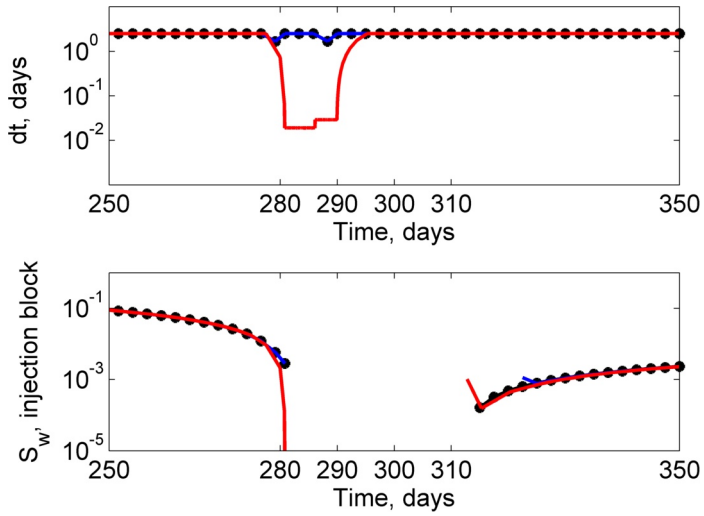

(b) Magnified plot of time stepping and injection block aqueous saturation

Figure 3.6: Comparison of the time stepping behavior of three compositional numerical treatments when crossing the thermodynamic phase boundaries. The reaction system is described in Table 3.1.

dissolve the material into the water phase. Nonetheless, that treatment is not necessary in the hybrid method (in the case studies investigated) for the following reason.

In this formulation, the two-phase region is detected in the overall-composition variable algorithm, taking into account the small mass of aqueous species, at which point the algorithm switches to natural variables. Under the natural-variable formulation, however, the two-phase status is established without taking the mass of aqueous species into account, as this mass is stored in independent variables. Instantaneous dissolution of the deposited mass into the water phase thus creates an inconsistency, which may hinder convergence.

Twelve-component reactive transport model

At this point, three minerals, anorthite, calcite, and kaolinite, are incorporated into the model along with the chemical reactions given in Table 3.1. Results for the three numerical schemes are presented in Fig. 3.6. The general trend in time stepping remains similar to the previous case for all of the formulations. A closer look at the numerical performance data is warranted at this point.

The numerical performance for all of the various scenarios and formulations presented thus far is given in Table 3.4. We first discuss the top two blocks of data, neither of which involves chemical reactions. The numerical performance of the overall-composition variable formulation is influenced dramatically by the presence of trace amounts of aqueous species, even in the absence of reaction modeling. In fact, the number of time steps increases by 55% between the first two scenarios. Moreover, the overall numerical cost grows by an even larger factor, as the average number of linear and nonlinear solver iterations per time step almost triples. Phase equilibrium calculations are also more expensive in the second and third sets of results due to the challenges introduced by the aqueous species; this additional cost is more drastic in the overall-composition approach, consistent with our discussion thus far.

The last block in Table 3.4 reports the numerical performance results for cases with chemical reactions. A larger degree of nonlinearity is now present, with the kinetic reaction rates and equilibrium reactions placing algebraic constraints on the aqueous species concentrations. The numerical performance is, however, generally superior to that of the second set of scenarios. Because the mass of aqueous species varies in the reactive case, but remains nearly at initial conditions in the non-reactive setup,

Table 3.4: Numerical performance of the three algorithms with maximum time step of 2.5 days. Data given for a 4290-day simulation. Wasted time steps and Newton iterations are reported in parentheses.

Numerical scheme	Time steps	Newton iterations	Avg. flash iters. per Newton iter. per block
Two component compositional simulation, no reactions, Fig. 3.3			
Natural	1734	2120	0.10
Overall-compositions	1735(2)	2138(40)	1.29
Nine component compositional simulation, no reactions, Fig. 3.4			
Natural	1734	2133	0.10
Overall-compositions	2694(966)	9879(19185)	2.21
Hybrid	1734	2155	0.10
Twelve component reactive transport simulation, Fig. 3.6			
Natural	1734(1)	2158(5)	0.10
Overall-compositions	2151(424)	2573(8480)	2.41
Hybrid	1734(1)	2173(5)	0.10

Table 3.5: Numerical performance of the three algorithms with maximum time step of 0.5 day. Data given for a 4290-day simulation. Wasted time steps and Newton iterations are reported in parentheses.

Numerical scheme	Time steps	Newton iterations	Avg. flash iters. per Newton iter. per block
Two component compositional simulation, no reactions, Fig. 3.3			
Natural	8594	8931	0.04
Overall-compositions	8594	9009	1.12
Nine component compositional simulation, no reactions, Fig. 3.4			
Natural	8594	9470	0.04
Overall-compositions	9599(1028)	19782(20526)	2.12
Hybrid	8594	9610	0.05
Twelve component reactive transport simulation, Fig. 3.6			
Natural	8594	9014	0.04
Overall-compositions	9050(479)	10067(9580)	2.28
Hybrid	8595(1)	9145(3)	0.05

Table 3.6: Numerical performance of the algorithms for a spatially refined model. The same reservoir as in Table 3.4 is divided into 20 grid blocks. A maximum time step of 2.5 days is used. The water disappears in the injection well block before 160 days, when the injection ceases. Data given for a 4160-day simulation. Wasted time steps and Newton iterations are reported in parentheses.

Numerical scheme	Time steps	Newton iterations	Avg. flash iters. per Newton iter. per block
Two component compositional simulation, no reactions, Fig. 3.3			
Natural	1682	2041	0.10
Overall-compositions	1683(3)	2055(60)	1.29
Nine component compositional simulation, no reactions, Fig. 3.4			
Natural	1685(5)	2192(100)	0.10
Overall-compositions	2418(741)	10595(14647)	2.22
Hybrid	1683(1)	2205(20)	0.10
Twelve component reactive transport simulation, Fig. 3.6			
Natural	1683(2)	2083(40)	0.11
Overall-compositions	1864(187)	2250(3740)	2.37
Hybrid	1684(3)	2079(60)	0.10

the comparison between the two models is not definitive and may depend on the particular reaction set and scenario.

Finally, comparing the results of the two-component system against the reactive-transport case demonstrates the advantages of our fully-implicit scheme. Roughly the same number of time steps and solver iterations is required for the natural-variable and hybrid formulations. The overall-composition variable formulation experiences time step cuts at the point of water disappearance as discussed before, but is otherwise capable of maintaining a time step size similar to that in the non-reactive model.

In order to investigate the persistence of the above observations, numerical performance is further assessed for temporally and spatially refined cases in Tables 3.5 and 3.6. In Table 3.5, a maximum time step of 0.5 day is utilized as opposed to 2.5 days. In Table 3.6, the base reservoir model is divided into 20 grid blocks instead of 10. Similar conclusions as before can be made for both refined cases. The data in Table 3.5 demonstrate a reduction in the average cost of phase equilibrium calculations per Newton iteration for smaller time steps under the natural-variable

formulation as well as for the hybrid model. The overall cost of phase equilibrium calculations, however, increases for both of these formulations due to the rise in the number of Newton iterations.

3.2.3 Results for a three-dimensional case

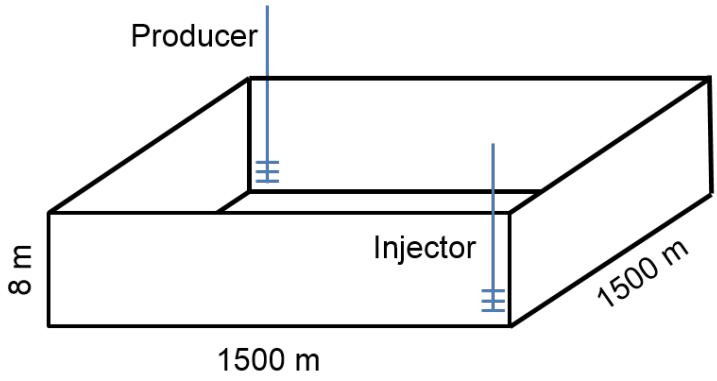

Figure 3.7: Three-dimensional model with injection and production wells.

In this section, the various reactive transport formulations discussed so far are applied to a three-dimensional reservoir model. The reaction system in Table 3.1 is employed for this set of results. The 1500 m $\times$ 1500 m $\times$ 8 m reservoir is divided into $15 \times 15 \times 4$ grid blocks, yielding a total of 900 blocks. An injection well injects pure CO_2 at a bottom corner of the reservoir. A production well, located across the reservoir from the injection well, produces at the bottom of the reservoir at constant bottomhole pressure. The model and wells are depicted in Fig. 3.7. The initial reservoir pressure is 118 bar, porosity is 18%, and permeability is 100 md.

The model is simulated using the three numerical schemes described earlier. A maximum time step of 1 year, and equivalent time stepping schemes, are used for all runs. Pure CO_2 is injected for 57 years, at which point both wells are shut-in. The water phase disappears in the injection well grid block just before the shut-in. Following the well shut-in, the water phase imbibes into the injection well grid block due to capillary pressure effects.

In Fig. 3.8, the saturation profile is shown at the point of shut-in, along with the

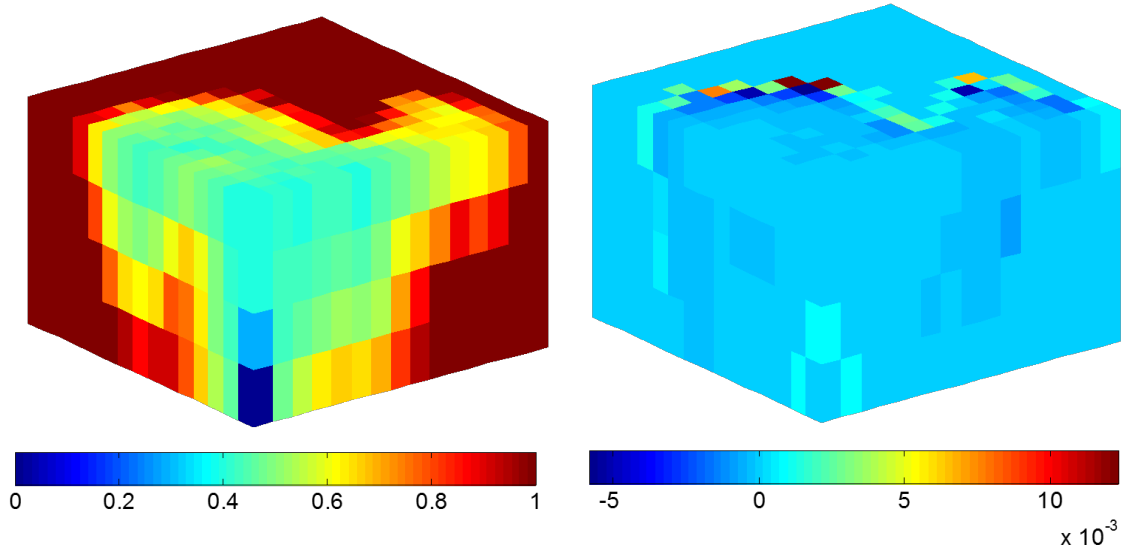

(a) Saturation profile, overall-compositions (b) Difference in saturation profiles

Figure 3.8: Aqueous saturation profile for the overall-composition variable formulation at 57 years, along with the difference between the two saturation profiles produced using overall-composition and natural variables.

Table 3.7: Numerical performance of the algorithms in producing the data in Fig. 3.9. Data given at 500 years.

Numerical scheme	Time steps	Newton iterations	Avg. linear solver iters. per Newton iter.	Avg. flash iters. per Newton iter. per block
Natural	582(16)	2334(311)	4.45	0.52
Overall-compositions	670(116)	1989(2320)	3.99	1.27
Hybrid	576(13)	2393(157)	4.73	0.56

differences in saturation profiles between the overall-composition and the natural-variable schemes. The profiles are very close, and the minor differences are within the tolerances. These differences are usually observed around the saturation front. A similar comparison at 500 years is presented in Fig. 3.9.

The numerical performance of the three schemes is assessed in Table 3.7. As expected, the phase equilibrium cost is higher for the overall-composition case compared to

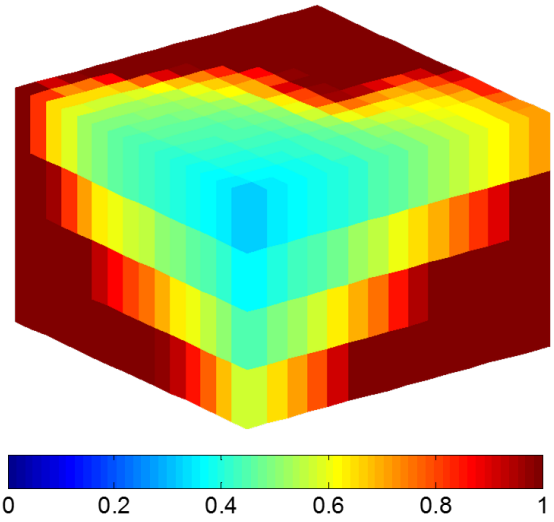

(a) Water saturation profile, Overall-compositions

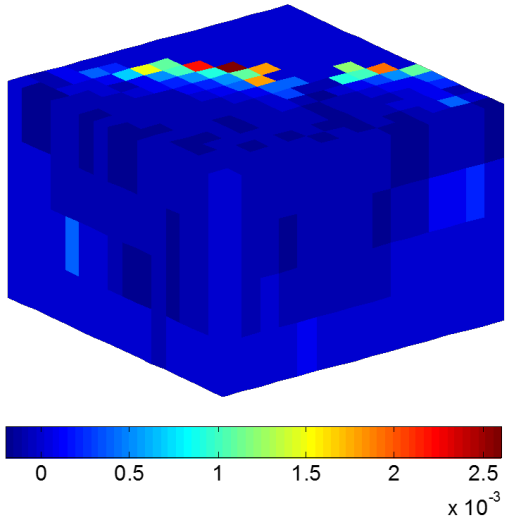

(b) $S_{w,\text{overall-compositions}} - S_{w,\text{natural}}$

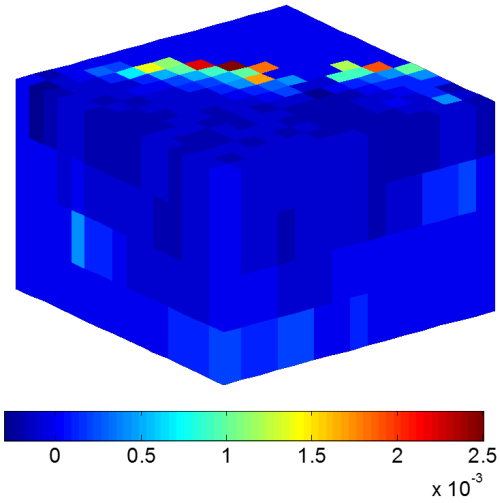

(c) $S_{w,\text{overall-compositions}} - S_{w,\text{hybrid}}$

Figure 3.9: Aqueous saturation profile for the overall-composition variable formulation at 500 years (top). The difference between the saturation profiles (bottom), where the profiles produced under natural-variable and hybrid formulations are compared against that obtained from the overall-composition variable formulation.

the other scenarios. Consistent with previous observations, this formulation again requires more time steps when crossing the phase boundary because it treats the problem more accurately by maintaining tight tolerances.

3.3 Concluding remarks

In this chapter we discussed a fully-coupled, fully-implicit simulation framework to handle kinetic, equilibrium, homogeneous and heterogeneous reactions within an overall-composition variable formulation. The treatment of primary and secondary variables and equations was discussed in detail. Similar to the natural-variable approach, transformations at the level of the Jacobian matrix convert the component mass balance equations into element balance equations. Though linear-level transformation, i.e., Schur complement, is not required in the purely compositional overall-composition formulation, we have proposed and employed such manipulations in our reactive-transport model to enhance efficiency. This transformation offers significant savings at the linear solver level due to the large number of equilibrium reactions that commonly govern geochemical systems.

A hybrid numerical formulation was proposed, which offers an alternative to deposition modeling in treating water phase disappearance and reappearance. It incorporates some of the advantages of the overall-composition variable formulation into an existing simulator, though it is based on the natural-variable formulation.

We analyzed the performance of the three numerical formulations for geological carbon storage problems. Results for a two-dimensional model demonstrated a close match among the reactive-transport models. We then used a one-dimensional model to investigate the impact of mass and time scale differences, and the nonlinearity due to chemical reactions, on the different numerical techniques for cases with water disappearance and reappearance in a geochemical system. We observed that the complications that arise when crossing the phase boundaries in geochemical simulations using a cubic equation of state are due in large part to the presence of aqueous species. Finally, an investigation was conducted for a three-dimensional system of 900 grid blocks, which demonstrated close agreement among the results of the three formulations.

When treating chemical reactions, natural and overall-composition variable formulations show the same advantages and drawbacks as under (non-reactive) compositional simulation. This is however not true in our special case of crossing thermodynamic

phase boundaries in the presence of trace amounts of material in only one of the phases (aqueous). The overall-composition variable formulation is capable of converging to the solution, though it may require many time step cuts. The natural-variable formulation attempts to resolve the local phase compositions and volume fractions at the global level, while undergoing variable switching, and may not achieve convergence under tight tolerances.

The high cost of phase equilibrium calculations in the overall-composition variable treatment represents an important drawback. However, solving the subset of grid blocks which experience water phase disappearance, in terms of overall-compositions, is advisable in the application under study. Alternatively, in a simulator based on the natural-variable formulation only, deposition modeling is also a viable option, and it requires the least modification to the underlying simulator. The hybrid method removes the necessity of specifying the arbitrary parameter in the deposition reaction rate, though it imposes additional variable switching requirements, thus demanding modification of the nonlinear solver.

Chapter 4

In-situ Carbon Storage in Ultramafic Rocks

Carbonate mineralization entails the dissolution of non-carbonate, primary minerals, including silicates, oxides and hydroxides, followed by the precipitation of secondary, carbonate minerals. Carbonate mineralization is thus a highly favorable storage mechanism that may reduce the risk of CO_2 leakage relative to other forms of trapping.

Ultramafic rocks were introduced in Chapter 1 as potential candidates for the sequestration of CO_2 in the form of minerals. Weathering in ultramafic rocks, where the carbonation takes place naturally, has been studied in order to understand the reaction pathways, limiting factors, and potential complexities governing mineral alterations [45, 37, 54, 88]. Results from these investigations will be applied to the assessments considered in this work.

In this chapter, carbonation of ultramafic rocks is investigated under both weathering and sequestration conditions. A list of the minerals involved in these processes, along with their chemical formula and type (primary or secondary), is provided in Table 4.1. As noted in Chapter 1, primary minerals are by definition the constituent minerals of the rock, which can dissolve when they are in contact with undersaturated water. Secondary minerals result from precipitation, which occurs when the water becomes supersaturated under the conditions of interest.

Table 4.1: Minerals relevant to CO_2 storage in ultramafic rocks.

Mineral	Chemical formula	Type
Olivine	$(Mg, Fe)_2SiO_4$	Primary
Forsterite	Mg_2SiO_4	Primary
Enstatite	$MgSiO_3$	Primary
Diopside	$MgCaSi_2O_6$	Primary
Fayalite	Fe_2SiO_4	Primary
Magnesite	$MgCO_3$	Secondary
Hydromagnesite	$Mg_5(CO_3)_4(OH)_2 - 4\,H_2O$	Secondary
Calcite	$CaCO_3$	Secondary
Dolomite	$CaMg(CO_3)_2$	Secondary
Chrysotile	$Mg_3Si_2O_5(OH)_4$	Secondary
Brucite	$Mg(OH)_2$	Secondary
Magnetite	Fe_3O_4	Secondary
Quartz	SiO_2	Secondary
Halite	NaCl	-

We first consider the reaction paths experienced in a natural weathering system in peridotites of Samail Ophiolite in Oman. Peridotites are ultramafic rocks that are rich in the mineral olivine, $(Mg, Fe)_2\,SiO_4$. Olivine has the two endmembers forsterite (Mg_2SiO_4) and fayalite (Fe_2SiO_4). We model this system using our implementation of reactive transport in Stanford's Automatic Differentiation-based General Purpose Research Simulator (AD-GPRS). This model is subsequently employed to simulate a CO_2 sequestration project in an idealized ultramafic reservoir. A series of sensitivity runs will be performed in order to quantify the impact of reservoir and operational parameters on CO_2 mineralization.

4.1 Impact of solution pH on CO_2 dissolution

In the reaction paths of interest in this application, the primary minerals provide a source of base. The details of this process are described in this section. The relatively fast mineral dissolution kinetics consume H^+ ions rapidly, impacting the aqueous concentrations of the carbon-bearing ions dramatically. The high pH values imposed by the primary minerals thus lead to a potentially major rise in the total concentration of aqueous CO_2. The total concentration of aqueous CO_2, also referred to in this work as dissolved inorganic carbon (DIC), includes dissolved carbon in all forms, e.g., H_2CO_3, $HCO_3{}^-$, and $CO_3{}^{2-}$.

The formation of carbon-bearing ions is governed by a series of reactions, as illustrated in the following. After the dissolution of carbon dioxide in water, the solution experiences a lowered pH via the following reactions [59]:

$$CO_2(aq) + H_2O \longrightarrow H_2CO_3, \tag{4.1}$$

$$H_2CO_3 \longrightarrow HCO_3{}^- + H^+, \tag{4.2}$$

$$HCO_3{}^- \longrightarrow CO_3{}^{2-} + H^+. \tag{4.3}$$

Naturally occurring silicates, e.g., forsterite, respond to the excess H^+ content by dissolving:

$$Mg_2SiO_4 + 4\,H^+ \longrightarrow 2\,Mg^{2+} + SiO_2 + 2\,H_2O. \tag{4.4}$$

The carbonate and bicarbonate ions precipitate in the form of carbonate minerals once divalent cations are available through the above dissolution reaction. The reaction is:

$$\mathrm{CO_3}^{2-} + \mathrm{Mg}^{2+} \longrightarrow \mathrm{MgCO_3}. \tag{4.5}$$

The conversion of the dissolved CO_2 triggers additional sequences of the reactions in Eqs. (4.1)-(4.5). The H^+ ion is consumed by silicate dissolution and produced by CO_2 dissolution. A host rock with high kinetic rates can therefore enhance CO_2 storage through dissolution and mineralization, by rapidly consuming H^+ ions and producing divalent ions.

To illustrate the impact of pH buffering on the ionic trapping of CO_2, consider the following set of equations governing the equilibrium reactions described by Eqs. (4.1)-(4.3):

$$\frac{[\mathrm{H_2CO_3}]}{[\mathrm{CO_2(aq)}][\mathrm{H_2O}]} = K_1, \tag{4.6}$$

$$\frac{[\mathrm{HCO_3}^-][\mathrm{H}^+]}{[\mathrm{H_2CO_3}]} = K_2, \tag{4.7}$$

$$\frac{[\mathrm{CO_3}^{2-}][\mathrm{H}^+]}{[\mathrm{HCO_3}^-]} = K_3, \tag{4.8}$$

where the values K_1, K_2, and K_3 are equilibrium constants. Since the concentration of H_2CO_3 is dictated through multiphase equilibrium, higher pH values lead to higher carbonate and bicarbonate ion concentrations, i.e., encourage ionic trapping.

An example of water-rock interactions enhancing carbon dissolution is shallow groundwater in the natural peridotite weathering systems introduced later in this chapter [73]. Through the phenomena described by Eqs. (4.1)-(4.5), the surface weathering of peridotites has acted as an effective capture mechanism, leading to highly elevated concentrations of DIC in the groundwater.

Note that, in addition to enhanced ionic trapping, the relatively fast kinetics associated with ultramafic rocks (compared to sandstones) may result in faster carbonate precipitation because silicate dissolution, e.g., Eq. (4.4), is usually thought to be the rate-limiting step in the carbonation process [88].

4.2 Natural weathering of ultramafic rocks

Peridotite hydration and carbonation are two phenomena observed in weathering outcrops. They are both thermodynamically favored, exothermic processes at conditions relevant to weathering and carbon sequestration. For example, consider forsterite, the Mg end-member of olivine ($(Mg, Fe)_2SiO_4$), as a main constituent mineral of peridotites. The hydration process involves the conversion of forsterite (Mg_2SiO_4) into chrysotile ($Mg_3Si_2O_5(OH)_4$) and brucite ($Mg(OH)_2$). Meanwhile, the carbonation process leads to the product of interest in carbon sequestration, magnesite ($MgCO_3$). These reactions may be expressed as follows:

$$\underset{\text{forsterite}}{2Mg_2SiO_4} + 3H_2O \rightarrow \underset{\text{chrysotile}}{Mg_3Si_2O_5(OH)_4} + \underset{\text{brucite}}{Mg(OH)_2}, \tag{4.9}$$

$$\underset{\text{forsterite}}{Mg_2SiO_4} + 2CO_2 \rightarrow \underset{\text{magnesite}}{2MgCO_3} + \underset{\text{quartz}}{SiO_2}. \tag{4.10}$$

Hydration occurs in contact with an aqueous phase. The carbonation process in Eq. (4.10), however, will only take place in the presence of CO_2. Note that the reactions in Eqs. (4.9) and (4.10) are expressed slightly differently in the reaction sets that follow. Moreover, while the hydrated silicates, e.g., chrysotile, may subsequently react with CO_2 to yield carbonates, the corresponding reaction kinetics are orders of magnitude slower than those for forsterite carbonation in Eq. (4.10) [39]. These other reaction paths are thus ignored in this work.

Peridotite weathering, which involves a series of low temperature reactions among surface water and peridotite, is believed to consist of three consecutive stages [8]. These stages are hypothesized in order to explain the aqueous as well as mineral compositions characteristic of typical outcrops. We investigate two reaction paths, which correspond to published data and analyses of the weathering phenomena in

Samail Ophiolite of Oman [88]. The three processes are briefly introduced, followed by a detailed description of the AD-GPRS model.

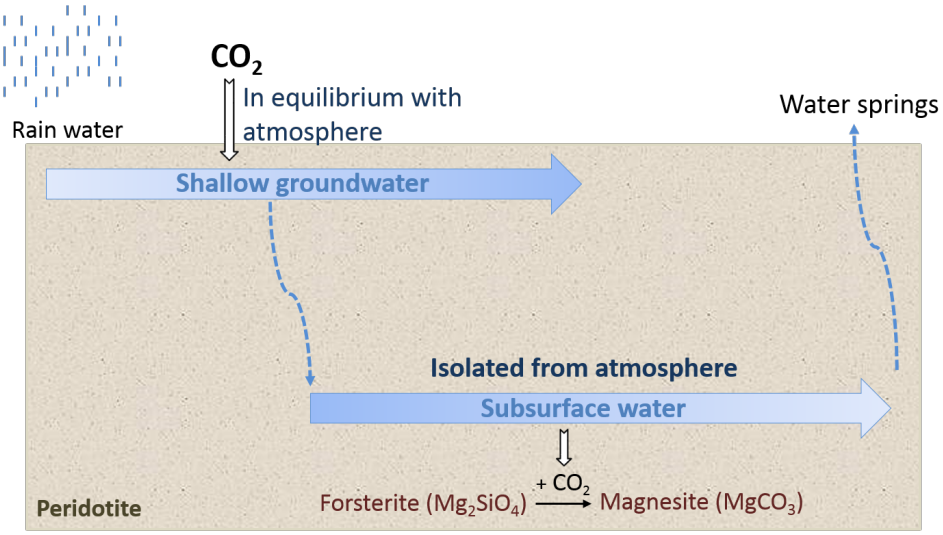

Figure 4.1: Simplified schematic of the weathering phenomena in a hypothetical peridotite rock. The shading of the arrows represents total dissolved carbon concentration (darker shades correspond to higher concentrations).

The first stage, represented by the upper blue arrow in Fig. 4.1, involves near-surface weathering, which occurs on the surface or at shallow depths. As rainwater reacts with peridotite in equilibrium with the atmosphere, elevated concentrations of dissolved Mg^{2+} and HCO_3^- develop. This yields Mg^{2+}–HCO_3^- rich water, referred to as Type I water, which is characteristic of shallow groundwater in peridotite rocks. The detailed reaction system governing this phenomenon is described in the next section.

The second stage occurs in the subsurface, where Type I water is exposed to peridotite in the absence of atmospheric contact. Magnesium carbonates, e.g., magnesite and dolomite, as well as serpentine (e.g., chrysotile) and clay minerals, precipitate out of the solution. Despite being a minor component in peridotite, the dissolved Ca^{2+} content rises due to dissolution of the pyroxene minerals (e.g., diopside), even in the presence of dolomite precipitation. This is due to the absence of Ca^{2+} in the precipitating serpentine and clay [54]. Rapid mineral dissolution rates produce a very high pH, while at the same time carbonate precipitation consumes the dissolved

carbon. This process yields high pH (around 12), low-carbon solutions known as Type II waters, observed as the $Ca^{2+}-OH^{-}$ water emerging from alkaline springs in peridotites. The detailed reaction system representing this stage is discussed in Section 4.2.2.

The third stage occurs when the alkaline spring waters, upon contact with the atmosphere, experience a lowering of pH to neutral levels, along with calcite and dolomite precipitation. This stage is not modeled in this work due to the lack of reported (quantitative) field measurements.

The first and second stages of this process will now be simulated and compared to a model developed by Paukert et al. [88] using a software package for geochemical modeling of aqueous systems, EQ3/6, v.8.0 [124]. Our goal here is to keep our work consistent with the published analysis, while accounting for the different software characteristics and taking advantage of the advanced features in AD-GPRS. The implementation in AD-GPRS has the ability to treat any combination of reactions among components in multiple phases. In order to minimize the simulation cost, in this work we aim at finding the smallest set of reactions/components that are representative of the phenomena of interest, i.e., reactions leading to CO_2 mineralization. This simplification will enable us to perform many simulations efficiently, as required for detailed engineering assessments or computational optimization. The geochemical analysis conducted using exhaustive reaction sets found in geochemistry databases is, however, a key first step in our procedure.

4.2.1 Numerical model, first stage

The first stage of the process occurs near-surface and in contact with the atmosphere. We model this system as a batch reactor using a single grid block. The reaction system consists of 13 fluid species, nine solid phases (minerals and halite), five equilibrium reactions, and nine kinetic reactions. This results in a reactive compositional model involving 22 species and eight elements. The aqueous phase is initialized to rainwater composition [88], and is held in equilibrium with a gas phase representing the atmosphere. The water composition and mineral concentrations are tracked over time. Atmospheric pressure and a temperature of 30°C are assumed.

The reference work, by contrast, employs a fluid-centered flow-through model [88]. In this model, 1 kg of water undergoes successive stages in which it is equilibrated with the atmosphere and consequently exposed to fresh porous medium. The quantities that are tracked are the cumulative masses of precipitated secondary minerals and the aqueous composition. The dissolution kinetics relate time to reaction progress in this model. In our batch reactor model, we capture this behavior by stepping through time, while providing an abundant amount of primary minerals. We allow only precipitation of secondary minerals, and prevent their dissolution throughout this work.

Based on field observations, the primary minerals consist of forsterite, enstatite, and diopside. Paukert et al. [88] also included the primary mineral fayalite (Fe_2SiO_4) and the secondary mineral magnetite (Fe_3O_4). However, the influence of these iron-bearing minerals and the corresponding ions on quantities of interest (carbonization products) was concluded insignificant based on simulation results under the conditions of interest. We thus eliminated these components to reduce the system of reactions. The aqueous system was also simplified by removing various complexes that had negligible concentration and no measurable impact on the results, e.g., ${H_2SiO_4}^{2-}$, ${HSiO_3}^{-}$ and $MgCl^{+}$. The final system of reactions used in this work to model the first weathering stage is given in Table 4.2.

For all reaction systems in this work, the aqueous reactions are modeled as equilibrium reactions, while mineral reactions are treated kinetically. The thermodynamic properties required for chemical reaction modeling are extracted form SUPCRT92 at all temperatures and pressures of interest. Moreover, in all cases in this work, equilibrium among fluid phases is modeled through a modified Peng-Robinson equation of state. This model fits the H_2O volume shift parameter as well as the H_2O-CO_2 binary interaction coefficients to published data [60, 26].

Salinity rises in the first weathering stage from that of rainwater to that of Type I water. It then continues to increase through the second stage, yielding the Type II water salinity. Halite dissolution is included in the simulation model to enable the formation of the elevated aqueous concentrations of Cl^{-} expected from field measurements. As in [88], the dissolution rate of halite is not calculated independently, and

is taken to be proportional to the forsterite dissolution rate. The calculated salinity matches field observations, namely measured Cl^- concentration values of 3.5 mmol/l in Type I water and 7.25 mmol/l in Type II water [88].

Table 4.2: Chemical reaction system used in the first weathering stage. All aqueous reactions are modeled as equilibrium reactions, while mineral reactions are treated kinetically.

Reaction #	Type	Reactions
1	Equilibrium	$MgCO_3 = Mg^{2+} + {CO_3}^{2-}$
2	Equilibrium	$MgHCO_3{}^+ = Mg^{2+} + HCO_3{}^-$
3	Equilibrium	$CO_2(aq) + H_2O = H^+ + HCO_3{}^-$
4	Equilibrium	$HCO_3{}^- = {CO_3}^{2-} + H^+$
5	Equilibrium	$H_2O = H^+ + OH^-$
6	Kinetic	$\text{Forsterite} + 4\,H^+ = 2\,Mg^{2+} + SiO_2(aq) + 2\,H_2O$
7	Kinetic	$\text{Enstatite} + 2\,H^+ = Mg^{2+} + SiO_2(aq) + H_2O$
8	Kinetic	$\text{Diopside} + 4\,H^+ = Ca^{2+} + Mg^{2+} + 2\,SiO_2(aq) + 2\,H_2O$
9	Kinetic	$\text{Hydromagnesite} + 10\,H^+ = 5\,Mg^{2+} + 4\,CO_2(aq) + 10\,H_2O$
10	Kinetic	$\text{Chrysotile} + 6\,H^+ = 3\,Mg^{2+} + 2\,SiO_2(aq) + 5\,H_2O$
11	Kinetic	$\text{Calcite} = Ca^{2+} + {CO_3}^{2-}$
12	Kinetic	$\text{Quartz} = SiO_2(aq)$
13	Kinetic	$\text{Brucite} + 2\,H^+ = Mg^{2+} + 2\,H_2O$
14	Kinetic	$\text{Halite} = Na^+ + Cl^-$

All rock-water interactions are modeled as kinetic reactions based on the following reaction rate law:

$$r_k = A k_r a_{H^+}^{n_{H^+}} \left(1 - \Omega\right), \tag{4.11}$$

where Ω is the mineral saturation index, A is the mineral surface area, k_r is the kinetic rate constant, and a_{H^+} is the activity of the H^+ ion. Here $n_{H^+} = 0$ unless otherwise specified. Note that all of these parameters were defined in Chapter 2.

Table 4.3: Primary mineral kinetic rate constants. These k_r values (mol/m^2/s) are reported at 25°C. The first two columns follow the data reported in [88]. Values in the last column, which are applied to the sequestration problem, were obtained from experimental data measured at temperatures closest to the temperature of interest (90°C). These values are extracted from [87] for forsterite (65°C), [84] for enstatite (100°C), and [58] for diopside (70°C). Note that the various systems correspond to different pH and temperature values.

	First weathering stage		Second weathering stage		Sequestration model	
Mineral	k_r	n_{H^+}	k_r	n_{H^+}	k_r	n_{H^+}
Forsterite	8.71×10^{-9}	0.28	2.40×10^{-11}	-	3.79×10^{-10}	-
Enstatite	1.10×10^{-9}	0.25	8.24×10^{-10}	0.24	3.51×10^{-11}	-
Diopside	3.16×10^{-10}	0.19	6.92×10^{-12}	-	2.53×10^{-11}	-

In [88] the secondary minerals were assumed to be in equilibrium with the aqueous phase. We instead use very fast kinetics for these minerals, essentially ensuring equilibrium. The kinetic rate constants used throughout this chapter for primary minerals are given in Table 4.3. A kinetic rate constant of 10^{-7} mol/m^2/s is used for all secondary minerals except for magnesite, dolomite, and quartz. The kinetic rate constants for magnesite and dolomite are 10^{-4} mol/m^2/s, while a value of 10^{-6} mol/m^2/s is used for quartz. These values correspond to the 'slowest' rates that give similar behavior to the equilibrium assumption in [88]. All values are reported at 25°C. Activation energy values of 16.1, 11.6, and 9.7 kcal/mol are used for forsterite, enstatite, and diopside respectively. Activation energy is set to zero for the secondary minerals, however, making their rates temperature independent. Moreover, no pH-dependence is assumed for the secondary minerals. In order to maintain consistency with the fluid-centered flow-through model employed in [88], the reactions corresponding to the minerals are irreversible. This means we have only the dissolution of the primary minerals and the precipitation of the secondary minerals.

The initial rock composition in our work, given in Table 4.4, is based on the mineral mass fractions obtained from Paukert et al. [88]. The fraction corresponding to minerals not included in the reaction system, e.g., fayalite, is considered non-reactive rock.

Moreover, we employ a specific mineral surface area of $A_s = 0.26$ cm^2/(g mineral) for all minerals. This value was calculated by Kelemen et al. [54] by scaling the results of experiments conducted on fine particles (~ 70 μm) to a fracture spacing of 0.7 m [88, 5]. Assuming reactive transport occurs in fractures only, the entire rock located between two adjacent fractures is effectively considered a single grain for the purpose of defining specific mineral surface area. Scaling based on either cubic or spherical particle shapes, the surface area per unit volume of 0.7 m grains is 10^{-4} times that of the 70 μm particles. Specific surface area is consequently converted to the (bulk) mineral surface area, required in Eq. (4.11), through the following relationship:

$$A_m = A_{s,m}\rho_{rock}\zeta_m, \tag{4.12}$$

where subscript m represents mineral m, ζ_m indicates mineral mass fraction in the rock, and ρ_{rock} is the rock density [110]. It is worth noting that there is likely to be significant uncertainty associated with mineral surface area due to the impact of the detailed fracture geometry (including the effects of secondary fractures if they are present), asperities along the fracture walls, etc. The small value of 8.55×10^{-4} m^2/m^3 is assigned to the initial (bulk) mineral surface area for all the secondary minerals, based on the assumption that these minerals are not present in the original rock. Note that all the assumptions and values mentioned thus far, summarized in Tables 4.4 and 4.5, are employed throughout this chapter unless otherwise specified.

Table 4.4: Summary of the primary mineral properties. The mineral surface areas are calculated based on Eq. (4.12). Details of the kinetic rate constants for these minerals are given in Table 4.3.

Mineral	Forsterite	Enstatite	Diopside	Fayalite	Halite
Mass fraction, ζ_m	0.696	0.165	0.034	0.104	0.001
Surface area, A_m (m^2/m^3)	59.5	14.1	2.91	8.89	-
Activation energy, E (kcal/mol)	16.1	11.6	9.7	16.1	-
1st weathering stage	$\surd$	$\surd$	$\surd$	$\times$	$\surd$
2nd weathering stage	$\surd$	$\surd$	$\surd$	$\times$	$\surd$

Table 4.5: Summary of the secondary mineral properties. All these minerals are assigned an initial surface area, A, of 8.55×10^{-4} m^2/m^3, and an activation energy of zero. The 1st and 2nd stages refer to the first and second weathering stages.

Mineral	Magnesite	Hydromgnesite	Dolomite	Chrysotile	Calcite	Quartz	Brucite
k_r (mol/m^2/s)	10^{-4}	10^{-7}	10^{-4}	10^{-7}	10^{-7}	10^{-6}	10^{-7}
1st stage	×	√	×	√	√	√	√
2nd stage	√	√	√	√	√	√	√

The main carbonate of interest in this system is magnesite, whose crystallization has been deemed to be 'sluggish' in the literature [44, 100]. Despite the fact that magnesite is thermodynamically stable and favored under conditions relevant to CO_2 sequestration, its precipitation is inhibited by the strong hydration shells that form around the small Mg^{2+} ions [92]. As a result, various hydrated magnesium carbonates form depending on the efficiency of the geochemical system in breaking the hydration shells surrounding Mg^{2+} ions. These hydrated forms are expected to convert to the stable magnesite form over time. Various modeling approaches may be used to account for the formation of magnesite and its hydrated forms. For example, based on field observations, magnesite and dolomite precipitation are suppressed in the first weathering stage, while hydromagnesite precipitates in small amounts. Note that calcite forms more easily than magnesite, and at a faster rate, since the calcium ion is much larger than the magnesium ion.

Following the previous analysis [88], the model is run until a steady state aqueous composition is achieved, which occurs at about 65 years in our setup. The evolution of the water compositions and cumulative precipitated minerals per kilogram of water are presented in Fig. 4.2. DIC represents dissolved inorganic carbon. Type I water, identified by its $Mg^{2+}-HCO_3^-$ composition, is observed once steady state is reached (at the right end of Fig. 4.2(a)). The model in [88] required 30 years to achieve steady state aqueous composition, as opposed to our model, which took about 65 years. This discrepancy is due to the difference in the treatment of the secondary minerals. These minerals are assumed to be in equilibrium with the water phase in

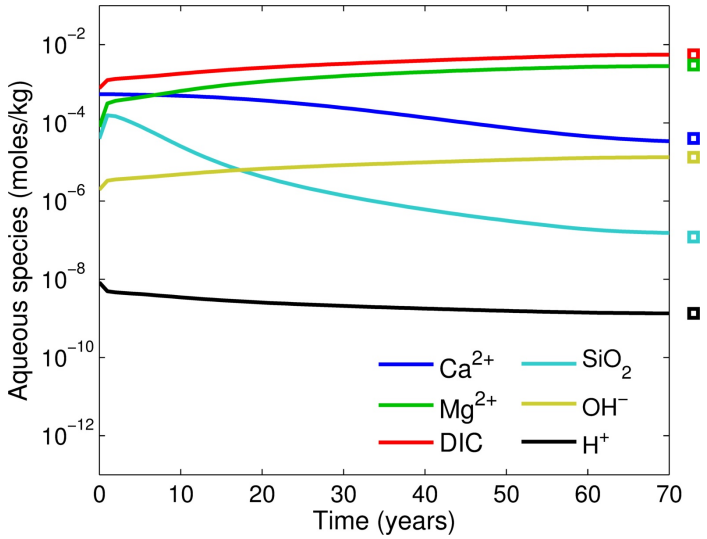

(a) Aqueous composition

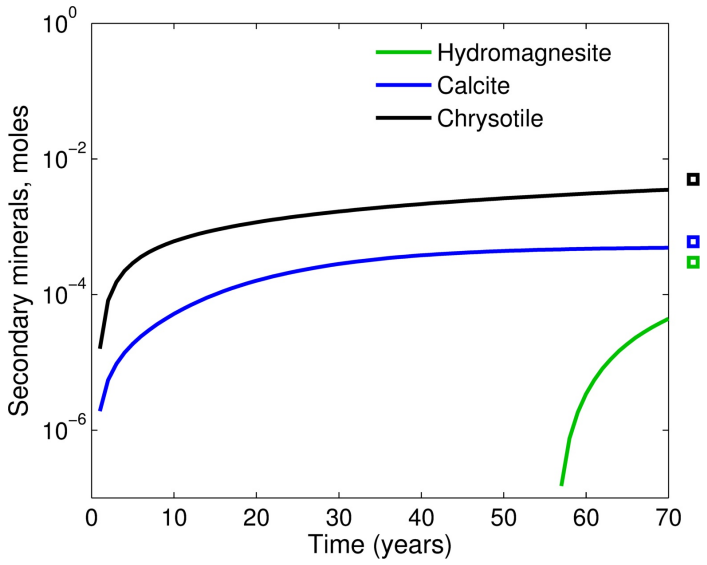

(b) Cumulative precipitated secondary minerals

Figure 4.2: Results of the first weathering system, presented for 1 kg of water. Aqueous composition is initialized to that of rainwater equilibrated with air and progresses to Type I water compositions. DIC denotes dissolved inorganic carbon. Chrysotile and calcite precipitate out of the solution, along with small amounts of hydromagnesite. The squares to the right of the plots denote the simulated steady state aqueous composition as well as the moles of (secondary) mineral precipitation profiles obtained at 30 years in the corresponding geochemistry simulation presented in [88].

[88], but are treated kinetically in our work. Steady state results from [88] are shown as squares on the right of the plots in Fig. 4.2. A close match is observed between the two steady state aqueous composition results.

The secondary mineral precipitation profiles, shown in Fig. 4.2(b), are again in reasonable agreement with the simulation results in [88]. In making this comparison, the significant difference in the treatment of secondary minerals (equilibrium versus kinetic) should be taken into account. Importantly, our computed profiles are consistent with field observations; i.e., they mainly indicate chrysotile and calcite precipitation. Finally, note that our simulated reaction path will be examined against measured field data in the next section.

As the water flows in contact with the peridotite rock, an increase in the pH is accompanied by a rise in the overall carbon dissolution, primarily due to ion formation. In fact, based on the steady state compositions shown in Fig. 4.3, Type I water is seen to contain dissolved carbon primarily in the form of HCO_3^-. The rise in pH due to the high kinetic rates of the primary minerals encourages the formation of bicarbonate ion through the reactions in Eqs. (4.1)-(4.3). This stage of the weathering process, which relies upon the high kinetic rates of the primary minerals, thus acts as an effective carbon capture mechanism.

4.2.2 Numerical model, second stage

The second system is concerned with the interaction of Type I water with subsurface peridotite, in the absence of atmospheric contact. This stage is also simulated using a single grid block (batch reactor) containing a single fluid phase (liquid) and the minerals. The reaction system includes the same 13 fluid species as in the first stage, 11 solid phases (minerals and halite), five equilibrium reactions, and 11 kinetic reactions. The reactive compositional simulation model thus consists of 24 components and eight elements. The primary minerals are the same as before, i.e., the primary peridotite content is assumed to not change with depth. Secondary minerals precipitating, however, now consist of magnesite, hydromagnesite, dolomite, calcite, quartz, chrysotile, and brucite, as seen in Table 4.6. The aqueous compositions are initialized to that of Type I water, and progress to the Type II compositions over time.

Table 4.6: Chemical reaction system used in the second weathering stage.

Reaction #	Type	Reactions
1	Equilibrium	$MgCO_3 = Mg^{2+} + {CO_3}^{2-}$
2	Equilibrium	$MgHCO_3^+ = Mg^{2+} + HCO_3^-$
3	Equilibrium	$CO_2(aq) + H_2O = H^+ + HCO_3^-$
4	Equilibrium	$HCO_3^- = {CO_3}^{2-} + H^+$
5	Equilibrium	$H_2O = H^+ + OH^-$
6	Kinetic	$\text{Forsterite} + 4\,H^+ = 2\,Mg^{2+} + SiO_2(aq) + 2\,H_2O$
7	Kinetic	$\text{Enstatite} + 2\,H^+ = Mg^{2+} + SiO_2(aq) + H_2O$
8	Kinetic	$\text{Diopside} + 4\,H^+ = Ca^{2+} + Mg^{2+} + 2\,SiO_2(aq) + 2\,H_2O$
9	Kinetic	$\text{Magnesite} = Mg^{2+} + {CO_3}^{2-}$
10	Kinetic	$\text{Hydromagnesite} + 10\,H^+ = 5\,Mg^{2+} + 4\,CO_2(aq) + 10\,H_2O$
11	Kinetic	$\text{Dolomite} = Ca^{2+} + Mg^{2+} + 2\,{CO_3}^{2-}$
12	Kinetic	$\text{Chrysotile} + 6\,H^+ = 3\,Mg^{2+} + 2\,SiO_2(aq) + 5\,H_2O$
13	Kinetic	$\text{Calcite} = Ca^{2+} + {CO_3}^{2-}$
14	Kinetic	$\text{Quartz} = SiO_2(aq)$
15	Kinetic	$\text{Brucite} + 2\,H^+ = Mg^{2+} + 2\,H_2O$
16	Kinetic	$\text{Halite} = Na^+ + Cl^-$

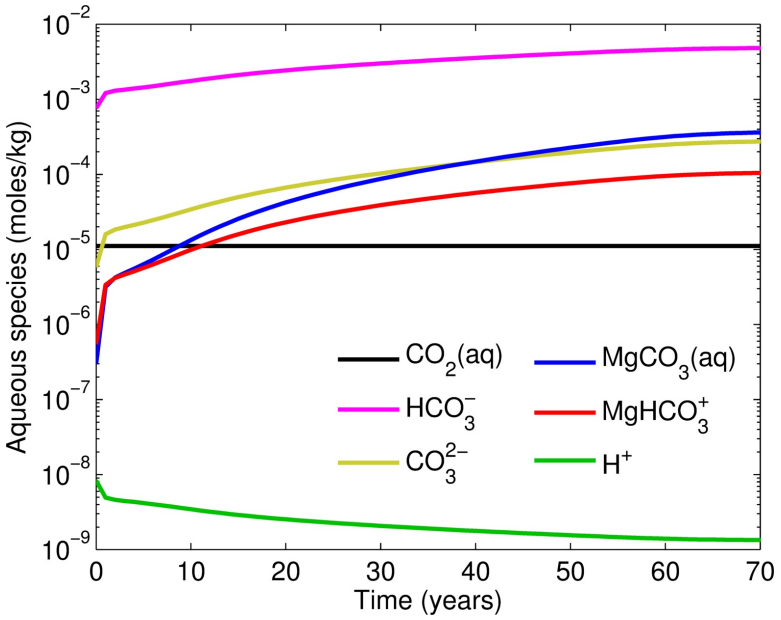

Figure 4.3: Distribution of carbon-bearing components in the water phase (first weathering stage).

Unlike in the first weathering step, and consistent with the reference geochemistry analysis, a steady state is not achieved in the second stage. This configuration is, however, modeled for long enough to reach the maximum pH measured in the field for Type II water samples (about 12). The resulting aqueous compositions and cumulative mineral precipitation profiles are shown in Fig. 4.4. We suppressed magnesite and dolomite precipitation in the first weathering step, but these effects are included in this stage, based on field observations. As a consequence, Type I water is supersaturated with respect to these minerals, resulting in their rapid precipitation out of the solution. This process consumes a major portion of the Mg^{2+} ion, as well as the dissolved carbon (DIC), and results in a high pH. Since the system is not in contact with the atmosphere, it is not replenished in CO_2. The precipitation of carbonates is thus limited by the (dissolved) CO_2 content in Type I water.

Continuous dissolution of the primary minerals provides the solution with Mg^{2+}, Ca^{2+}, and SiO_2(aq) ions, and leads to a rise in pH. This causes the precipitation of chrysotile, brucite, and calcite, as observed in Fig. 4.4(b). This stage thus entails carbonation, as well as hydration of the host rock. The overall weathering process

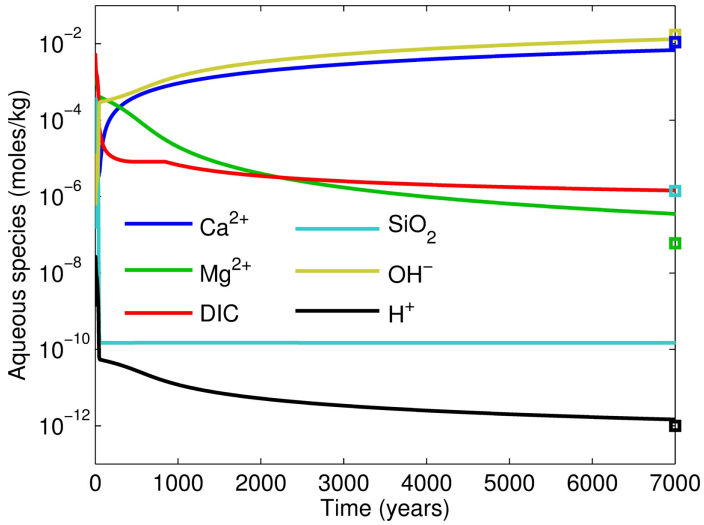

(a) Aqueous composition

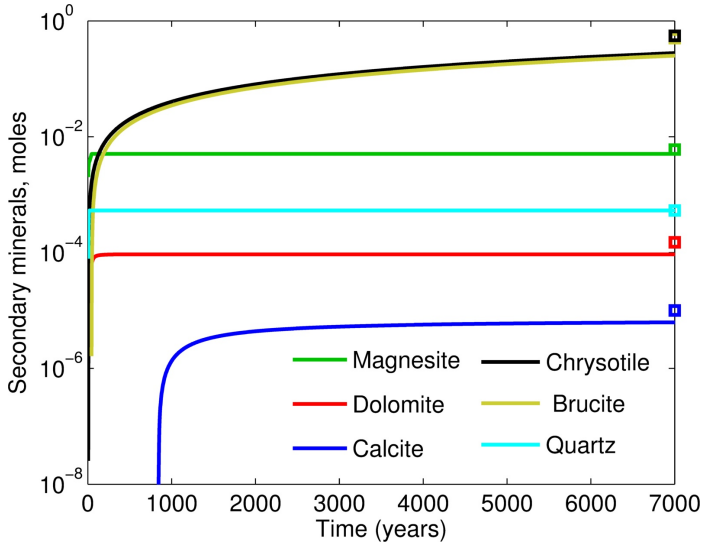

(b) Cumulative precipitated secondary minerals

Figure 4.4: Results of the second weathering system, presented for 1 kg of water. Aqueous composition is initialized to that of Type I water and progresses to Type II water composition. Initial precipitation of magnesite and dolomite consumes the dissolved CO_2. In the absence of any dissolved carbon, an alternative reaction path takes place and chrysotile and brucite precipitate out of the solution, along with small amounts of calcite. The squares represent the analogous results obtained in [88]. The amount of DIC at 7000 years reported in [88] is nearly zero (due to the equilibrium treatment of secondary minerals) and is thus not shown on the plot.

involves a natural, highly effective carbon capture mechanism during the first stage, followed by a sequestration step in the second stage [53]. As seen in Fig. 4.2(a), shallow groundwater captures atmospheric CO_2 in the form of ions as it reacts with the host rock. This stream of water loses contact with the atmosphere as it moves deeper in the formation, and subsequently undergoes the reaction path observed in Fig. 4.4(a). The dissolved carbon originating from the atmosphere thus precipitates in the form of magnesite and dolomite in the second stage, as seen in Fig. 4.4(b).

The data obtained in [88] at 7000 years are shown as squares on the plots in Fig. 4.4 and may be compared against our results. A smaller (nearly zero) DIC value as well as a higher SiO_2 content were reported at 7000 years in [88]. These discrepancies are due to the equilibrium treatment of the secondary minerals, which yields a slightly different equilibrium state in the aqueous phase composition. Key aqueous content values are in close agreement, while the secondary mineral masses are slightly less in our model.

In order to examine the validity of the simulated reaction paths, results of both stages are compared against field data in Fig. 4.5. Specifically, the aqueous DIC, Mg^{2+} and Ca^{2+} profiles are tracked from rainwater to the alkaline spring water measurements. The field data, shown as points on Fig. 4.5, were obtained from [88]. The various points correspond to measurements made in the Samail Ophiolite of Oman at three wells and 10 alkaline spring sites in peridotite in January 2009 and 2010. The samples were taken from alkaline springs at their discharge location in peridotite and along their surface flow path, from irrigation channels and wadis, and at the wells set in peridotite [88]. The measurements shown in Fig. 4.5 consist of data of three kinds. First, a single (averaged) rainwater composition defines the initial state of aqueous composition. Next, samples from fresh surface water and shallow groundwater constitute Type I water observations. Finally, measurements from alkaline spring waters found in the peridotite rocks are assumed to represent Type II water composition at depth. The arrows define the direction in which the system proceeds.

The process of the rainwater reaching equilibrium with the atmosphere is evident as the red horizontal lines (near the arrows) on all the plots in Fig. 4.5. Here, the pH rises while DIC and dissolved Mg^{2+} and Ca^{2+} values stay nearly unchanged. The remaining

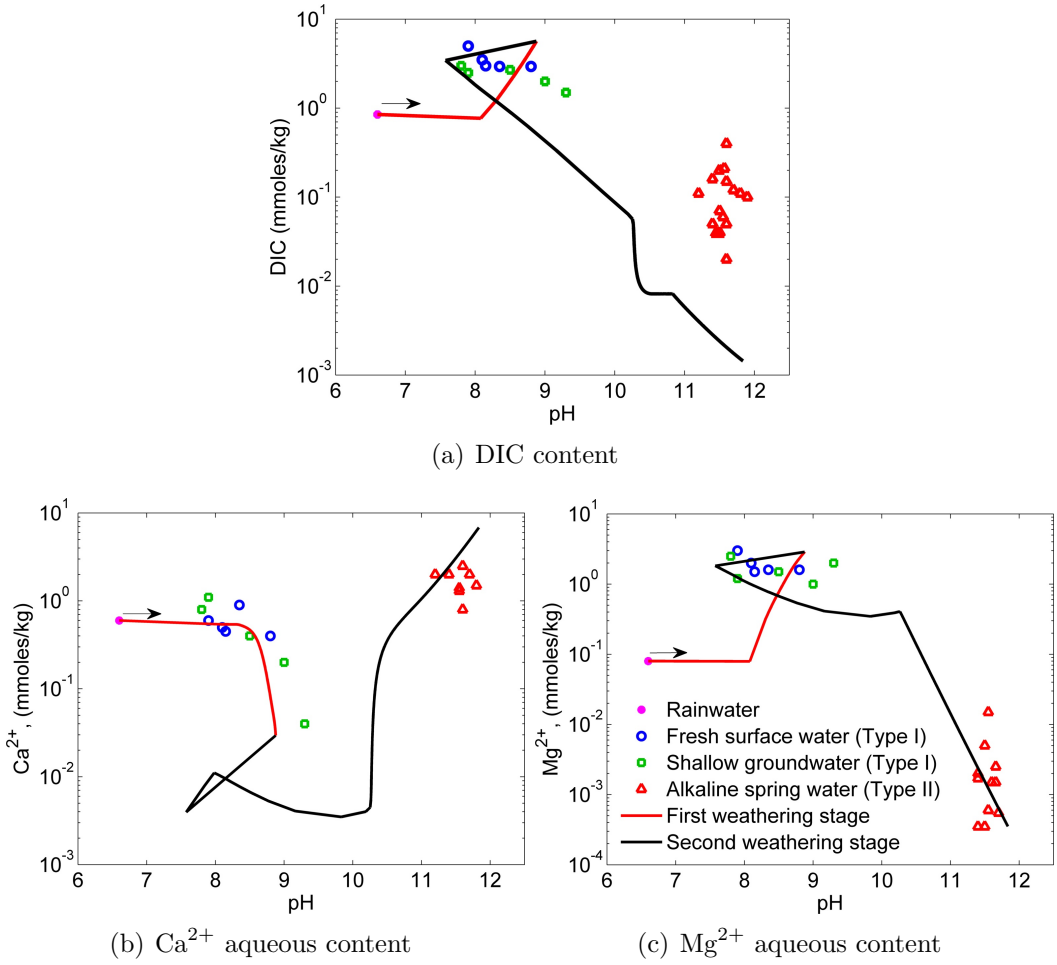

(a) DIC content

(b) Ca^{2+} aqueous content

(c) Mg^{2+} aqueous content

Figure 4.5: Comparison of simulated reaction paths for the two weathering systems against field data. Points signify data measured in the field, and the lines represent simulation results. The arrows demonstrate the direction of the composition change experienced through time. The aqueous composition, initially that of rainwater, progresses through the first and second weathering stages with time, arriving at Type II composition at the end of the solid black line.

portions of the red curves signify the variations experienced during the first stage of weathering, and correspond to the results in Fig. 4.2(a). The black lines capture the changes in aqueous composition during the second weathering stage, consistent with Fig. 4.4(a). As seen in Fig. 4.5(a), during the second stage the simulated DIC content decreases more steeply than the measured data. Nonetheless, our results are closer to these field observations than the simulated DIC content in Paukert et al. [88],

which declines to nearly zero values. While the authors in [88] discuss a few potential causes for the discrepancy between their simulation results and field data, the most likely source of this deviation in our results is that the samples of Type II water were collected at alkaline springs (at the surface) instead of at higher depths in the formation. The DIC content rises as water reaches the surface due to atmospheric contact. This may explain the elevated DIC values in the field samples relative to the simulation results in Fig. 4.5(a).

Both the Mg^{2+} and Ca^{2+} profiles are in reasonable agreement with the data. Moreover, the concentrations of both ions stay within the range of the field data at all stages. The maximum concentration for the Mg^{2+} ion in the shallow groundwater occurs at pH of around 9. The calcium ion experiences a drop in concentration in the first weathering stage and then an increase in the second stage due to the dissolution of diopside. A higher value for Ca^{2+} content is calculated in our model compared to the alkaline spring water data, as seen in Fig. 4.5(b). This behavior is also observed in [88], and may once again indicate that the alkaline spring water samples do not adequately represent the Type II water at depth in the formation. In fact, when rising to the surface, Type II water is likely to lose some of its calcium ion content through the precipitation of calcium carbonates at shallow depths [88], so the discrepancy is in the direction we would expect. Two of the shallow groundwater field samples experience pH values higher than expected for Type I water and thus deviate from the simulated reaction paths shown in Fig. 4.5. Similar deviations are also evident in the simulation results presented in [88].

4.3 Geological carbon sequestration modeling

The general agreement with measurements observed in weathering analogs provides a degree of validation of our modeling capability. It has been proposed that the natural weathering rates considered above can be enhanced by a factor of a million by moving the carbonation depth from about 15 m to 3 km [53]. Injecting CO_2 in deeper formations takes advantage of enhanced kinetics at the elevated temperatures. Moreover, the higher pressures increase CO_2 solubility in brine, which further enhances the kinetics. Also, a primary limiting factor in the natural system is the small supply

of CO_2 at carbonation depths. In a well-engineered process, large volumes of CO_2 will be continuously injected [53].

All reaction properties are consistent with those given previously. Specifically, dissolution kinetics parameters are extracted from the literature as reported in Table 4.3. The precipitation reaction rates are the same as in the weathering systems; i.e., they are kept high enough that silicate dissolution is once again the rate-limiting step. This is still an acceptable treatment since carbonates display faster kinetics compared to silicates [85]. In general, the silicate dissolution can be enhanced as shown in many experimental studies, but currently most of these techniques are cost-prohibitive at the field scale. For example, the dissolution of forsterite, serpentine, and anorthite can be enhanced by increasing interface area, raising the temperature, or through the addition of acids [82, 16]. Later in this chapter, we will briefly examine the influence of a field-scale increase in temperature.

4.3.1 Fractured medium modeling

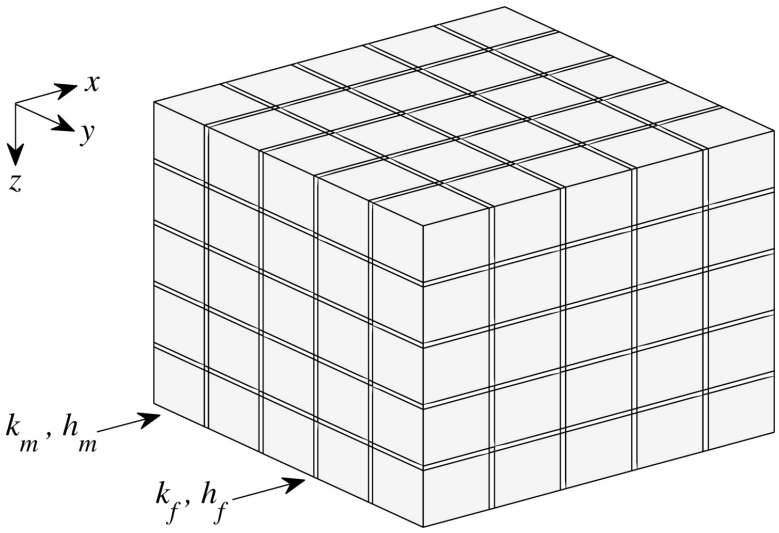

Figure 4.6: Three-dimensional view of fractures and matrix.

Peridotites are characterized by low permeability and porosity. Hydraulic fracturing could potentially be used to enhance these properties. In this work we assume that, if necessary, hydraulic fracturing or some other permeability-stimulation process has

already taken place. We do not attempt to model the fracturing process, though we account for it by considering enhanced reservoir properties. Moreover, fracture-matrix flow is not modeled; rather an overall effective permeability value is used, as we now describe.

In a fractured medium, flow takes place in fractures as well as in the matrix. In fractured ultramafic rocks, due to the low permeability of the matrix, the majority of the flow is expected to occur in fractures. It follows that the effective permeability is scale-dependent and can be estimated based on fracture density, which varies with depth in ultramafic rocks. In crystalline rocks at shallow depths, effective permeability values of 100 mD to 100 D have been observed at the large scale for 1% fracture porosity [125]. In deeper formations, values of 10 μD to 10 mD have been reported at smaller scales [72, 73]. For example, the permeability of the fissured weathering horizon in Oman peridotites has been estimated as 10 mD in a groundwater flow study [23].

For simplicity, we assume that hydraulic fracturing generates a uniform and isotropic fracture distribution throughout the reservoir, as shown in Fig. 4.6. This is clearly an approximation as a higher fracture density is expected in the vicinity of the well. The effective (upscaled) permeability for flow along (parallel to) the layers of a layered system, k_p, is given by:

$$k_p = \frac{\Sigma_i h_i k_i}{\Sigma_i h_i}, \tag{4.13}$$

where h_i and k_i indicate the thickness and permeability of region i (see Fig. 4.7).

Due to the extremely low permeability matrix in peridotites, the flow in all directions is dominated by the fractures along that direction. In the case of a homogeneous fracture distribution, as shown in Fig. 4.6, this yields the following approximation for effective permeability:

$$k_{eff} = 2 \times \frac{h_m k_m + h_f k_f}{h_m + h_f} \approx 2\frac{h_f}{h_m} k_f, \tag{4.14}$$

where k_{eff} stands for effective permeability in the x, y or z directions, k_f and h_f

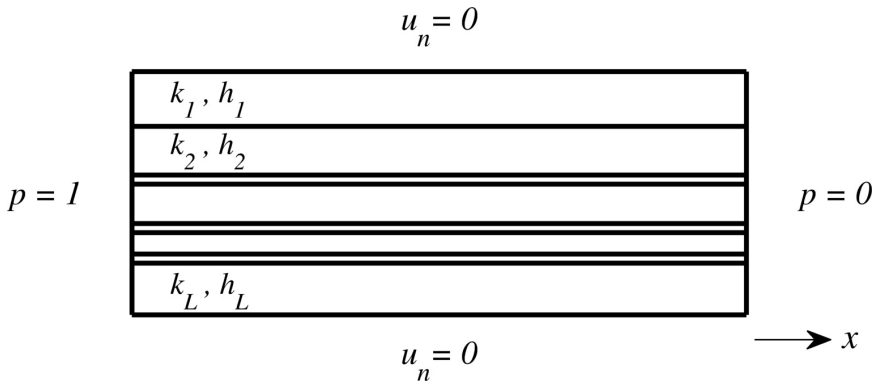

Figure 4.7: Two-dimensional view of a layered system.

are the fracture permeability and aperture, and k_m and h_m are the permeability and width of the matrix in between two fractures (See Fig. 4.6). This expression is based on the assumption that $h_f \ll h_m$ and $k_f \gg k_m$. The factor of 2 arises because, for a given flow direction, flow is enhanced by two sets of fractures.

For smooth fractures of constant aperture, k_f is related to aperture via $k_f = h_f^2/12$. This gives

$$k_{eff} = \frac{h_f^3}{6h_m}. \tag{4.15}$$

Following the discussion on mineral surface area in Section 4.2.1, a fracture spacing of 0.7 m is assumed, along with a very low matrix permeability ($k_m \ll 10$ mD). A fracture aperture of 0.035 mm then yields an effective permeability value of 10 mD for the hydraulically fractured ultramafic rock. This value is used in most of the computations in this chapter.

4.3.2 Three-dimensional simulation model

In this section, we assess an idealized geological carbon sequestration project in ultramafic rocks, namely peridotites in the Samail Ophiolite of Oman [53]. Some rock properties are based upon relevant data found in the literature. The reservoir dimensions are however selected in order to minimize the boundary effects. Despite the

large plume size (due to the very small pore volume of the formation), the boundaries can be avoided because the ultramafic massifs generally extend laterally over a large area. For example, the Samail Ophiolite of Oman is estimated to be more than 350 km long and about 40 km wide. This massif is on average 5 km thick, and contains approximately 30% peridotite by volume [88, 53]. In the simulations below, we assume a 400 m thick reservoir.

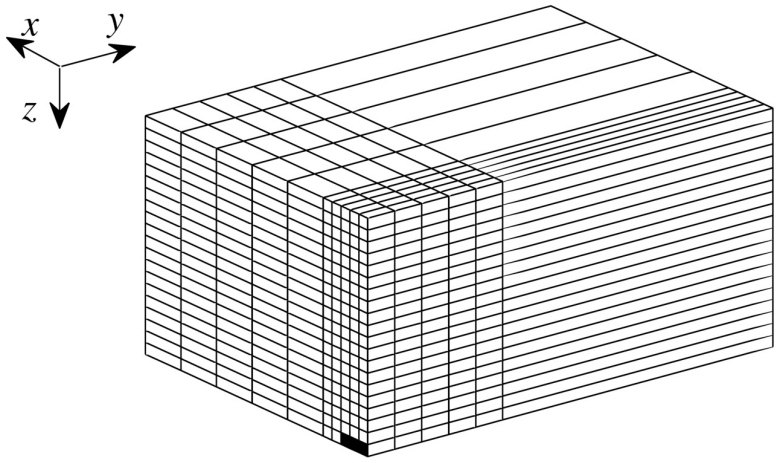

Figure 4.8: Schematic of the simulation model, showing one quarter of the reservoir. The blocks containing the horizontal well are shown in black.

In our model, a horizontal well of length 1.5 km (about 4900 ft) injects CO_2 at 1 MT/year in the center of a 12.5 km $\times$ 35 km $\times$ 400 m peridotite reservoir for 40 years. This corresponds to a total injection of 4% of the pore volume at reservoir conditions. The simulation model extends in the direction perpendicular to the horizontal well for 35 km on each side in order to provide pressure support. The injected CO_2 does not reach the large boundary blocks. These blocks have porosity of 20% and permeability of 1 D.

The schematic in Fig. 4.8 depicts one quarter of the reservoir. This model is simulated using $10 \times 6 \times 20$ grid blocks. The blocks are uniform in the central portion of the model in the y and z directions. In the x direction, along which the well extends, we use five blocks of 250 m length, followed by five blocks of size 1 km. The blocks containing the horizontal well are shown in black in Fig. 4.8. In all results presented

in this chapter, only the central (1/4) reservoir is shown, and the last block in the y direction is eliminated.

We again employ the reaction set in Table 4.6 except for interactions with hydromagnesite and halite. Similar to the second weathering system, hydromagnesite will not form because magnesite is thermodynamically favored at the conditions of interest. Halite dissolution is unimportant in the second, subsurface, weathering system studied above. In the absence of further information at greater depths, halite dissolution and precipitation are eliminated to avoid generating overly saline aqueous profiles. The aquifer is however initialized to the Type I water composition, including the elevated Na^+ and Cl^- content, namely a Cl^- concentration of 3.5 mmol/l (the average value observed in shallow groundwater of interest). Type I water is utilized under the assumption that local shallow groundwater would be available and employed for fracturing. Sensitivity studies demonstrated, however, that varying the initial aquifer water composition over a reasonable range had very little impact on simulation results.

The reservoir is assumed to be at 2 km depth, and thus at 200 bar and 90 °C, based on the geothermal gradients in Oman [88]. Effective permeability of 10 md, and 1% porosity, are prescribed. A pure stream of supercritical CO_2 is injected at the bottom of the reservoir. This phase flows upward due to gravity, and the CO_2 also transfers to the water phase due to dissolution, which leads to the formation of ions, as seen in Table 4.6. Through subsequent kinetic reactions, carbon is fixed in the form of minerals.

As confirmed by our simulation results, under this reaction system, CO_2 mineralization mainly occurs in the form of magnesite precipitation, and the primary source of divalent Mg^{2+} cations is forsterite. Magnesite precipitation consumes the dissolved DIC content of the aqueous phase. In the presence of a free supercritical CO_2 phase, the continuous dissolution of CO_2 in water supports DIC concentrations and maintains high carbonate precipitation rates. As a result, the profile of magnesite precipitation, shown in Fig. 4.9 at two different times, traces the location of CO_2.

The fate of the injected CO_2 is shown in Fig. 4.10. This ultramafic reservoir allows for more than 99% CO_2 mineralization in less than 250 years, which is a drastic

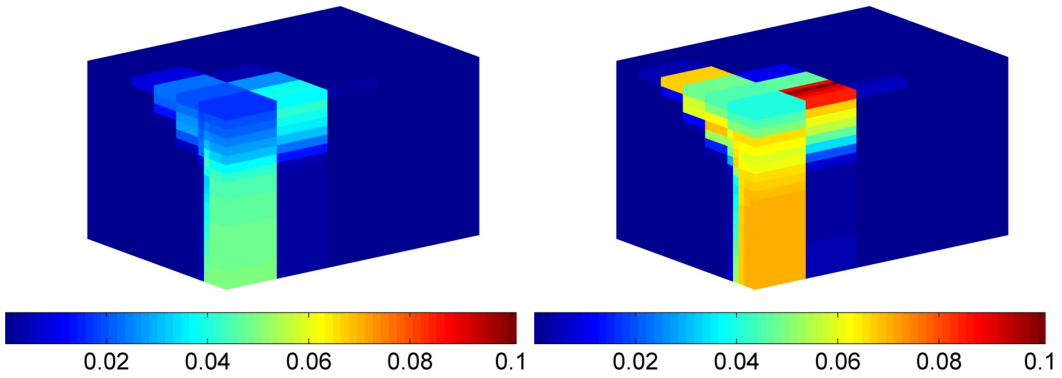

(a) 40 years (b) 100 years

Figure 4.9: Magnesite precipitation profile at two different times. Magnesite concentration is shown in units of kmol/(m^3 bulk volume). CO_2 injection stops at 40 years.

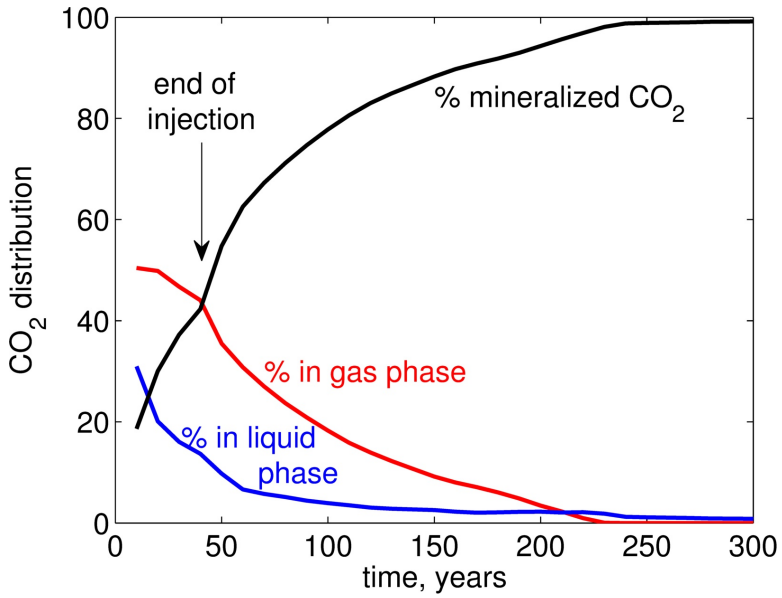

Figure 4.10: Fate of the injected CO_2 over the course of the simulation.

improvement from the 10% mineralization obtained for the sandstone case study in Fig. 2.8. Moreover, the remaining CO_2 (less than 1%) is captured in the form of ions, which is also a safe form of storage. Unlike in sandstones, the CO_2 does not remain in the gas phase, thus reducing the risk of leakage.

The rapid kinetics characteristic of ultramafic rocks have implications on the mineralization pattern. Most of the CO_2 is initially present in the form of gas, where it dissolves into water and finally converts to solids. Three distinct mineralization regimes, evident in Fig. 4.10, may be explained as follows. Initially, a rapid rate of mineralization is observed as the injected stream rises and the plume forms. This elevated reservoir-scale mineralization rate observed at about 45 years in Fig. 4.10 is due to reactions taking place in many parts of the model. Note that the change of slope at 40 years is due to the injection coming to an end, at which point the total injected CO_2 remains constant.

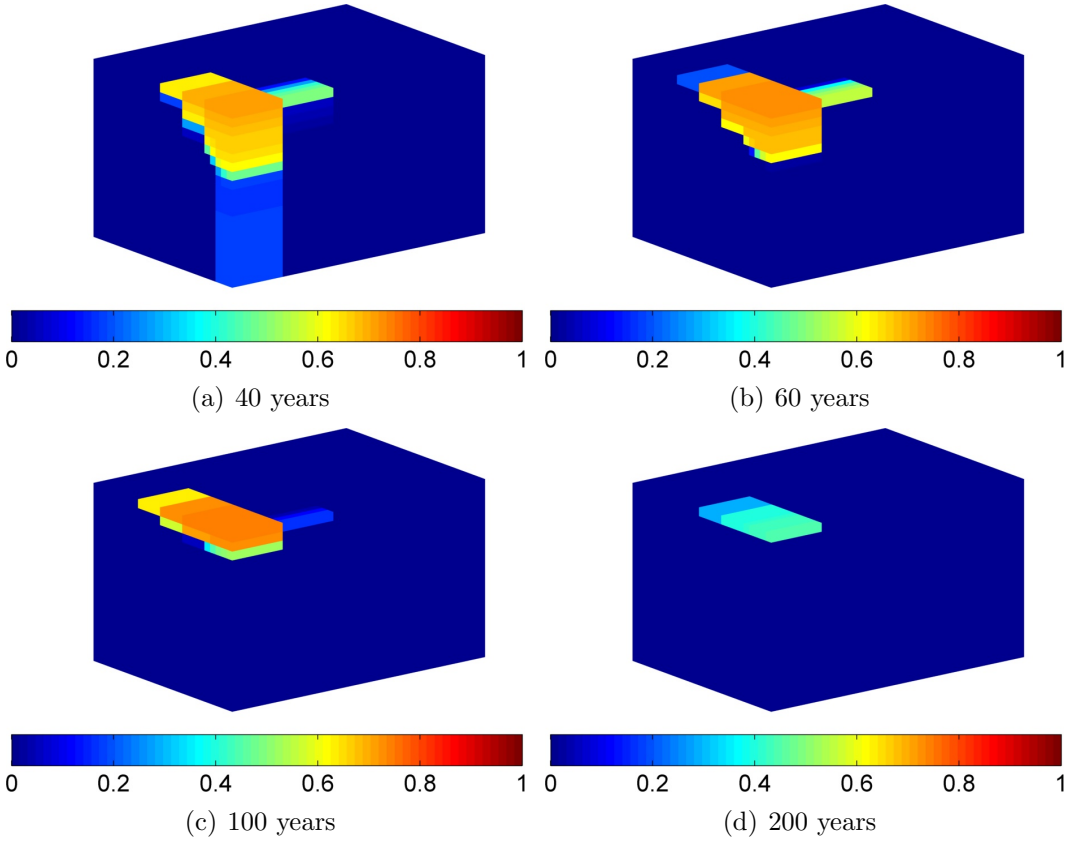

(a) 40 years (b) 60 years

(c) 100 years (d) 200 years

Figure 4.11: Gas saturation profiles at various times.

The second regime, starting at around 60 years, corresponds to mineralization occurring at the top of the reservoir, where the plume has formed. The mineralization rate

is smaller compared to the previous regime, since fewer blocks participate in the reactions. These blocks have nonzero gas saturation, which provides a continuous supply of aqueous carbon. The change in the number of such blocks is evident in Fig. 4.11. The nearly constant water carbon content after 100 years in Fig. 4.10 indicates that the transfer of carbon from the aqueous phase to the solids is compensated by CO_2 dissolution from the gas phase. Finally, the mineralization ceases as the gas phase disappears throughout the model, yielding the final, static mode.

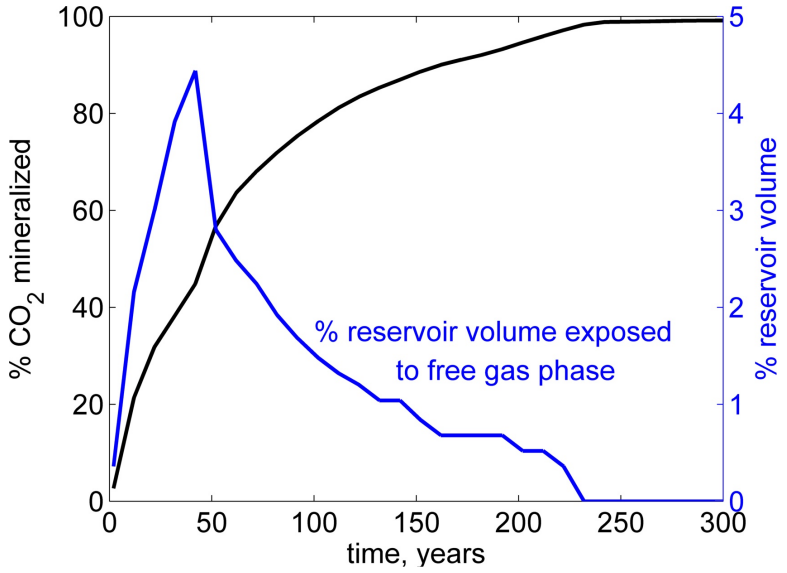

Figure 4.12: Mineralized CO_2 along with the volume of the reservoir containing free gas phase.

Our observations on the progress of mineralization have implications on the efficient design of storage operations. Clearly, distributing the gas phase over a large volume of the reservoir is a key factor in ensuring rapid mineralization. Having many regions where CO_2 is converted into a solid phase is highly beneficial. This is illustrated in Fig. 4.12, which highlights the close relationship between free gas distribution and mineralization rate. Essentially, the larger the reservoir volume participating in the reactions, the higher the mineralization rate.

Modeling porosity and permeability variations is of major importance in ultramafic

formations due to solid volume change during reactions. The porosity and permeability profiles, computed using the procedure described in Section B.1, are shown in Fig. 4.13 at 100 years and 300 years. Evidently, due to the mineralization occurring near the well region, reservoir injectivity is impacted negatively. The Carman-Kozeny equation employed in this work could be replaced by models that are more appropriate for describing permeability evolution in a fractured medium. For example, statistical approaches may be used to update matrix and fracture permeability values independently [115, 116].

The inclusion of variable surface area in the kinetics of mineral dissolution and precipitation [110] did not make a notable difference in this simulation model. Based on the composition of the rock [88], the primary minerals are present in abundance and have very large surface areas. These are altered very little during the 300 years of simulation.

4.3.3 Simplifying the reaction system

After analyzing the masses of various minerals dissolving and precipitating, we concluded that the key reaction paths can be represented using a simplified set of reactions consisting of a single primary mineral (forsterite) and four secondary minerals, as shown in Table 4.7. The original problem involves 22 species, 14 reactions, and eight elements, while the reduced model involves 17 species, ten reactions, and seven elements. The reduced model runs about 10 times faster than the base case. This is because (1) the smaller set of components leads to fewer unknowns, and (2) the reduced set of reactions removes some stiffness from the numerical system, resulting in larger time steps.

The mineralization results are compared against the base case in Fig. 4.14. The small error in percent CO_2 mineralized is acceptable given other approximations and uncertainties associated with field-scale models. The reduced reaction set is thus used in all subsequent simulations.

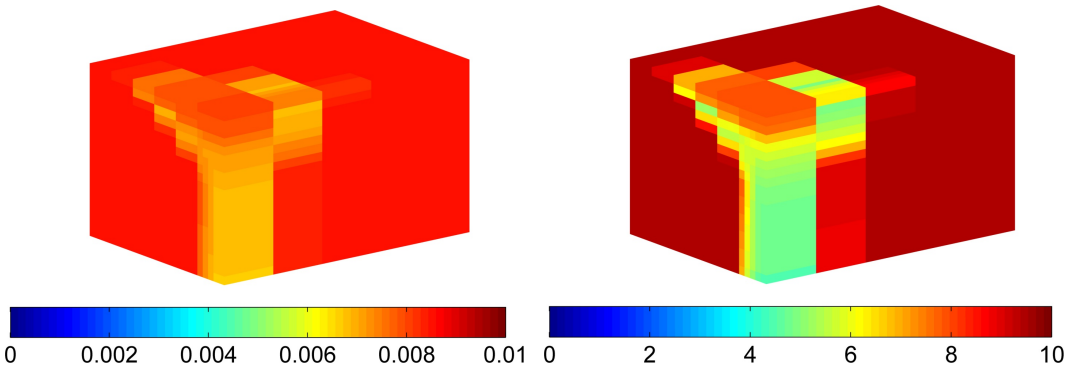

(a) Porosity, 100 yeras (b) Permeability(md), 100 years

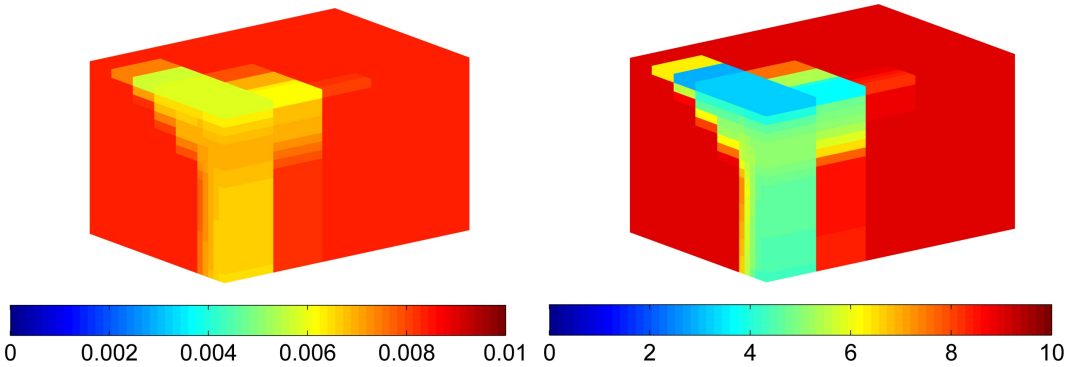

(c) Porosity, 300 years (d) Permeability(md), 300 years

Figure 4.13: Porosity and permeability fields at 100 and 300 years.

4.3.4 Vertical grid refinement

We have seen that the CO_2 distribution in the reservoir is of major importance for large-scale mineralization. In addition, the plume size and shape are impacted by gravity segregation. It is thus expected that the vertical grid resolution in the model may influence the mineralization progress.

Using the simplified reaction system, we now simulate the model using different numbers of grid blocks in the vertical direction (maintaining a 400 m thick reservoir). The convergence behavior for mineralization is shown in Fig. 4.15. It appears that convergence is essentially achieved with 20 layers. The magnesite profiles at 300 years shown in Fig. 4.16 further verify that convergence is essentially achieved at this vertical grid resolution. We thus establish a simulation model, consisting of 20 layers and employing the simplified reaction system, to serve as the base case for the sensitivity

Table 4.7: Simplified chemical reaction system used in mineralization examples.

Reaction #	Type	Reactions
1	Equilibrium	$MgCO_3 = Mg^{2+} + {CO_3}^{2-}$
2	Equilibrium	$MgHCO_3{}^{+} = Mg^{2+} + HCO_3{}^{-}$
3	Equilibrium	$CO_2(aq) + H_2O = H^{+} + HCO_3{}^{-}$
4	Equilibrium	$HCO_3{}^{-} = {CO_3}^{2-} + H^{+}$
5	Equilibrium	$H_2O = H^{+} + OH^{-}$
6	Kinetic	$Forsterite + 4\,H^{+} = 2\,Mg^{2+} + SiO_2(aq) + 2\,H_2O$
7	Kinetic	$Magnesite = Mg^{2+} + {CO_3}^{2-}$
8	Kinetic	$Quartz = SiO_2(aq)$
9	Kinetic	$Chrysotile + 6\,H^{+} = 3\,Mg^{2+} + 2\,SiO_2(aq) + 5\,H_2O$
10	Kinetic	$Brucite + 2\,H^{+} = Mg^{2+} + 2\,H_2O$

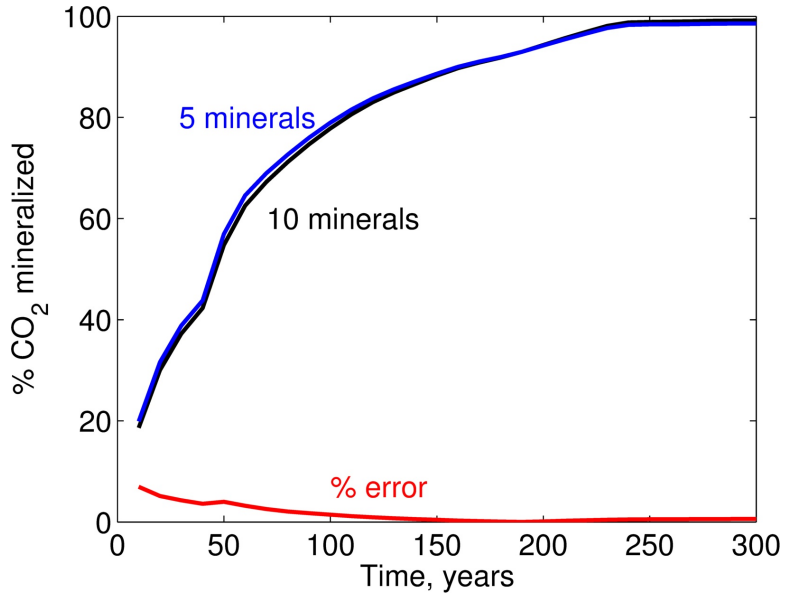

Figure 4.14: Comparison of mineralization results under two chemical reaction systems.

studies presented in the following section.

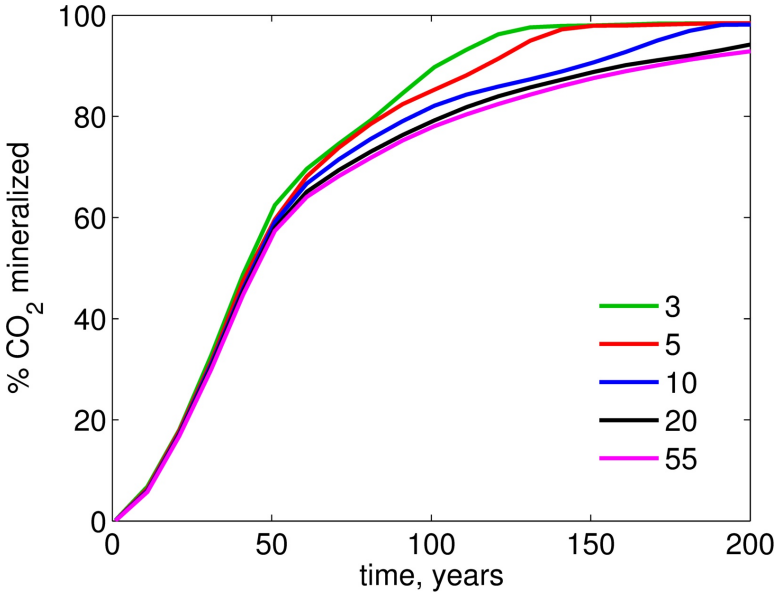

Figure 4.15: Mineralized CO_2 for various refinement levels in the vertical direction.

4.4 Sensitivity studies

In order to understand the impact of various factors on a sequestration project in ultramafic rocks, we now conduct sensitivity studies. In general, CO_2 solubility increases with increasing pressure and decreasing temperature and salinity [91]. The dissolved inorganic carbon (DIC) content in water is governed by both the partial pressure of CO_2 as well as the solution pH (DIC concentration rises with pH) [91]. We now consider the impact of some of these parameters on reservoir-scale carbonation.

4.4.1 Temperature dependence

The kinetic rates governing mineral dissolution and precipitation are a strong function of temperature, so temperature is of great importance in sequestration projects. The formation of carbonates due to the interactions of CO_2 and silicates such as forsterite, enstatite, serpentine, and anorthite is thermodynamically favorable at low temperatures and is accompanied by heat release [85, 63, 62, 102]. Note that at much higher temperatures, however, the reverse process is thermodynamically favored. At

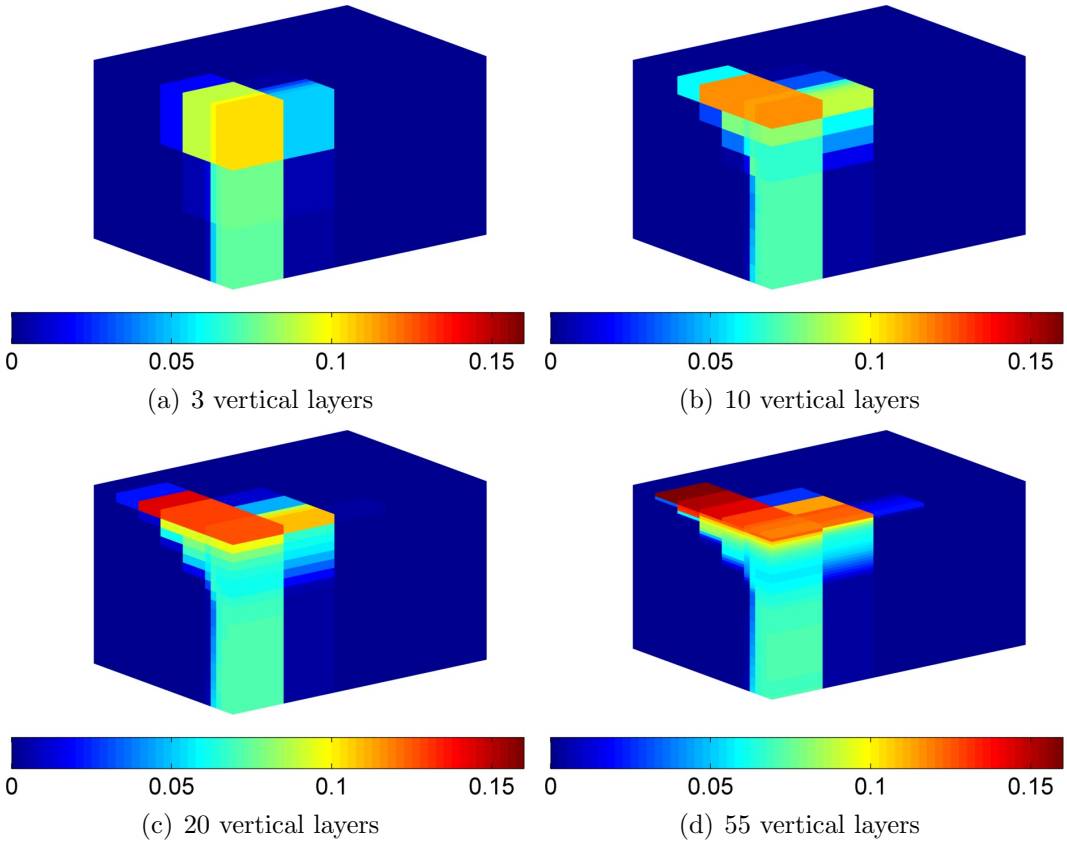

(a) 3 vertical layers (b) 10 vertical layers

(c) 20 vertical layers (d) 55 vertical layers

Figure 4.16: Magnesite precipitation profiles, in kmol/(m^3 bulk volume), at 300 years. These profiles are consistent with the convergence behavior observed in Fig. 4.15.

1 bar CO_2 partial pressure, this reversal occurs at temperatures beyond 900°C for Ca carbonates and 300°C for Mg carbonates [85].

Kelemen and Matter [53] calculated an optimal temperature at which peridotite carbonation rates are maximized. This temperature, between surface conditions and the equilibrium phase boundary for mineral stability, is calculated based on the competition between two phenomena. Specifically, higher temperatures encourage diffusive kinetics in both hydration and carbonation processes, though as the temperature approaches the equilibrium phase boundary for carbonate mineral stability, the chemical potential driving the reaction diminishes. Carbonation is maximized at 185°C at 150 bar CO_2 pressure.

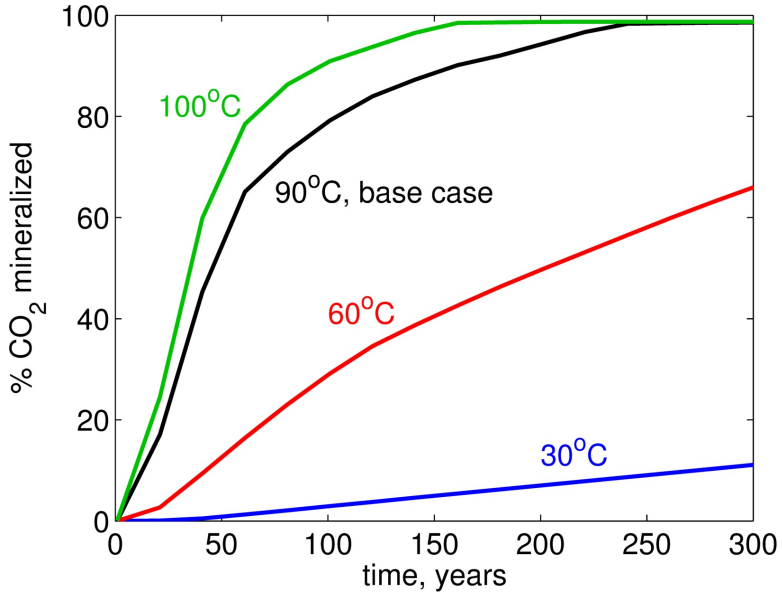

Figure 4.17: Mineralization progress for various reservoir temperatures.

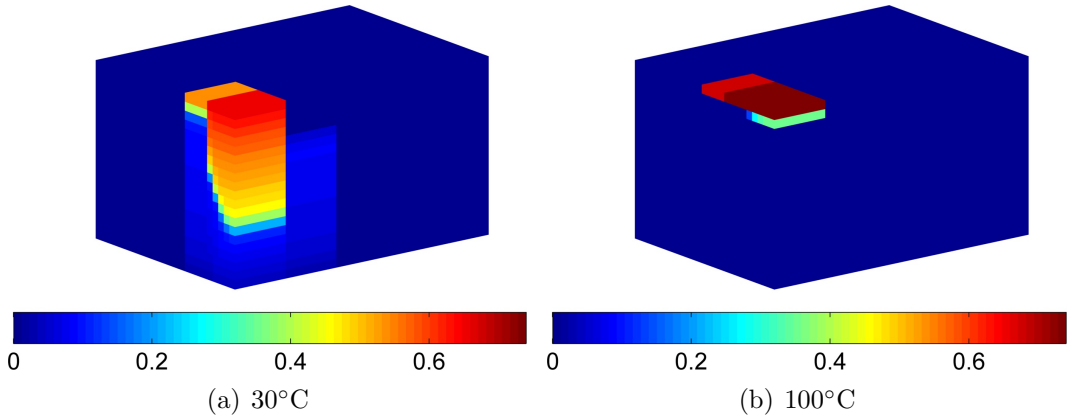

(a) 30°C (b) 100°C

Figure 4.18: Gas saturation profiles at 100 years for two different temperatures. The impact of gas phase density on CO_2 distribution is evident.

Kelemen and Matter [53] proposed preheating the reservoir to 185°C, and then maintaining that temperature through the chemical potential energy of the mantle peridotite. This could be achieved by exposing the reservoir to an optimal CO_2-brine mixture flow rate, where heat losses due to injection of cold fluids are balanced by the exothermic reactions. The flow rate must be sufficiently high to allow for adequate carbonation and thus heat generation, yet it should not be so high that advective heat

losses cool the formation. A flow rate of 0.040 m/s for injection of pure CO_2 at 300 bar and 25°C is the optimized value reported in [53]. Their simple one-dimensional model resulted in complete conversion of olivine in place to magnesite, fixing 2 Mt CO_2 per km^3.

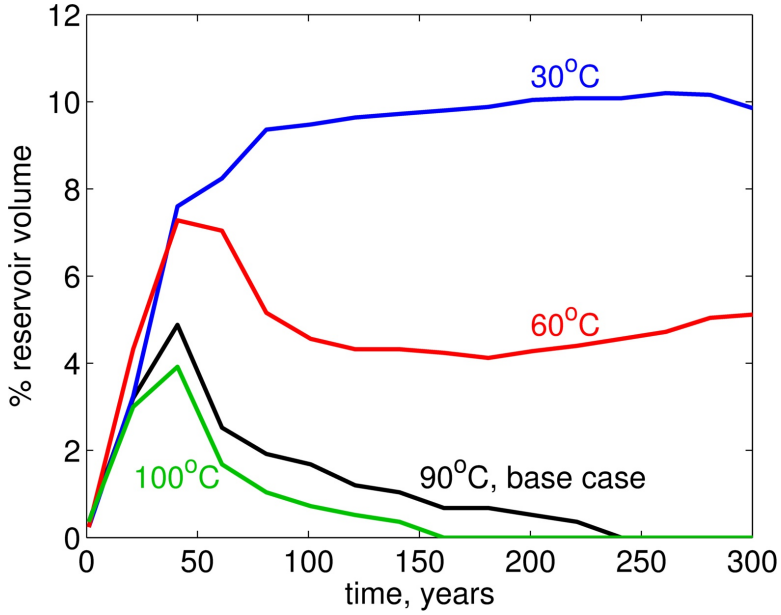

Figure 4.19: Percent reservoir volume exposed to free gas phase. Phase density influences the plume shape and thus the distribution of the gas phase, though faster kinetics at higher temperatures effectively removes CO_2 from the gas phase through mineralization.

Following a similar strategy, we conducted energy balance calculations for our three-dimensional storage problem. We concluded that the carbonation and hydration reactions do not have a notable impact on temperature in our model. Also, the energy release due to these reactions is compensated for in part by the injection of cold fluids. Thus, we believe that thermal simulation is not necessary, and our temperature sensitivity analysis will entail isothermal simulations.

Mineralization profiles for four different temperatures are shown in Fig. 4.17. The impact of temperature on kinetics accelerates the mineralization process as anticipated. In addition to kinetics, temperature also impacts phase properties such as density, and as a result affects gravity segregation and plume formation. This is depicted

in Fig. 4.18 where the plume shapes are compared for two different temperatures. At lower temperatures, the gas phase is more dense, hindering gravity segregation. The reservoir volume exposed to free gas is shown in Fig. 4.19. Even though lower temperatures (30°C) lead to more exposure to gas, the slower kinetics still result in much less mineralization than at higher temperatures.

4.4.2 Pressure dependence

Reservoir depth generally dictates initial pressure and temperature, and thus impacts CO_2 solubility, equilibrium constants, and kinetics. In this section, we consider changes in initial pressure, while keeping the temperature constant at 90°C, in order to isolate the influence of pressure.

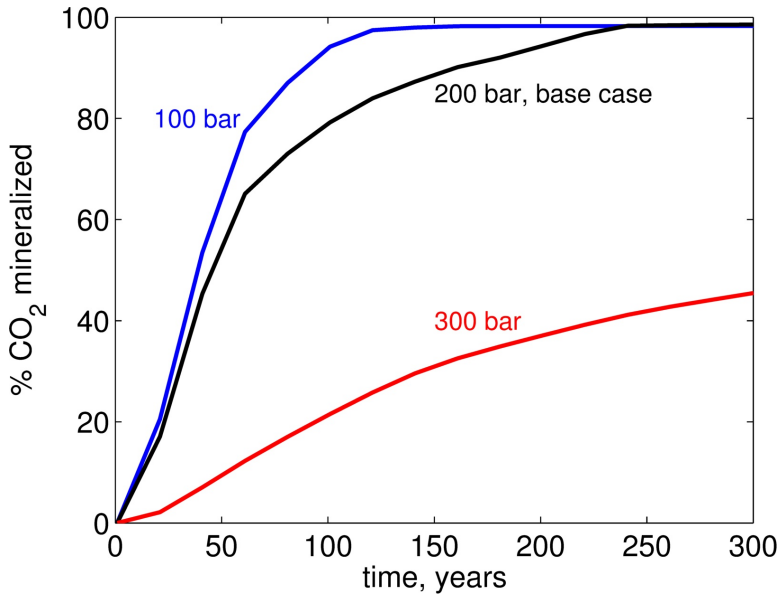

Figure 4.20: Mineralization progress for various initial reservoir pressures.

Mineralization results for three reservoir pressures are shown in Fig. 4.20. Increased pressure enhances CO_2 solubility and might thus be expected to enhance carbonation of the ultramafic minerals. We observe, however, slower mineralization at the reservoir scale for higher pressures. This can be explained in terms of the spread of the gas phase. In fact, similar to the temperature case, plume shapes and sizes are affected in

these scenarios due to the pressure dependence of phase densities, as seen in Fig. 4.21. The large-scale enhancement due to plume shape, observed at lower pressure, more than compensates for the reduction in local-scale CO_2 solubility.

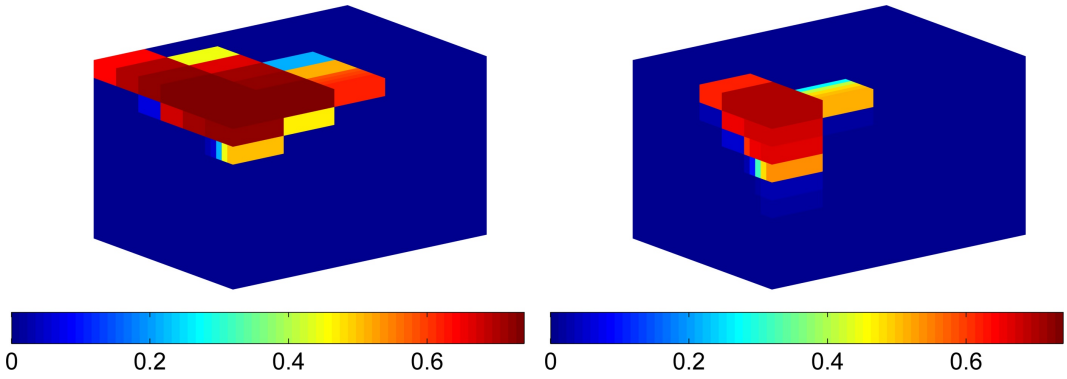

(a) 100 bar (b) 300 bar

Figure 4.21: Gas saturation profiles at 100 years for two different initial reservoir pressures.

4.4.3 Kinetic rate dependence

Throughout this chapter, relatively fast kinetic rate constants are assigned to secondary minerals based on the assumption that the dissolution of primary silicates is the rate-limiting step in the hydration and carbonation processes. In order to assess the impact of secondary mineral reaction rates on simulation results, we now vary these values while fixing the primary mineral kinetic rate constants. The mineralization progress is shown in Fig. 4.22 for the base case and three scenarios, where the k_r values are multiplied by 0.5, 0.2 and 0.01. Clearly, although mineralization is hindered by the slower kinetics, the general behavior is only weakly impacted for the multipliers of 0.5 and 0.2. Even with a multiplier of 0.01, significant mineralization still occurs.

In addition to the peridotite carbonation rate, the slower rates impact the profile of the permeability reduction in the reservoir. This is evident in the pattern of magnesite precipitation shown in Fig. 4.23. Note that these figures represent 65% mineralization for both scenarios, and thus correspond to different times.

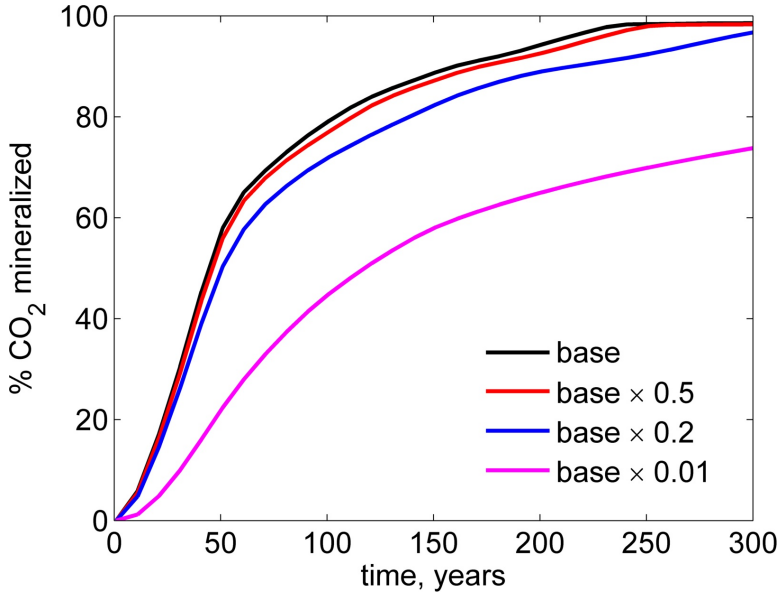

Figure 4.22: Mineralization progress for varying secondary mineral reaction rate constants.

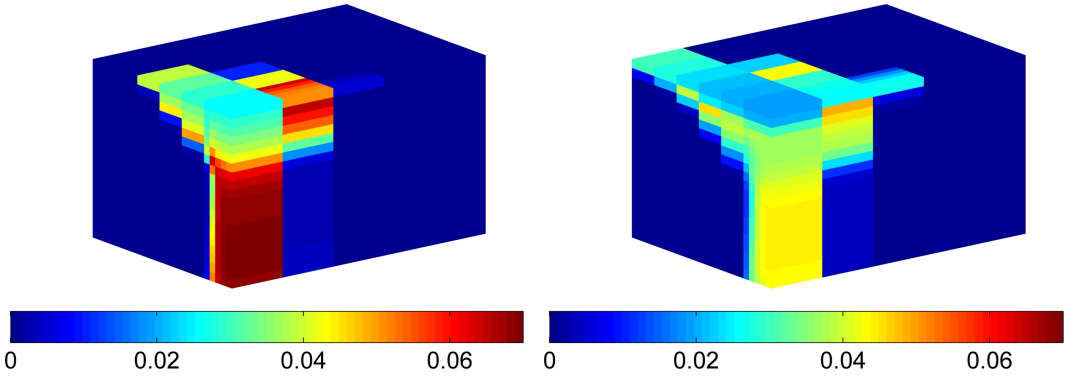

(a) Magnesite precipitation, base case (b) Magnesite precipitation, base case × 0.01

Figure 4.23: Magnesite precipitation profiles in kmol/(m^3 bulk volume). Results shown at 65% carbon mineralization for two different sets of secondary mineral kinetic reaction rates.

4.4.4 Permeability dependence

Reservoir properties such as permeability control multiphase flow and thus the plume shape, and as a result can impact mineralization. In Fig. 4.24, mineralization profiles are shown for different reservoir permeabilities. The anisotropic case corresponds to

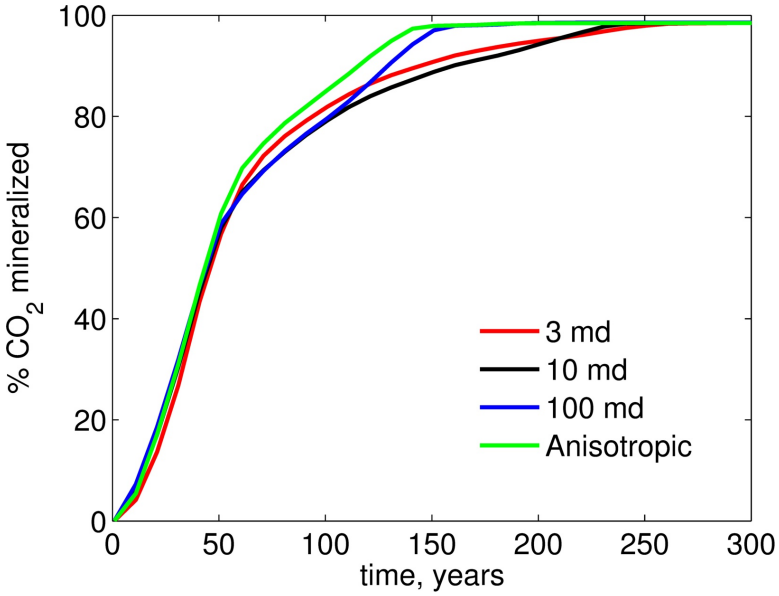

Figure 4.24: Mineralization progress for various reservoir permeabilities.

horizontal permeability of 100 md and vertical permeability of 3 md.

The magnesite profile facilitates the tracing of the plume history. The distribution of precipitated magnesite for two different permeability cases is presented at 50 years and 300 years in Fig. 4.25 in order to understand the impact of permeability. For the lower permeability case, the gravity segregation stage takes longer, and the first mineralization regime is in effect for a longer period of time. In other words, the initial rapid mineralization rate is maintained for longer. However, once the plume is formed at the top of the reservoir, the low permeability slows its spread, thus limiting the gas phase distribution. The mineralization rate is thus lower during this regime for lower permeability values. This is evident in Fig. 4.26, which shows the fraction of reservoir volume in contact with a free gas phase (and thus actively contributing to carbonation).

In the anisotropic case, mineralization benefits from both an extended first regime and a relatively high rate following plume formation due to the horizontal spreading. The outcome of a hydraulic fracturing operation thus will not only influence injectivity, but also the mineralization pattern and rate. Note that natural anisotropy may

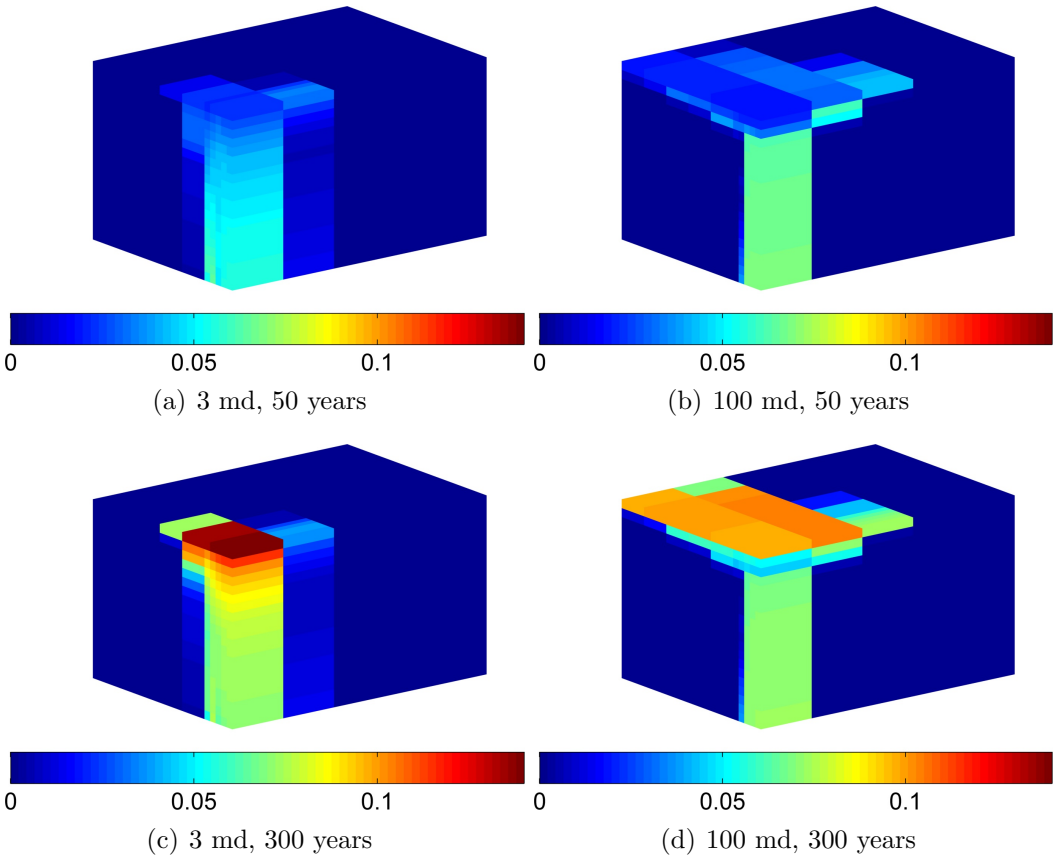

(a) 3 md, 50 years (b) 100 md, 50 years

(c) 3 md, 300 years (d) 100 md, 300 years

Figure 4.25: Magnesite precipitation profiles, in kmol/(m^3 bulk volume), at 50 years and 300 years for two different isotropic permeability values.

not necessarily be a plausible assumption as very little hydrological data exists on ultramafic rocks due to their low permeability.

4.4.5 Porosity dependence

Increased pore volume facilitates carbonation due to larger volumes of water having contact with the minerals. On the small scale, kinetics are linearly proportional to porosity. On the large scale, however, additional factors also control mineralization rate. Here we keep the reservoir size and the CO_2 injection rate constant, and only change the pore volume. Pore volume injected thus varies among the cases.

As shown in Fig. 4.27, mineralization is enhanced as reservoir pore volume increases.

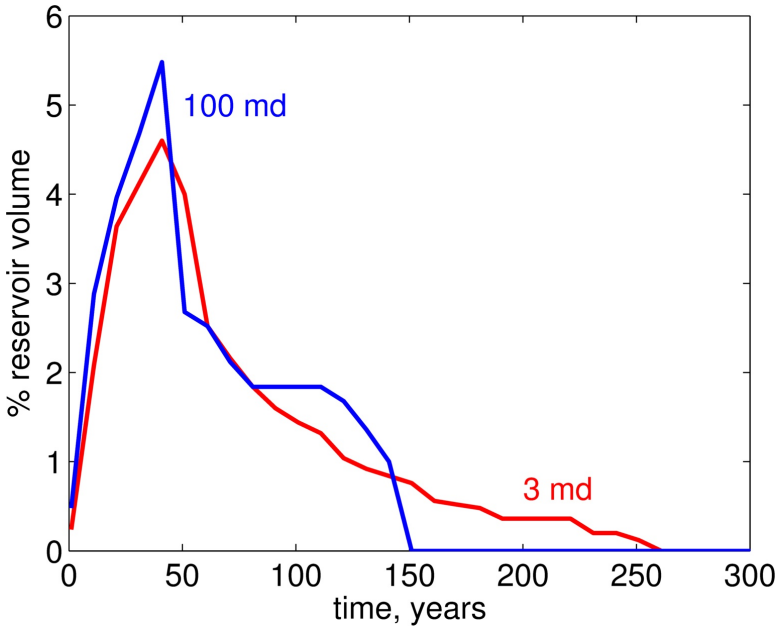

Figure 4.26: Percent reservoir volume exposed to free gas phase for two different permeability values.

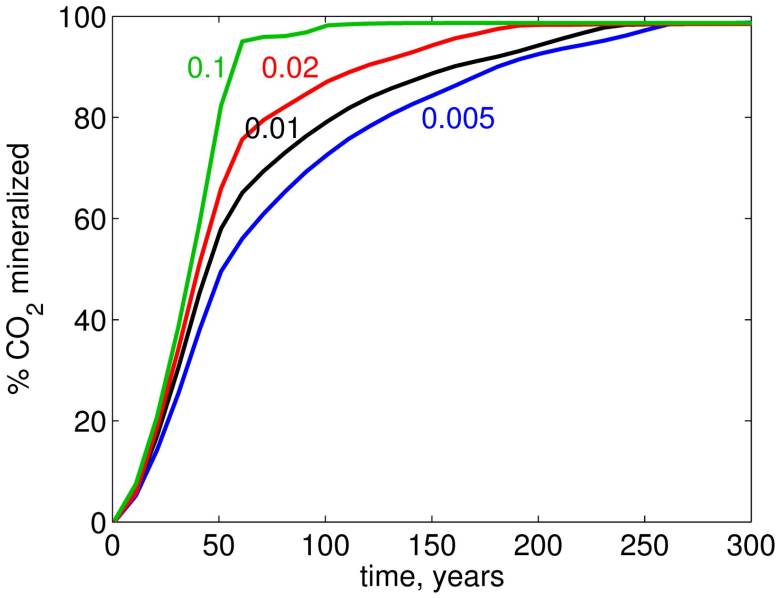

Figure 4.27: Mineralization progress for various reservoir porosity values.

The enhancement is not linearly proportional to porosity at the reservoir scale. The plume shapes are shown for two cases in Fig. 4.28. As illustrated in Fig. 4.29, despite

the plume expanding over a smaller region of the reservoir in the case of higher porosity values, a larger pore volume still contributes to kinetics in these scenarios.

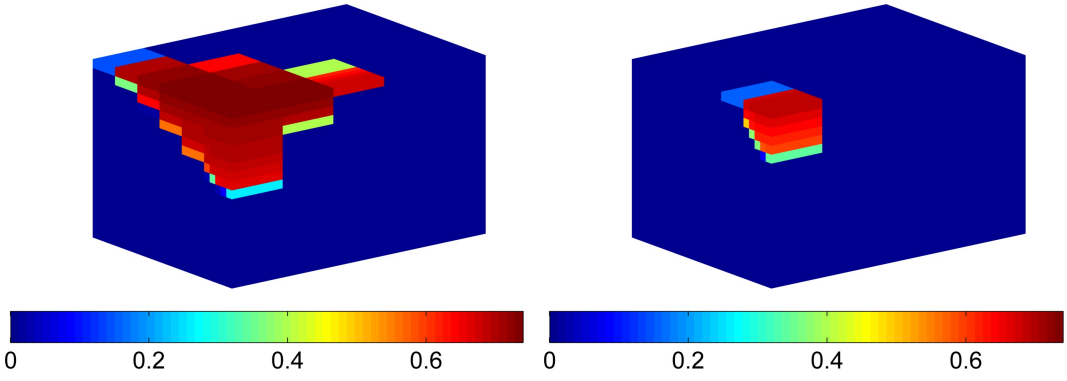

(a) $\phi = 0.005$ (b) $\phi = 0.02$

Figure 4.28: Gas saturation profiles at 50 years for two different porosity values.

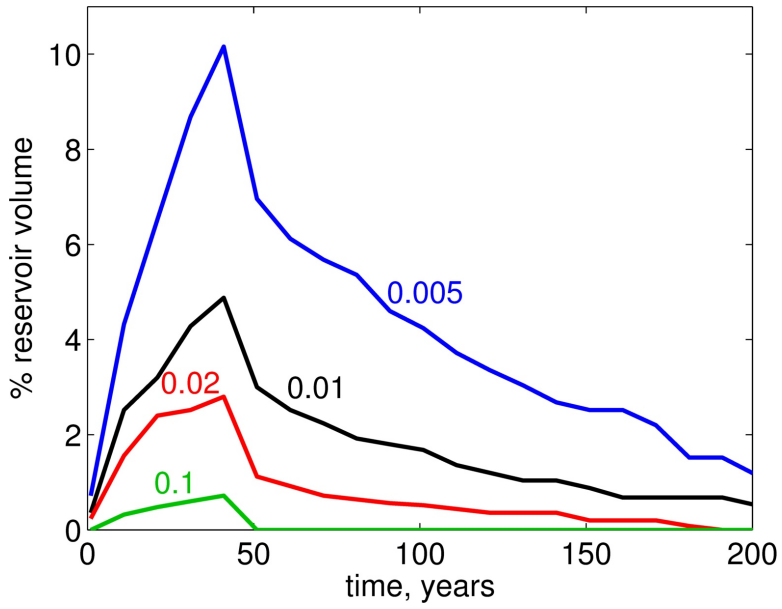

Figure 4.29: Percent reservoir volume exposed to free gas phase for various porosity values.

4.4.6 Well management

In this section, we demonstrate improvement in the mineralization rate in a sequestration project through management of the CO_2 injection. The goal is to enhance reservoir-scale mineralization for a fixed set of reservoir and kinetic parameters. Our approach entails improving CO_2 distribution in the reservoir by co-injecting water along with the CO_2. This impedes plume formation, and thus extends the productive first period of mineralization.

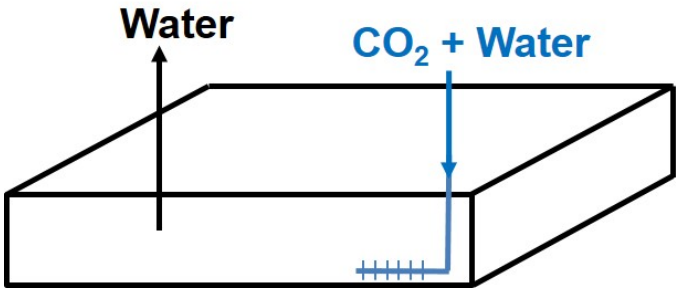

Figure 4.30: Schematic of the well management case, showing one quarter of the reservoir. CO_2 and water are co-injected from a horizontal well, while water is produced from a vertical well.

One quarter of the reservoir is again modeled, as shown in Fig. 4.30. CO_2 and water are co-injected from a horizontal well. Various CO_2/water ratios are considered. Water is continuously produced from a vertical well in order to prevent pressure buildup. The CO_2 rate is kept constant at 1 MT/year, while water volume is adjusted to vary the CO_2 fraction in the injection stream. Water injection and production are balanced at all times.

The mineralized CO_2 is shown in Fig. 4.31 for varying molar fractions of CO_2 in the injection stream. At lower CO_2 molar fractions, a free gas phase does not form immediately and a higher fraction of CO_2 is present in the form of aqueous species. The injection of higher volumes of fluid assists in expanding the access to CO_2. Wider regions thus participate in the mineralization process, and the first period of mineralization is highly effective. This is evident from the magnesite precipitation profiles shown in Fig. 4.32 at 50 years for two different cases.

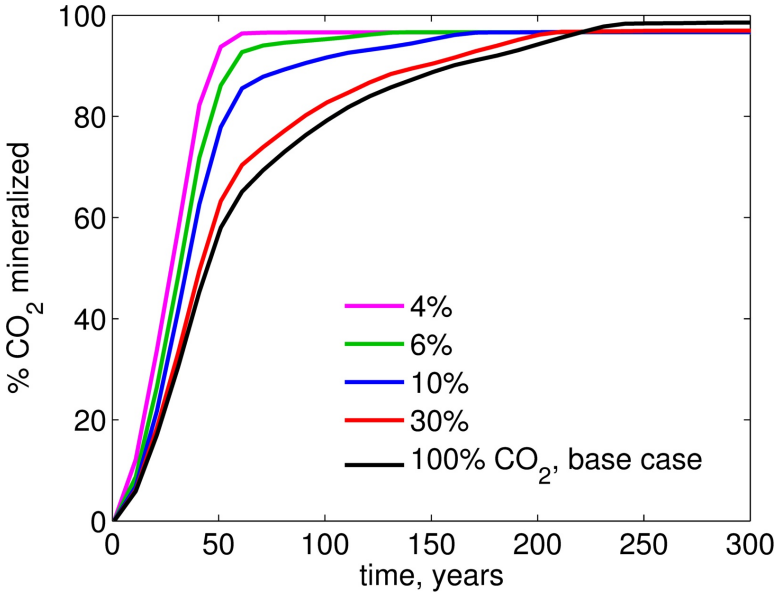

Figure 4.31: Mineralization results for varying molar fractions of CO_2 in the injection stream. Results generated using the model shown in Fig. 4.30.

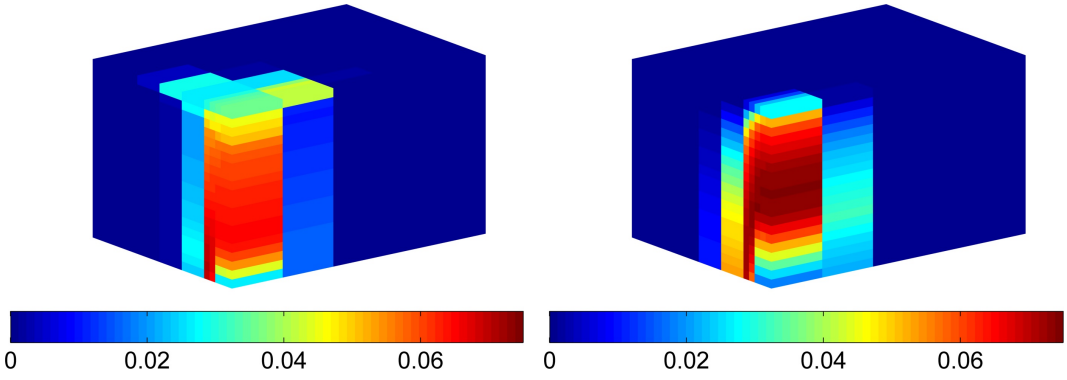

(a) 10% (b) 4%

Figure 4.32: Magnesite precipitation profiles, in kmol/(m^3 bulk volume), at 50 years for two different molar fractions of CO_2 in the injection stream. Results generated using the model shown in Fig. 4.30.

Alternatively, water may be injected through a horizontal well drilled above the first horizontal well, at the top of the formation, as shown in Fig. 4.33 [14]. This setup impedes CO_2 plume formation by redirecting the injected gas phase and thus preventing gravity segregation. The mineralization results for this scenario are shown

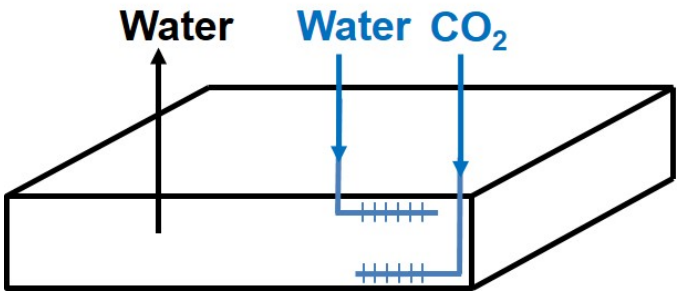

Figure 4.33: Schematic of the second well management case, showing one quarter of the reservoir. CO_2 and water are injected from two horizontal wells, while water is produced from a vertical well.

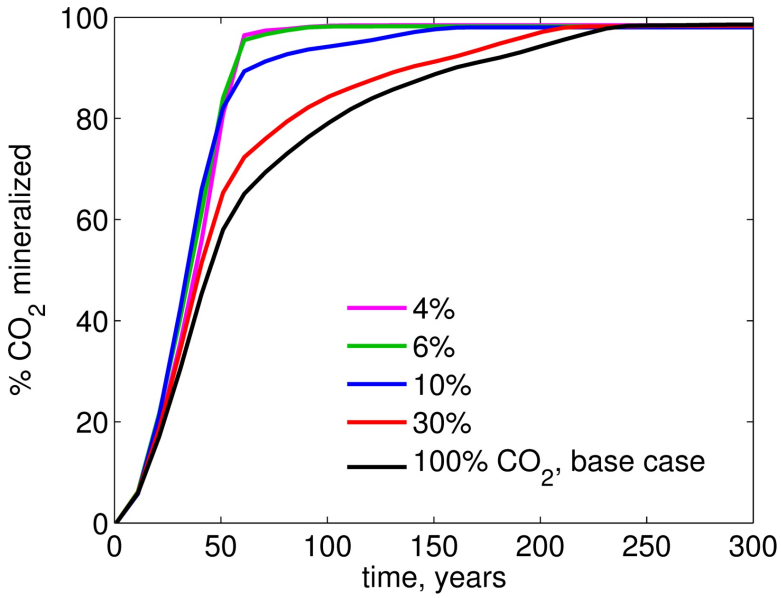

Figure 4.34: Mineralization results for varying molar fractions of CO_2 in the injection stream. Results generated using the model shown in Fig. 4.33.

in Fig. 4.34 for overall water and CO_2 injection rates equal to those for the cases presented in Fig. 4.31. Once again, water injection and production are balanced at all times. While the enhancement in carbonation rate is comparable to the two-well setup for lower water rates, differences are observed at higher rates. Unlike in the previous setup, very high water injection rates do not necessarily mean faster carbonation, particularly at early times. The comparison of the precipitated magnesite profiles for two different cases, shown in Fig. 4.35 at 50 years, demonstrates that very

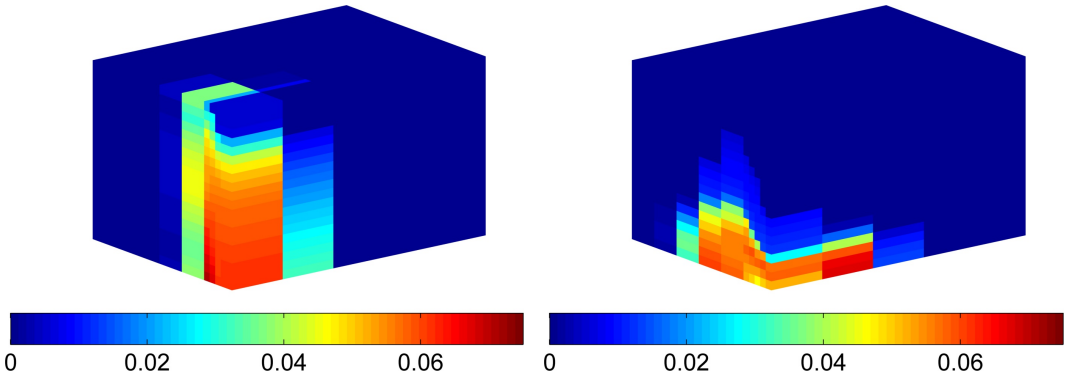

(a) 10% (b) 4%

Figure 4.35: Magnesite precipitation profiles, in kmol/(m^3 bulk volume), at 50 years for two different molar fractions of CO_2 in the injection stream. Results generated using the model shown in Fig. 4.33.

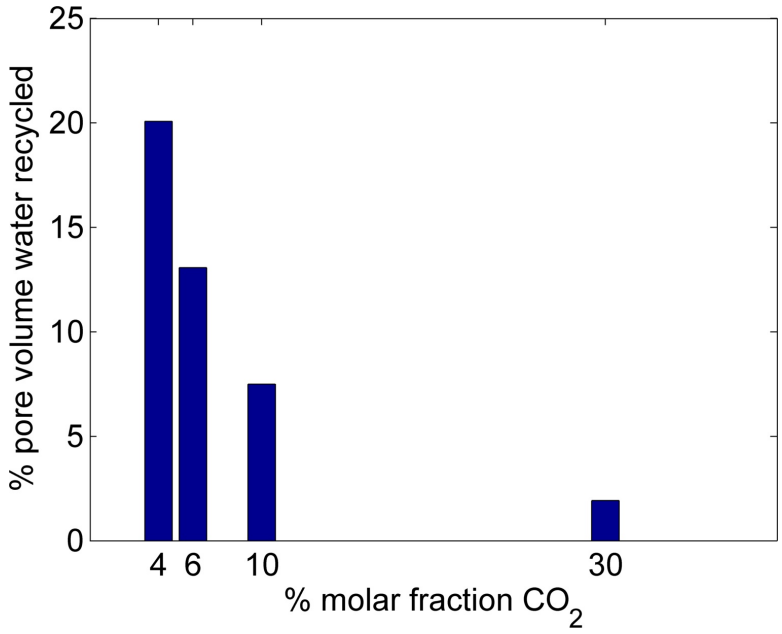

Figure 4.36: Recycled water volumes for cases shown in Figs. 4.31 and 4.34. Volumes are expressed in terms of percent reservoir pore volume, and are plotted against molar fraction of CO_2 in the (overall) injection stream.

high water injection rates restrict the injected CO_2 in a very limited region, and thus impede carbonation at early times.

The scenarios shown in Figs. 4.30 and 4.33 are both promising, and the choice of strategy will likely depend on various operational limitations and economic factors. The drawback of these approaches is that they require the cycling of large volumes of water, as seen in Fig. 4.36. Locating the operation in the proximity of abundant sources of water is thus an important consideration. The enhanced mineralization rate may justify the additional cost by, e.g., reducing monitoring requirements. Moreover, the costs associated with water injection might prove favorable in comparison to alternative strategies, such as preheating the reservoir.

4.5 Concluding remarks

In this chapter we investigated ultramafic rocks as a candidate for geological CO_2 storage. We discussed both natural weathering analogs and geological sequestration scenarios. In analyzing the weathering systems, we validated the results produced using AD-GPRS against the field data and geochemistry simulation analyses presented in Paukert et al. [88]. In our sequestration models, almost all of the CO_2 is converted into stable minerals, except for about one percent, which is trapped in the form of ions. Vertical grid resolution was shown to be important for quantifying mineralization.

We conducted a range of simulations to evaluate the impact of reservoir properties and operational factors on carbonation. As anticipated, a key parameter is temperature, which enhances the kinetics. In cases where we varied the initial pressure, we observed that the small changes in local-scale kinetics were more than compensated for by changes in multiphase flow behavior induced by pressure. Lower permeability reservoirs were shown to experience elevated mineralization rates at early time, and higher porosity values enhanced CO_2 storage by subjecting a larger pore volume to mineralization kinetics. Injection-well management was also investigated, and operating strategies involving the injection of water in addition to CO_2 were shown to improve mineralization.

Chapter 5

Summary, Conclusions and Future Work

This work entailed the development and implementation of robust numerical modeling techniques for simulating geological CO_2 storage. A target phenomenon of interest was CO_2 mineralization, which requires the modeling of chemical reactions. This physical setup requires the model to track many aqueous species that are absent from the gas phase, for example ions. In the absence of the aqueous phase, and under the standard natural-variable formulation, no subset of variables is valid for representing the system, resulting in mathematical complications at the linearized-solution level in a fully-implicit scheme, and thus lack of convergence. This drawback of the natural-variable formulation was a key motivation behind the numerical models developed in this work. The main features of these models are as follows:

- Our reactive transport model based on the natural-variable formulation was extended to include a new treatment for the special case of aqueous phase disappearance. This treatment entails the introduction of a deposition phase, which holds aqueous species in the absence of the water phase. The transfer of material between the aqueous and the deposition phases was achieved through a (heuristic) kinetic reaction.

- A novel reactive transport model based on overall-composition variables was formulated and implemented. The overall-composition variables are valid under

all fluid phase combinations, rendering variable switching unnecessary. Accordingly, aqueous phase disappearance and reappearance are effectively treated. A major drawback of this approach however, is the high cost of phase equilibrium calculations.

- A hybrid formulation was thus proposed. This approach uses natural variables in all fluid phase combinations except for single-phase gas, where it uses overall-composition variables. The hybrid model thus benefits from the advantages of both numerical treatments.

The reactive-transport numerical frameworks described above were implemented in Stanford's Automatic Differentiation-based General Purpose Research Simulator (AD-GPRS) and applied to the problem of geological carbon storage. The key findings from this study are as follows:

- Field-scale, three-dimensional storage scenarios in sandstones were simulated, accounting for various carbon storage mechanisms. Despite choosing a sandstone composed of minerals likely to react in the presence of CO_2, the majority of the injected CO_2 remained in a free gas phase, and only about 10% carbonation was observed after 2000 years.

- For the two-phase two-component compositional model, the natural and overall-composition variable formulations displayed similar time-stepping behavior and numerical performance, but differed in terms of the cost of thermodynamic calculations. Specifically, in grid blocks experiencing two fluid phases, the overall-composition variable formulation requires flash calculations at all Newton iterations, while the use of natural variables avoids this extra step.

- The comparison of our fully-implicit natural and overall-composition variable formulations under reactive transport scenarios led to conclusions similar to those in the case of non-reactive compositional models. The extra cost of phase equilibrium calculations may however be even higher with overall-composition variables when reactions are present.

- We demonstrated that the introduction of aqueous species (even in trace amounts) was the source of some of the major complications observed in the numerical

simulation of geological carbon storage. The three numerical formulations were all shown to be capable of treating aqueous phase disappearance in such cases. The overall-composition variable formulation can resolve the diminishing water saturation with more accuracy than the natural variable-based treatment, though it may require time step cuts.

- We conclude that natural variables generally offer superior computational efficiency compared to overall-compositional variables. Also, in an existing simulator based on natural variables, we believe that deposition modeling is the preferred approach in treating the aqueous phase disappearance problem, primarily due to the ease of implementation. This is because, unlike in the hybrid model, it does not require a change in the nonlinear formulation.

We then employed our reactive transport simulator to analyze ultramafic rocks as host rocks for CO_2 sequestration. These rocks offer fast reaction rates and high storage capacity due to the constituent minerals. We began by analyzing two stages of a weathering system in peridotites of Samail Ophiolite in Oman where field observations and a geochemistry study were reproduced [88]. Our specific findings are as follows:

- The evolution of water composition was tracked from rainwater to shallow groundwater in order to model the first stage of the weathering process, which occurs in contact with the atmosphere. Reported laboratory analyses of samples obtained from the surface and shallow groundwater were used to verify our simulation results. The calculated mineral precipitation was also in agreement with field observations [88].

- The next stage of weathering occurs at greater depths and in the absence of any contact with the atmosphere. The evolution of water composition was again in agreement with samples of water from alkaline springs in the peridotite formation (measured in [88]). Moreover, the model provided mineral precipitation profiles close to the field observations [88].

We then investigated the outcome of a field-scale CO_2 sequestration project in an idealized peridotite reservoir. Our findings are as follows:

- A base case reservoir was established using typical values reported for peridotite formations, and a permeability of 10 md. The reaction system was based on the weathering system analysis. Almost complete mineralization of CO_2 was observed, enhancing trapping security dramatically compared to the case of sandstone formations.

- A sensitivity analysis was then performed by changing various reservoir and operation parameters. Temperature was found to have a substantial impact on the mineralization results due to its impact on the kinetic rates. Other parameters, such as pressure, permeability, and porosity influence the large-scale mineralization results through their effect on the distribution of CO_2 in the reservoir.

- Well operation scenarios were then studied to enhance and accelerate the mineral trapping of CO_2. Two strategies involving simultaneous injection of water and CO_2 were found to be quite effective in this regard.

Future work

Many aspects of this work should be investigated further, both on the formulation and application sides. Specifically, the following areas are suggested for future research:

- Mixed-implicit treatments should be considered to reduce computational time and memory requirements for problems with many aqueous species, minerals, and reactions.

- More detailed, and specific modeling of ultramafic reservoirs should be performed. The idealized models employed in our simulation cases could be replaced by discrete fracture models to better represent the hydraulically fractured system. This should yield more accurate estimates of the distribution of CO_2, and thus mineralization, in this type of reservoir.

- Integration of geomechanical calculations into the reactive-transport simulator will enable the modeling of reaction-induced fractures, which are expected to occur in ultramafic rocks [56] and may also occur in sandstone aquifers. Moreover, permeability and porosity evolution can play a major role on the final

mineralization outcome in ultramafic rocks. Field-scale and experimental observations should be employed to develop appropriate modeling techniques for these important phenomena [115].

- In order to take advantage of the rapid kinetics in ultramafic rocks, optimization techniques may be employed to determine operating parameters [14], including stimulation techniques, that yield the most favorable carbonation outcome.

Nomenclature

Greek Symbols

α_i	mole fraction of component i in deposited phase
γ_c	activity coefficient of component c
μ_c	chemical potential of component c
μ_j	viscosity of phase j
ν	phase molar fractions
Ω	mineral saturation index
ϕ	fluid-filled porosity
ϕ_r	reactive solid-filled porosity
ϕ_0	initial porosity at reference pressure
ρ_i^m	density of mineral i
ρ_j	density of phase j
ρ_{rock}	rock density
ρ_T	overall density for fluid phases
τ	tortuosity
$\tilde{\phi}$	total porosity
υ	stoichiometric coefficient
ζ_m	mass fraction of mineral m in the rock

Variables

$\bar{\mathbf{S}}$	canonical stoichiometric matrix
$\bar{\mathbf{S}}_k$	canonical kinetic stoichiometry matrix
$\bar{\mathbf{S}}_q$	canonical equilibrium stoichiometry matrix
$\dot{B}$	B-dot parameter

$\mathbf{R}_{lp}$	vector of linear primary residual equations
$\mathbf{R}_{ls}$	vector of linear secondary residual equations
$\mathbf{R}_{p}$	vector of primary residual equations
$\mathbf{R}_{s}$	vector of secondary residual equations
$\mathbf{x}_{lp}$	vector of linear primary variables
$\mathbf{x}_{ls}$	vector of linear secondary variables
$\mathbf{x}_{p}$	vector of primary variables
$\mathbf{x}_{s}$	vector of secondary variables
$\mathbf{D}_{ij}$	dispersion tensor for component i in phase j
$\mathbf{E}$	equilibrium rate annihilation matrix
$\mathbf{E}_1$	element stoichiometric matrix
$\mathbf{F}$	formula matrix
$\mathbf{I}$	identity matrix
$\mathbf{J}$	Jacobian matrix
$\mathbf{K}$	absolute permeability tensor
$\mathbf{L}$	flux term
$\mathbf{N}$	vector of total component concentrations
$\mathbf{R}$	residual vector
$\mathbf{r}$	vector of reaction rates
$\mathbf{S}$	stoichiometric matrix
$\mathbf{u}_j$	Darcy velocity of phase j
$\mathbf{x}$	vector of unknowns
A	mineral surface area
A_i	chemical formula for species i
a_{H^+}	activity of H^+
A_γ	Debye-Hückel A parameter
a_{ij}	activity of component i in phase j
$A_{s,m}$	specific surface area of mineral m
B_γ	Debye-Hückel B parameter
c_r	rock compressibility
C_m	concentration of mineral m
$c_{r,nr}$	compressibility factor of the nonreactive solid portion of the rock

D	depth
D_p	a measure of the dependence of permeability on pore size
Da	Damköhler number
E_α	activation energy for kinetic reaction α
f_{ij}	fugacity of component i in phase j
g	gravitational acceleration
I	ionic strength
k^D	dissolution reaction rate constant
K^{eq}	reaction equilibrium constant
$k^{T_{ref}}$	pre-exponential factor
k_a	kinetic rate constant for the acid mechanism
k_b	kinetic rate constant for the base mechanism
k_n	kinetic rate constant for the neutral mechanism
k_{rj}	relative permeability to phase j
M_i^D	mass of component i in deposited phase
$m_{i,w}$	molality of component i in water phase
n_e	number of elements
n_f	number of fluid components
N_i	mass concentration per bulk volume for component i
n_k	number of kinetic reactions
n_m	number of solid components
n_p	number of phases
n_q	number of equilibrium reactions
n_r	number of total reactions
n_s	number of total components
n_u	number of unknowns
n_{aq}	number of aqueous species excluding CO_2 and H_2O
n_{kf}	number of fluid kinetic reactions
n_{lpr}	number of linear primary variables
n_{lsec}	number of linear secondary variables
N_{n_f+m}	mass concentration per bulk volume for mineral m
n_{pr}	number of primary variables

n_{sec}	number of secondary variables
P_c	capillary pressure
p_j	pressure of phase j
p_{ref}	reference pressure
Q	reaction activity product
q_i^D	dissolution rate for aqueous component i
q_i^W	well source term for component i
R	gas constant
r^D	dissolution reaction rate
r_q	equilibrium reaction rate
r_k	kinetic reaction rate
S_i^m	mineral saturation
S_j	saturation of phase j
T	absolute temperature
t	time
T_{ref}	reference temperature
V_ϕ	pore volume
V_{nr}	nonreactive solid volume
$V_{r,i}$	volume of reactive mineral i
V_r	reactive solid volume
X_{ij}	mole fraction of component i in phase j
Z_i	electrical charge of component i
z_i	overall composition for component i
$\overset{o}{a}_c$	ion size of component c

Subscripts

0	initial value
g	gas phase
k	kinetic reaction
o	oil phase
p	primary variable
q	equilibrium reaction
ref	reference pressure

s	secondary variable
w	water phase

Superscripts

0	standard state

Bibliography

[1] User's guide for UTCHEM-9.0: A three-dimensional chemical flood simulator. Reservoir Engineering Research Program, Center for Petroleum and Geosystems Engineering, The University of Texas at Austin, 2000.

[2] Stars user's manual. *Computer Modelling Group*, 2015.

[3] G. Acs, S. Doleschall, and E. Farkas. General purpose compositional model. *Society of Petroleum Engineers Journal*, 25(4):543–553, 1985.

[4] E. Aharonov, E. Tenthorey, and C. H. Scholz. Precipitation sealing and diagenesis: 2. Theoretical analysis. *Journal of Geophysical Research: Solid Earth*, 103(B10):23969–23981, 1998.

[5] M. Andreani, L. Luquot, P. Gouze, M. Godard, E. Hois, and B. Gibert. Experimental study of carbon sequestration reactions controlled by the percolation of CO_2-rich brine through peridotites. *Environmental Science & Technology*, 43(4):1226–1231, 2009.

[6] R. Aris. Prolegomena to the reaction analysis of systems of chemical reactions. *Archive for Rational Mechanics and Analysis*, 19(2):81–99, 1965.

[7] R. Aris and R. H. S. Mahi. Independence of chemical reactions. *Industrial and Engineering Chemistry Fundamentals*, 2:90–94, 1963.

[8] I. Barnes and J. R. O'Neil. The relationship between fluids in some fresh alpine-type ultramafics and possible modern serpentinization, western United States. *Geological Society of America Bulletin*, 80:1947–1960, 1969.

[9] K. Becker and E. E. Davis. New evidence for age variation and scale effects of permeabilities of young oceanic crust from borehole thermal and pressure measurements. *Earth and Planetary Science Letters*, 210(34):499 – 508, 2003.

[10] C. M. Bethke. *Geochemical and Biogeochemical Reaction Modeling*. Cambridge University Press, Cambridge, 2008.

[11] D. Bhuyan, L. W. Lake, and G. A. Pope. Mathematical modeling of high-pH chemical flooding. *SPE Reservoir Engineering*, 5(2):213–220, 1990.

[12] J. D. Bolling. Development and application of a limited-compositional, miscible flood reservoir simulator. Paper SPE 15998 presented at the SPE Symposium on Reservoir Simulation, San Antonio, Texas, USA, 1987.

[13] D. P. Butt, K. S. Lackner, C. H. Wendt, S. D. Conzone, H. Kung, Y. Lu, and J. K. Bremser. Kinetics of thermal dehydroxylation and carbonation of magnesium hydroxide. *Journal of the American Ceramic Society*, 79(7):1892–1898, 1996.

[14] D. A. Cameron and L. J. Durlofsky. Optimization of well placement, CO_2 injection rates, and brine cycling for geological carbon sequestration. *International Journal of Greenhouse Gas Control*, 10:100–112, 2012.

[15] H. Cao. *Development of techniques for general purpose simulators*. PhD thesis, Stanford University, 2002.

[16] S. A. Carroll and K. G. Knauss. Dependence of labradorite dissolution kinetics on CO_2(aq), Al(aq), and temperature. *Chemical Geology*, 217(34):213–225, 2005.

[17] M. C. H. Chien, S. T. Lee, and W. H. Chen. A new fully implicit compositional simulator. Paper SPE 13385 presented at the SPE Symposium on Reservoir Simulation, Dallas, Texas, USA, 1985.

[18] K. H. Coats. An equation of state compositional model. *Society of Petroleum Engineers Journal*, 20(5):363–376, 1980.

[19] K. H. Coats, L. K. Thomas, and R. G. Pierson. Compositional and black-oil reservoir simulation. *SPE Reservoir Evaluation & Engineering*, 1(4):372–379, 1998.

[20] D. A. Collins, L. X. Nghiem, Y.-K. Li, and J. E. Grabonstotter. An efficient approach to adaptive-implicit compositional simulation with an equation of state. *SPE Reservoir Engineering*, 7(2):259 – 264, 1992.

[21] R. Courant, K. Friedrichs, and H. Lewy. On the partial difference equations of mathematical physics. *IBM Journal of Research and Development*, 11(2):215–234, 1967.

[22] T. A. Davis. Algorithm 832: UMFPACK, an unsymmetric-pattern multifrontal method. *ACM Transactions on Mathematical Software*, 30(2):196 – 199, 2004.

[23] B. Dewandel, P. Lachassagne, F. Boudier, S. Al-Hattali, B. Ladouche, J. L. Pinault, and Z. Al-Suleimani. A conceptual hydrogeological model of ophiolite hard-rock aquifers in Oman based on a multiscale and a multidisciplinary approach. *Hydrogeology Journal*, 13(5):708–726, 2005.

[24] S. Emmanuel and B. Berkowitz. Suppression and stimulation of seafloor hydrothermal convection by exothermic mineral hydration. *Earth and Planetary Science Letters*, 243(34):657–668, 2006.

[25] M. Fahs, J. Carrayrou, A. Younes, and P. Ackerer. On the efficiency of the direct substitution approach for reactive transport problems in porous media. *Water, Air, and Soil Pollution*, 193:299–308, 2008.

[26] Y. Fan. *Chemical reaction modeling in a subsurface flow simulator with application to in-situ upgrading and CO_2 mineralization.* PhD thesis, Stanford University, 2010.

[27] Y. Fan, L. J. Durlofsky, and H. A. Tchelepi. Numerical simulation of the in-situ upgrading of oil shale. *Society of Petroleum Engineers Journal*, 15(2):368–381, 2010.

[28] Y. Fan, L. J. Durlofsky, and H. A. Tchelepi. A fully-coupled flow-reactive-transport formulation based on element conservation, with application to CO_2 storage simulations. *Advances in Water Resources*, 42:47–61, 2012.

[29] Y. Fang. A general paradigm to model reaction-based biogeochemical processes in batch systems. *Water Resources Research*, 39(4):1–25, 2003.

[30] Y. Fang, G. T. Yeh, and W. D. Burgos. A general paradigm to model reaction-based biogeochemical processes in batch systems. *Water Resources Research*, 39(4):1083–1107, 2003.

[31] S. F. Farshidi, Y. Fan, L. J. Durlofsky, and H. A. Tchelepi. Chemical reaction modeling in a compositional reservoir-simulation framework. Paper SPE 163677 presented at the SPE Reservoir Simulation Symposium, The Woodlands, Texas, USA, 2013.

[32] A. Flaaten, Q. Nguyen, J. Zhang, H. Mohammadi, and G. Pope. Alkaline/surfactant/polymer chemical flooding without the need for soft water. *Society of Petroleum Engineers Journal*, 15(1):184–196, 2010.

[33] H. S. Fogler. *Elements of Chemical Reaction Engineering*. 2005.

[34] T. D. Fowler and H. J. Vinegar. Oil shale ICP - Colorado field pilots. Paper SPE 121164 presented at the SPE Western Regional Meeting, San Jose, California, USA, 2009.

[35] L. T. Fussell and D. D. Fussell. An iterative technique for compositional reservoir models. *Society of Petroleum Engineers Journal*, 19(4):211–220, 1979.

[36] P. García del Real, K. Maher, G. E. Brown, Jr., and D. K. Bird. Massive magnesite veins in peridotite: A result of thermal fracturing by CO_2-rich fluids. Presented at the American Geophysical Union, San Francisco, California, USA, 2013.

[37] P. García del Real, K. Maher, G. E. Brown, Jr., and D. K. Bird. Thermal fracturing of crustal ultramafic rocks for geologic CO_2 sequestration. *in review Geology*, 2016.

[38] P. García del Real and V. Vishal. *Mineral Carbonation in Ultramafic and Basaltic Rocks*. Geologic Carbon Sequestration. Springer, 2016.

[39] S. J. Gerdemann, W. K. O'Connor, D. C. Dahlin, L. R. Penner, and H. Rush. Ex situ aqueous mineral carbonation. *Environmental Science & Technology*, 41(7):2587–2593, 2007.

[40] S. M. V. Gilfillan, B. S. Lollar, G. Holland, D. Blagburn, S. Stevens, M. Schoell, M. Cassidy, Z. Ding, Z. Zhou, G. Lacrampe-Couloume, and C. J. Ballentine. Solubility trapping in formation water as dominant CO_2 sink in natural gas fields. *Nature*, 458:614–618, 2009.

[41] W. D. Gunter, E. H. Perkins, and I. Hutcheon. Aquifer disposal of acid gases: modelling of water-rock reactions for trapping of acid wastes. *Applied Geochemistry*, 15(8):1085–1095, 2000.

[42] G. Hammond, P. C. Lichtner, and C. Lu. Subsurface multiphase flow and multicomponent reactive transport modeling using high-performance computing. *Journal of Physics: Conference Series*, 78:12–25, 2007.

[43] G. E. Hammond, A. J. Valocchi, and P. C. Lichtner. Application of Jacobian-free Newton-Krylov with physics-based preconditioning to biogeochemical transport. *Advances in Water Resources*, 28:359–376, 2005.

[44] M. Hanchen, V. Prigiobbe, R. Baciocchi, and M. Mazzotti. Precipitation in the Mg-carbonate system – effects of temperature and CO_2 pressure. *Chemical Engineering Science*, 63(4):1012–1028, 2008.

[45] A. L. Harrison, I. M. Power, and G. M. Dipple. Accelerated carbonation of brucite in mine tailings for carbon sequestration. *Environmental Science & Technology*, 47(1):126–134, 2013.

[46] H. C. Helgeson and D. H. Kirkham. Theoretical prediction of the thermodynamic behaviour of aqueous electrolytes at high pressure and temperatures: II. Debye-Hückel parameters for activity coeffcients and relative partial molal properties. *American Journal of Science*, 274:1199–1261, 1974.

[47] J. Hövelmann, H. Austrheim, and B. Jamtveit. Microstructure and porosity evolution during experimental carbonation of a natural peridotite. *Chemical Geology*, 334:254–265, 2012.

[48] A. Iranshahr, D. V. Voskov, and H. A. Tchelepi. Tie-simplex based compositional space parameterization: Continuity and generalization to multiphase systems. *American Institute of Chemical Engineers Journal*, 59(5):1684–1701, 2013.

[49] K. Iyer, B. Jamtveit, J. Mathiesen, A. Malthe-Srenssen, and J. Feder. Reaction-assisted hierarchical fracturing during serpentinization. *Earth and Planetary Science Letters*, 267(34):503–516, 2008.

[50] Y. Jiang. *Techniques for modeling complex reservoirs and advanced wells*. PhD thesis, Stanford University, 2007.

[51] N. C. Johnson, B. Thomas, K. Maher, R. J. Rosenbauer, D. Bird, and G. E. Brown, Jr. Olivine dissolution and carbonation under conditions relevant for in situ carbon storage. *Chemical Geology*, 373:93–105, 2014.

[52] P. B. Kelemen and G. Hirth. Reaction-driven cracking during retrograde metamorphism: Olivine hydration and carbonation. *Earth and Planetary Science Letters*, 345-348:81–89, 2012.

[53] P. B. Kelemen and J. Matter. In situ carbonation of peridotite for CO_2 storage. *Proceedings of the National Academy of Sciences of the United States of America*, 105(45):17295–17300, 2008.

[54] P. B. Kelemen, J. Matter, E. E. Streit, J. F. Rudge, W. B. Curry, and J. Blusztajn. Rates and mechanisms of mineral carbonation in peridotite: Natural processes and recipes for enhanced, in situ CO_2 capture and storage. *Annual Review of Earth and Planetary Sciences*, 39(1):545–576, 2011.

[55] P. B. Kelemen, J. Matter, and L. Streit. Field observations and theoretical studies relevant to enhanced in situ mineral carbonation of peridotite. Presented at the 2nd International Conference on Accelerated Carbonation for Environmental and Materials Engineering, Rome, Italy, 2008.

[56] P. B. Kelemen, H. Savage, and G. Hirth. Reaction-driven cracking during mineral hydration, carbonation and oxidation. *Poromechanics V*, pages 823–826, 2013.

[57] Y. K. Kharaka, D. R. Cole, S. D. Hovorka, W. D. Gunter, K. G. Knauss, and B. M. Freifeld. Gas-water-rock interactions in Frio formation following CO_2 injection: Implications for the storage of greenhouse gases in sedimentary basins. *Geology*, 34(7):577–580, 2006.

[58] K. G. Knauss, S. N. Nguyen, and H. C. Weed. Diopside dissolution kinetics as a function of pH, CO_2, temperature, and time. *Geochimica et Cosmochimica Acta*, 57(2):285–294, 1993.

[59] K. B. Krauskopf and D. K. Bird. *Introduction to Geochemistry*. 1994.

[60] A. Kumar. *A simulation study of carbon sequestration in deep saline aquifers*. Master's thesis, The University of Texas at Austin, 2004.

[61] A. Kumar, M. Noh, G. A. Pope, K. Sepehrnoori, S. Bryant, and L. W. Lake. Reservoir simulation of CO_2 storage in deep saline aquifers. Paper SPE 89343 presented at the SPE/DOE Symposium on Improved Oil Recovery, Tulsa, Oklahoma, USA, 2004.

[62] K. S. Lackner. Carbonate chemistry for sequestering fossil carbon. *Annual Review of Energy and the Environment*, 27:193–232, 2002.

[63] K. S. Lackner, C. H. Wendt, D. P. Butt, E. L. Joyce, and D. H. Sharp. Carbon dioxide disposal in carbonate minerals. *Energy*, 20(11):1153–1170, 1995.

[64] L. W. Lake. *Enhanced Oil Recovery*. Prentice Hall, New Jersey, 1989.

[65] P. C. Lichtner. Continuum model for simultaneous chemical reactions and mass transport in hydrothermal systems. *Geochimica et Cosmochimica Acta*, 49(3):779–800, 1985.

[66] P. C. Lichtner. Continuum formulation of multicomponent-multiphase reactive transport. *Reviews in Mineralogy*, 34:1–81, 1996.

[67] P. C. Lichtner, G. E. Hammond, C. Lu, S. Karra, G. Bisht, B. Andre, R. Mills, and J. Kumar. PFLOTRAN user manual. 2015.

[68] E. Liteanu and C. J. Spiers. Influence of pore fluid salt content on compaction creep of calcite aggregates in the presence of supercritical CO_2. *Chemical Geology*, 265(12):134 – 147, 2009.

[69] J. Lu, A. Goudarzi, P. Chen, D. H. Kim, C. Britton, M. Delshad, K. K. Mohanty, U. P. Weerasooriya, and G. A. Pope. Surfactant enhanced oil recovery from naturally fractured reservoirs. Paper SPE 159979 presented at the SPE Annual Technical Conference and Exhibition, San Antonio, Texas, USA, 2012.

[70] A. H. Macdonald and W. S. Fyfe. Rate of serpentinization in seafloor environments. *Tectonophysics*, 116(12):123–135, 1985.

[71] K. Maher, C. I. Steefel, D. J. DePaolo, and B. E. Viani. The mineral dissolution rate conundrum: Insights from reactive transport modeling of U isotopes and pore fluid chemistry in marine sediments. *Geochimica*, 70:337–363, 2006.

[72] C. E. Manning and S. E. Ingebritsen. Permeability of the continental crust: Implications of geothermal data and metamorphic systems. *Reviews of Geophysics*, 37:127–150, 1999.

[73] J. M. Matter and P. B. Kelemen. Permanent storage of carbon dioxide in geological reservoirs by mineral carbonation. *Nature Geoscience*, 2(12):837–841, 2009.

[74] C. M. Mayer, E. O. Frind, and D. W. Blowes. Multicomponent reactive transport modeling in variably saturated media using a generalized formulation for kinetically controlled reactions. *Water Resources Research*, 38(9):1174, 2002.

[75] M. W. McClure and R. N. Horne. An investigation of stimulation mechanisms in enhanced geothermal systems. *International Journal of Rock Mechanics and Mining Sciences*, 72:242–260, 2014.

[76] M. L. Michelsen. The isothermal flash problem. Part I. Stability. *Fluid Phase Equilibria*, 9(1):1–19, 1982.

[77] S. Molins, J. Carrera, C. Ayora, and M. W. Saaltink. A formulation for decoupling components in reactive transport problems. *Water Resources Research*, 40(10):1–13, 2004.

[78] L. Nghiem, P. Sammon, J. Grabenstetter, and H. Ohkuma. Modeling CO_2 storage in aquifers with a fully-coupled geochemical EOS compositional simulator. Paper SPE 89474 presented at the SPE/DOE Symposium on Improved Oil Recovery, Tulsa, Oklahoma, USA, 2004.

[79] L. Nghiem, V. Shrivastava, and B. Kohse. Modeling aqueous phase behavior and chemical reactions in compositional simulation. Paper SPE 141417 presented at the SPE Reservoir Simulation Symposium, The Woodlands, Texas, USA, 2011.

[80] L. X. Nghiem, D. K. Fong, and K. Aziz. Compositional modeling with an equation of state. *Society of Petroleum Engineers Journal*, 21(6):687–698, 1981.

[81] A. Nicolas, F. Boudier, B. Ildefonse, and E. Ball. Accretion of Oman and United Arab Emirates ophiolite – Discussion of a new structural map. *Marine Geophysical Researches*, 21(3-4):147–179, 2000.

[82] E. H. Oelkers. General kinetic description of multioxide silicate mineral and glass dissolution. *Geochimica et Cosmochimica Acta*, 65(21):3703–3719, 2001.

[83] E. H. Oelkers, S. R. Gislason, and J. Matter. Mineral carbonation of CO_2. *Elements*, 4(5):333–337, 2008.

[84] E. H. Oelkers and J. Schott. An experimental study of enstatite dissolution rates as a function of pH, temperature, and aqueous Mg and Si concentration, and the mechanism of pyroxene/pyroxenoid dissolution. *Geochimica et Cosmochimica Acta*, 65(8):1219–1231, 2001.

[85] A. A. Olajire. A review of mineral carbonation technology in sequestration of CO_2. *Journal of Petroleum Science and Engineering*, 109:364–392, 2013.

[86] D. R. Olander. Simultaneous mass transfer and equilibrium chemical reaction. *American Institute of Chemical Engineers Journal*, 6(2):233–239, 1960.

[87] J. L. Palandri and Y. K. Kharaka. A compilation of rate parameters of water-mineral interaction kinetics for application to geochemical modeling. *U.S. Geological Survey Open File Report*, 2004.

[88] A. N. Paukert, J. M. Matter, P. B. Kelemen, E. L. Shock, and J. R. Havig. Reaction path modeling of enhanced in situ CO_2 mineralization for carbon sequestration in the peridotite of the Samail Ophiolite, Sultanate of Oman. *Chemical Geology*, 330-331:86–100, 2012.

[89] D. Y. Peng and D. B. Robinson. A new two–constant equation of state. *Industrial & Engineering Chemistry Fundamentals*, 15(1):59–64, 1976.

[90] G. A. Pope, L. W. Lake, and K. Sepehrnoori. Modelling and scale-up of chemical flooding. *U.S. Department of Energy, Bartlesville Project Office*, Technical Report, 1990.

[91] I. M. Power, A. L. Harrison, G. M. Dipple, S. A. Wilson, P. B. Kelemen, M. Hitch, and G. Southam. Carbon mineralization: from natural analogues to engineered systems. *Reviews in Mineralogy and Geochemistry*, 77:305–360, 2013.

[92] I. M. Power, S. A. Wilson, and G. M. Dipple. Serpentinite carbonation for CO_2 sequestration. *Elements*, 9(2):115–121, 2013.

[93] K. Pruess and N. Müller. Formation dry-out from CO_2 injection into saline aquifers: 1. Effects of solids precipitation and their mitigation. *Water Resources Research*, 45(3):1–11, 2009.

[94] K. Pruess, C. Oldenburg, and G. Moridis. TOUGH2 user's guide, version 2.0. 1999.

[95] K. Pruess and N. Spycher. ECO2N - a new TOUGH2 fluid property module for studies of CO_2 storage in saline aquifers. Presented at the TOUGH Symposium, Berkeley, California, USA, 2006.

[96] B. A. Robinson, H. S. Viswanathan, and A. J. Valocchi. Efficient numerical techniques for modeling multicomponent ground-water transport based upon

simultaneous solution of strongly coupled subsets of chemical components. *Advances in Water Resources*, 23(4):307–324, 2000.

[97] M. Roshanfekr, R. T. Johns, G. Pope, L. Britton, H. Linnemeyer, C. Britton, and A. Vyssotski. Simulation of the effect of pressure and solution gas on oil recovery from surfactant/polymer floods. *Society of Petroleum Engineers Journal*, 17(3):705–716, 2012.

[98] J. Rubin. Transport of reacting solutes in porous media: relation between mathematical nature of problem formulation and chemical nature of reactions. *Water Resources Research*, 19(5):1231–1252, 1983.

[99] M. W. Saaltink, J. Carrera, and C. Ayora. On the behavior of approaches to simulate reactive transport. *Journal of Contaminant Hydrology*, 48(3-4):213–235, 2001.

[100] G. D. Saldi, G. Jordan, J. Schott, and E. H. Oelkers. Magnesite growth rates as a function of temperature and saturation state. *Geochimica et Cosmochimica Acta*, 73(13):5646–5657, 2009.

[101] J. Schott, O. S. Pokrovsky, and E. H. Oelkers. The link between mineral dissolution/precipitation kinetics and solution chemistry. *Reviews in Mineralogy and Geochemistry*, 70:207–258, 2009.

[102] W. Seifritz. CO_2 disposal by means of silicates. *Nature*, 345(6275):486, 1990.

[103] S. D. Sevougian, R. S. Schechter, and L.W. Lake. Effect of partial local equilibrium on the propagation of precipitation/dissolution waves. *Industrial and Engineering Chemistry Research*, 32:2281–2304, 1993.

[104] A. Shahbazi and M. Pooladi-Darvish. Application of operator-splitting technique in numerical simulation of gas-hydrate reservoirs. *Society of Petroleum Engineers Journal*, 18(06):1067–1080, 2013.

[105] S. Solomon, D. Qin, M. Manning, Z. Chen, M. Marquis, K. B. Averyt, M. Tignor, and H. L. Miller. Climate change 2007: The physical science basis, contribution of Working Group I to the Fourth Assessment Report of the Intergovernmental Panel on Climate Change. Cambridge University Press, 2007.

[106] R. Span and W. Wagner. A new equation of state for carbon dioxide covering the fluid region from the triple point temperature to 1100 K at pressures up to 800 MPa. *Journal of Physical and Chemical Reference Data*, 25:1509–1596, 1996.

[107] P. Sriyanong. *Element-based formulations for coupled flow, transport, and chemical reactions*. Master's thesis, Stanford University, 2013.

[108] C. I. Steefel, D. J. DePaolo, and P. C. Lichtner. Reactive transport modeling: An essential tool and a new research approach for the Earth sciences. *Earth and Planetary Science Letters*, 240:539–558, 2005.

[109] C. I. Steefel and K. T. B. MacQuarrie. Approaches to modeling reactive transport in porous media. *Reviews in Mineralogy*, 34:83–125, 1996.

[110] C. I. Steefel and K. T. B. MacQuarrie. CrunchFlow: Software for modeling multicomponent reactive flow and transport. User's Manual, 2009.

[111] C. I. Steefel and K. Maher. Fluid-rock interaction: A reactive transport approach. *Reviews in Mineralogy and Geochemistry*, 70(1):485–532, 2009.

[112] C. I. Steefel, S. B. Yabusaki, and K. U. Mayer. Reactive transport benchmarks for subsurface environmental simulation. *Computational Geosciences*, 19(3):439–443, 2015.

[113] G. Strang. *Linear Algebra and its Applications*. 2006.

[114] E. Tenthorey, C. H. Scholz, E. Aharonov, and A. Léger. Precipitation sealing and diagenesis: 1. Experimental results. *Journal of Geophysical Research: Solid Earth*, 103(B10):23951–23967, 1998.

[115] A. Verma and K. Pruess. Thermohydrological conditions and silica redistribution near high-level nuclear wastes emplaced in saturated geological formations. *Geochimica*, 93:1159–1173, 1988.

[116] S. Vialle, J. L. Druhan, and K. Maher. Multi-phase flow simulation of CO_2 leakage through a fractured caprock in response to mitigation strategies. *International Journal of Greenhouse Gas Control*, 44:11–25, 2016.

[117] H. Vinegar. Shell's in-situ conversion process. Presented at the 26th Oil Shale Symposium, Golden, Colorado, USA, 2006.

[118] D. Voskov. An extended natural variable formulation for compositional simulation based on tie-line parameterization. *Transport in Porous Media*, 92:541–557, 2012.

[119] D. V. Voskov and H. A. Tchelepi. Comparison of nonlinear formulations for two-phase multi-component EoS based simulation. *Journal of Petroleum Science and Engineering*, 82-83:101–111, 2012.

[120] D. V. Voskov, R. Younis, and H. A. Tchelepi. General nonlinear solution strategies for multiphase multicomponent EoS based simulation. *Journal of Petroleum Science and Engineering*, 82-83:101–111, 2009.

[121] P. Wang, I. Yotov, M. Wheeler, T. Arbogast, C. Dawson, M. Parashar, and K. Sepehrnoori. A new generation EOS compositional reservoir simulator: Part I - Formulation and discretization. Paper SPE 37979 presented at the SPE Reservoir Simulation Symposium, Dallas, Texas, USA, 1997.

[122] J. W. Watts. A compositional formulation of the pressure and saturation equations. *SPE Reservoir Engineering*, 1(3):243–252, 1986.

[123] T. J. Wolery. EQ3NR, a computer program for geochemical aqueous speciation-solubility calculations : Theoretical manual, user's guide, and related documentation (version 7.0). *Lawrence Livermore National Laboratory*, 1992.

[124] T. W. Wolery and R. L. Jarek. Software user's manual EQ3/6, version 8.0. *Sandia National Lab*, 2003.

[125] Y. S. Wu, K. Zhang, and H. H. Liu. Estimating large-scale fracture permeability of unsaturated rock using barometric pressure data. *Vadose Zone Journal*, 5:1129–1142, 2006.

[126] T. Xu, J. A. Apps, and K. Pruess. Reactive geochemical transport simulation to study mineral trapping for CO_2 disposal in deep arenaceous formations. *Journal of Geophysical Research*, 108(B2), 2003.

[127] T. Xu, J. A. Apps, and K. Pruess. Numerical simulation of CO_2 disposal by mineral trapping in deep aquifers. *Applied Geochemistry*, 19(6):917–936, 2004.

[128] T. Xu, F. Gérard, K. Pruess, and G. Brimhall. Modeling non-isothermal multiphase multi-species reactive chemical transport in geologic media. *Lawrence Berkeley National Laboratory*, Technical Report, 1997.

[129] T. Xu and K. Pruess. Coupled modeling of non-isothermal multiphase flow, solute transport and reactive chemistry in porous and fractured media: 1. Model development and validation. *Lawrence Berkeley National Laboratory*, 1998.

[130] T. Xu and K. Pruess. Modeling multiphase non-isothermal fluid flow and reactive geochemical transport in variably saturated fractured rocks: 1. Methodology. *American Journal of Science*, 301:16–31, 2001.

[131] T. Xu, N. Spycher, E. Sonnenthal, L. Zheng, and K. Pruess. TOUGHREACT user's guide: A simulation program for non-isothermal multiphase reactive transport in variably saturated geologic media, version 2.0. *Lawrence Berkeley National Laboratory*, 2012.

[132] G. Yeh and V. S. Tripathi. A model for simulating transport of reactive multispecies components: Model development and demonstration. *Water Resources Research*, 27(12):3075–3094, 1991.

[133] L. C. Young and R. E. Stephenson. A generalized compositional approach for reservoir simulation. *Society of Petroleum Engineers Journal*, 23(5):727–742, 1983.

[134] R. Younis and K. Aziz. Parallel automatically differentiable data-types for next-generation simulator development. Paper SPE 106493 presented at the SPE Reservoir Simulation Symposium, Houston, Texas, USA, 2007.

[135] R. M. Younis. *Modern advances in software and solution algorithms for reservoir simulation*. PhD thesis, Stanford University, 2011.

Appendix A

Chemical reaction modeling

The description of aqueous systems, such as those relevant for CO_2 sequestration in saline aquifers, often involves a large number of equilibrium reactions and species. The geochemistry community takes advantage of the many equilibrium constraints to develop concise representations for large sets of species. In compositional reservoir simulation, on the other hand, the common practice is to represent hydrocarbon systems containing tens or hundreds of species using a limited number of so-called pseudo-species. Generally, no equilibrium reactions involving these pseudo-species are considered, making the problem in reservoir engineering very different from those posed in the geochemistry community. Accommodating the geochemistry conventions is thus not always appropriate for general purpose reservoir simulation. As seen later in this appendix, an equivalent approach has been used to treat equilibrium reactions in this field [26, 79].

A.1 Reaction treatment in carbon storage

In the following, we briefly describe chemical reaction modeling with special attention to the problem of CO_2 sequestration in saline aquifers.

A.1.1 Activity

Activity is a dimensionless quantity introduced to account for departure from ideality. In analogy to the concept of fugacity, the chemical potential for a species in a solution is expressed in terms of activity:

$$\mu_c = \mu_c^0 + RT \ln(a_c), \tag{A.1}$$

where μ_c is the chemical potential of species c, R is the gas constant, T is absolute temperature, a_c is the activity of species c in the solution, and superscript 0 denotes the standard state [59].

Activity is dimensionless by definition, and is expressed as:

$$a_c = \gamma_c \, m_c, \tag{A.2}$$

where m_c is molality and γ_c is the activity coefficient, which accounts for nonideal behavior. Molality is defined as $m_c = 55.508 \, x_c/x_w$, where x_c and x_w are molar fractions of species c and water, and 55.508 is the number of moles per kilogram for pure water. In very dilute solutions $\gamma_c \longrightarrow 1$ and $a_c \longrightarrow m_c$. The activity of the solvent in the aqueous phase (H_2O) is set to unity for our dilute solutions [124]. The activity of minerals is also assumed to be unity.

The usual sources of nonideality in electrolyte solutions, which result in non-unit activity coefficients, are electrical interactions [123]. Ionic strength, which quantifies the relevant effect, is defined as:

$$I = \frac{1}{2} \sum_{i=1}^{n_c} m_{i,w} Z_i^2, \tag{A.3}$$

where $m_{i,w}$ and Z_i are the molality and charge of the aqueous species i. It has been observed empirically that ionic strength provides a reasonable estimate of the influence of charged species on solubility, and that the solubility of salts is roughly proportional to the square root of ionic strength [59].

As in Fan et al. [28], we use the B-dot equation of Helgeson for electrically charged

species [46]:

$$\log\ \gamma_c = -\frac{A_\gamma\, Z_c^2 \sqrt{I}}{1 + \overset{o}{a}_c B_\gamma \sqrt{I}} + \dot{B} I, \tag{A.4}$$

where A_γ and B_γ are Debye-Hückel A and B parameters, $\dot{B}$ is the characteristic B-dot parameter, $\overset{o}{a}_c$ is the ion size of species c, and Z_c is the ion electrical charge for species c. The quantities A, B, and $\dot{B}$ are temperature-dependent constants, and are extracted from the EQ3 database [124].

A.1.2 Equilibrium reaction modeling

Reversible and sufficiently fast reactions are assumed to reach equilibrium instantaneously and are modeled through chemical equilibrium constraints. Consider the equilibrium reaction $\sum_{i=1}^{n_c} \upsilon_i A_i = 0$, where A_i denotes the species chemical formula (e.g., CO_2), and υ_i is the corresponding stoichiometric coefficient. The mass action law statement for this equilibrium reaction is $\prod_i a_i^{\upsilon_i} = K^{eq}$. The introduction of the ion activity product, Q, where $Q = \prod_i a_i^{\upsilon_i}$, gives the more familiar form of the equilibrium constraint; namely $Q - K^{eq} = 0$.

In the context of CO_2 sequestration, homogeneous reactions (among aqueous species) are modeled as equilibrium reactions. In contrast, the heterogeneous mineral dissolution/precipitation reactions progress at much slower rates and are modeled kinetically, as discussed in the following section.

A.1.3 Kinetics of mineral precipitation and dissolution

Most mineral dissolution and precipitation reactions have strong pH dependence at conditions far from equilibrium. Usually the three acid, neutral, and base mechanisms are observed in parallel, and the overall reaction rate law is obtained through the combination [87, 110]:

$$r_k = A \sum_\alpha k_\alpha a_{H^+}^{m_\alpha} \left(1 - \Omega^{p_\alpha}\right)^{q_\alpha} \quad , \quad \alpha = a, n, b, \tag{A.5}$$

where A is the mineral surface area, k_a, k_n and k_b are kinetic rate constants for the acid, neutral, and base mechanisms, a_{H^+} is the activity of H^+, and m_α, p_α, and q_α are

experimentally-determined exponents, with m_n usually taken to be zero. The mineral saturation index, Ω, is defined as $\Omega = Q/K^{eq}$, where K^{eq} is the mineral equilibrium constant. The kinetic rate constants are calculated based on the values at a reference temperature, T_{ref}, using the Arrhenius equation:

$$k_\alpha = k_\alpha^{T_{ref}} \exp\left(\frac{-E_\alpha}{R}\left(\frac{1}{T} - \frac{1}{T_{ref}}\right)\right), \quad \alpha = a, n, b, \tag{A.6}$$

where $k_\alpha^{T_{ref}}$ is the pre-exponential factor, E_α is the activation energy, R is the gas constant, and T is absolute temperature.

A.2 Reaction stoichiometry and equilibrium reaction modeling

In reactive transport frameworks, the equilibrium rate annihilation (**E**) matrix, derived from the canonical stoichiometric matrix of the set (or subset) of independent reactions, facilitates the treatment of equilibrium reactions. This matrix, a special form of which was proposed in Fan et al. [28], is defined such that, when applied to the mass balance equations, it eliminates the influence of the equilibrium reactions. We now motivate and describe the general approach for the derivation of the equilibrium rate annihilation matrix, and its connection to 'components' in the geochemistry literature. Note that we adopt the terms component and noncomponent to address the sets of independent and dependent variables as defined in the geochemistry literature.

A.2.1 Properties of the stoichiometry matrix

Consider the set of reactions:

$$\sum_{i=1}^{n_s} \upsilon_{ij} A_i = 0, \quad (j = 1, \cdots, n_r), \tag{A.7}$$

where A_i indicates a species chemical formula (e.g., CH_4, H_2O or CO_2) and υ_{ij} is the stoichiometric coefficient of species i in reaction j, n_s is the number of species, and

n_r is the number of reactions. Rewriting Eq. (A.7) in matrix-vector format gives:

$$\mathbf{S}^T\ \mathbf{A}\ = \mathbf{0}, \tag{A.8}$$

where $\mathbf{S}$ is the stoichiometry matrix. Each row of $\mathbf{S}^T$ corresponds to a reaction, and each column to a species.

The formula matrix $\mathbf{F}$ is an $n_e \times n_s$ matrix, where n_e is the smallest (non-redundant) number of elements from which the species are formed. An element may be defined as an atom (e.g., H, O), or a compound (e.g., -CH_3, -SiO_2) that does not partition into smaller entities by chemical reactions in the system under consideration. Each column of $\mathbf{F}$ describes the chemical composition of a species in terms of its constituent elements. As an example, consider the reaction system in Table A.1. The matrix form

Table A.1: Chemical system describing calcite dissolution with eight species and four independent reactions.

Reaction #	Type	Reactions
1	Kinetic	$CaCO_3 \longrightarrow Ca^{2+} + {CO_3}^{2-}$
2	Equilibrium	$CO_2 + H_2O = H^+ + {HCO_3}^-$
3	Equilibrium	${HCO_3}^- = H^+ + {CO_3}^{2-}$
4	Equilibrium	$H_2O = H^+ + OH^-$

of the reactions and the formula matrix can be written as follow:

$$\mathbf{S}^T\ \mathbf{A} = \begin{bmatrix} -1 & 1 & 0 & 0 & 1 & 0 & 0 & 0 \\ 0 & 0 & -1 & 1 & 0 & -1 & 1 & 0 \\ 0 & 0 & 0 & -1 & 1 & 0 & 1 & 0 \\ 0 & 0 & 0 & 0 & 0 & -1 & 1 & 1 \end{bmatrix} \begin{bmatrix} CaCO_3 \\ Ca^{2+} \\ CO_2 \\ {HCO_3}^- \\ {CO_3}^{2-} \\ H_2O \\ H^+ \\ OH^- \end{bmatrix} = \mathbf{0}, \tag{A.9}$$

$$\mathbf{F} = \begin{array}{c} \\ \text{C} \\ \text{H} \\ \text{O} \\ \text{Ca} \end{array} \begin{array}{c} \begin{array}{cccccccc} \text{CaCO}_3 & \text{Ca}^{2+} & \text{CO}_2 & \text{HCO}_3^- & \text{CO}_3^{2-} & \text{H}_2\text{O} & \text{H}^+ & \text{OH}^- \end{array} \\ \left[\begin{array}{cccccccc} 1 & 0 & 1 & 1 & 1 & 0 & 0 & 0 \\ 0 & 0 & 0 & 1 & 0 & 2 & 1 & 1 \\ 3 & 0 & 2 & 3 & 3 & 1 & 0 & 1 \\ 1 & 1 & 0 & 0 & 0 & 0 & 0 & 0 \end{array}\right] \end{array}. \tag{A.10}$$

Intuitively, we can see that $n_e \leq n_s$ [103]. By definition, the formula matrix must fully encompass the elements involved in all species and be non-redundant. Consequently, n_e is the dimension of the vector space spanned by the columns of the formula matrix. It follows that the rows of $\mathbf{F}$ are linearly independent. Once a particular $\mathbf{F}$ is defined, premultiplying it by any nonsingular $n_e \times n_e$ matrix yields an alternative matrix. The element mass balance imposed across individual reactions implies that:

$$\mathbf{F} \times \mathbf{S} = \mathbf{0}_{n_e \times n_r}, \tag{A.11}$$

where $0_{i,j}$ corresponds to the balance of element i in reaction j. The stoichiometric coefficient matrix $\mathbf{S}$ belongs to the null space of the formula matrix. Consequently, to have linearly independent reactions (in order to be physical), the columns of $\mathbf{S}$ must span the null space of $\mathbf{F}$. The null space of $\mathbf{F}$ is thus considered the stoichiometric subspace, or the reaction subspace [6]. Based on the fundamental theorem of linear algebra, the null space of a full-rank matrix $\mathbf{F}$ has dimensions of $n_s - n_e$, since $\text{rank}(\mathbf{F}) = n_e$ [113]; thus a maximum of $n_r = n_s - n_e$ reactions can exist among these species, either kinetic or equilibrium. These criteria allow for the validation of the consistency of the physical and reaction constraints. In practice, the complete set of reactions need not be employed, and any appropriate subset is mathematically acceptable.

A.2.2 Equilibrium rate annihilation matrix

The classification of the species into components and noncomponents is closely related to the derivation of the so-called equilibrium rate annihilation matrix, as we now demonstrate. The stoichiometry matrix, $\mathbf{S}$, can be arranged such that the first n_k columns represent kinetic reactions, followed by n_q columns modeling equilibrium

reactions. As shown later, $\mathbf{S}$ can be further algebraically reduced to its canonical form, $\bar{\mathbf{S}}$, [65]:

$$\bar{\mathbf{S}} = \left[\begin{array}{cc} \bar{\mathbf{S}}_{k,n_s \times n_k} & \bar{\mathbf{S}}_{q,n_s \times n_q} \end{array} \right] = \left[\begin{array}{cc} \mathbf{A}_{(n_s-n_q)\times n_k} & \mathbf{C}_{(n_s-n_q)\times n_q} \\ \mathbf{0}_{n_q \times n_k} & -\mathbf{I}_{n_q} \end{array} \right]_{n_s \times (n_q+n_k)}, \quad \text{(A.12)}$$

where $\bar{\mathbf{S}}_k$ and $\bar{\mathbf{S}}_q$ are the canonical kinetic and equilibrium stoichiometry matrices respectively, and $\mathbf{I}$ is the identity matrix. In this canonical form, each equilibrium reaction corresponds to a single species that is not involved in any other reaction. These species constitute the noncomponents. The derivation of components is more involved, as we now describe.

By definition, the equilibrium rate annihilation matrix, $\mathbf{E}$, must eliminate the influence (rate) of equilibrium reactions from the mass balance equations, i.e., $\mathbf{E} \times \bar{\mathbf{S}}_q = \mathbf{E} \times \mathbf{S}_q = \mathbf{0}$. Without loss of generality, the equilibrium reactions may be assumed linearly independent, resulting in a full-rank $\bar{\mathbf{S}}_q$ of rank n_q. This implies that the null space of $\mathbf{E}$ is an n_q-dimensional space, and $\mathbf{E}$ is of rank $n_s - n_q$. Once a matrix $\mathbf{E}$ is found, any matrix consisting of $n_s - n_q$ linearly independent rows in the vector space spanned by rows of $\mathbf{E}$ can serve as the equilibrium rate annihilation matrix. In other words, premultiplying an instance of $\mathbf{E}$ by any nonsingular $(n_s - n_q) \times (n_s - n_q)$ matrix yields another valid $\mathbf{E}$. A straightforward definition of $\mathbf{E}$ is as follows:

$$\mathbf{E} = \left[\begin{array}{cc} -\mathbf{I}_{n_s-n_q} & -\mathbf{C}_{(n_s-n_q)\times n_q} \end{array} \right]. \quad \text{(A.13)}$$

If $\mathbf{c}$ is the vector of n_s species, $\mathbf{u} = \mathbf{E} \times \mathbf{c}$ is the vector of $n_s - n_q$ components. The components are thus (a set of non-unique) linear combinations of the physical species and their definition is closely related to the choice of the $\mathbf{E}$ matrix. For example, the $\mathbf{E}$ matrix can be prescribed in terms of the formula matrix, as discussed in Fan et al. [28], yielding the element balance formulation where components are the elements .

Consider a groundwater software package which expresses the mass balance equations in terms of a specific set of components, $\mathbf{u}^*$. If a reservoir engineering simulator uses the corresponding equilibrium rate annihilation matrix, $\mathbf{E}^*$, to transform species

mass conservation equations, the final mass balance equations will be exactly the same in the two formulations. Moreover, the (component) mass balance equations are equivalent even for different choices of component sets and $\mathbf{E}$ matrices, as they all represent the same nonlinear problem.

A.2.3 Derivation of the canonical stoichiometry matrix

The canonical form of the stoichiometric matrix is central in defining the equilibrium rate annihilation matrix. Its derivation is thus addressed in this section. Most reaction sets are simple enough that the canonical form of $\mathbf{S}_q$ can be derived simply by rearranging the equations of the mass action laws governing the equilibrium reactions. A more general approach, applicable to more complex reaction sets, is described in the following.

Matrix $\mathbf{S}^T$ is arranged following our previous conventions: the top n_k rows represent kinetic reactions, followed by n_q rows corresponding to the equilibrium reactions:

$$\mathbf{S}^T = \begin{bmatrix} \mathbf{X}_{n_k \times (n_s - n_q)} & \mathbf{Y}_{n_k \times n_q} \\ \mathbf{W}_{n_q \times (n_s - n_q)} & \mathbf{Z}_{n_q \times n_q} \end{bmatrix}. \tag{A.14}$$

For any arbitrary set of reactions, $\mathbf{S}^T$ can be reduced to its canonical form, $\bar{\mathbf{S}}^T$, through the following (premultiplication) operations:

$$\begin{bmatrix} -\mathbf{I}_{n_k} & -\mathbf{Y}_{n_k \times n_q} \\ \mathbf{0} & \mathbf{I}_{n_q} \end{bmatrix} \begin{bmatrix} \mathbf{I}_{n_k} & \mathbf{0} \\ \mathbf{0} & -\mathbf{Z}^{-1}_{n_q \times nq} \end{bmatrix} \begin{bmatrix} \mathbf{X} & \mathbf{Y} \\ \mathbf{W} & \mathbf{Z} \end{bmatrix} = - \begin{bmatrix} \mathbf{X} - \mathbf{Y}\mathbf{Z}^{-1}\mathbf{W} & \mathbf{0} \\ \mathbf{Z}^{-1}\mathbf{W} & \mathbf{I} \end{bmatrix}. \tag{A.15}$$

Note that this transformation operates on the rows of $\mathbf{S}^T$, framing the chemical reaction phenomena in terms of a new reaction set. It does not, however, influence the ordering or nature of the columns of $\mathbf{S}^T$ corresponding to the n_s physical species.

On closer inspection, the linear operations performed in Eq. (A.15) are equivalent to

finding a Schur complement, a transformation commonly utilized in reservoir simulation to decouple local equations from the global system at the level of the Jacobian matrix. Since this Schur reduction algorithm is readily available in most compositional simulators, the conversion of the stoichiometric matrix to its canonical form is straightforward.

A slightly different form of the canonical stoichiometric matrix is used in Section 2.1.2, the derivation of which involves an extra step. The $\bar{\mathbf{S}}^T$ matrix from Eq. (A.15) can be re-written as:

$$\bar{\mathbf{S}}^T = \begin{bmatrix} \bar{\mathbf{X}}_{1,n_k\times(n_s-n_q-n_k)} & \bar{\mathbf{X}}_{2,n_k\times n_k} & \mathbf{0}_{n_k\times n_q} \\ \bar{\mathbf{W}}_{1,n_q\times(n_s-n_q-n_k)} & \bar{\mathbf{W}}_{2,n_q\times n_k} & -\mathbf{I}_{n_q} \end{bmatrix}. \tag{A.16}$$

An additional linear transformation will yield the matrix format used in Section 2.1.2:

$$\begin{aligned} \bar{\mathbf{S}}^{'T} &= \begin{bmatrix} -\bar{\mathbf{X}}^{-1}_{2,n_k\times n_k} & \mathbf{0} \\ \mathbf{0} & \mathbf{I}_{n_q} \end{bmatrix} \begin{bmatrix} \bar{\mathbf{X}}_1 & \bar{\mathbf{X}}_2 & \mathbf{0} \\ \bar{\mathbf{W}}_1 & \bar{\mathbf{W}}_2 & -\mathbf{I}_{n_q} \end{bmatrix} \\ &= \begin{bmatrix} -\bar{\mathbf{X}}_2^{-1}\bar{\mathbf{X}}_1 & -\mathbf{I}_{n_k} & \mathbf{0} \\ \bar{\mathbf{W}}_1 & \bar{\mathbf{W}}_2 & -\mathbf{I}_{n_q} \end{bmatrix}. \end{aligned} \tag{A.17}$$

Note that the ordering of the species may be modified at any stage to ensure that $\mathbf{Z}$ and $\bar{\mathbf{X}}_2$ are not singular.

Appendix B

Porosity and permeability change

The dissolution and precipitation of minerals change the rock volume and consequently impact porosity and permeability. Modeling this phenomenon may be important in certain applications, especially because potentially significant permeability variations can occur despite small changes in mineral volume. Porosity is usually adjusted based on volumetric criteria, and permeability is expressed as a function of porosity. Numerous correlations have been established, which differ from one another, in part, because of different pore scale properties, e.g., pore and connectivity geometries [115]. However, besides the inherent differences in the rocks, the mechanism under which the porosity change occurs also dictates its impact on permeability. Porosity changes due to stress are likely to be experienced chiefly in pore bodies. In contrast, a more dramatic impact on permeability may be observed under mineral precipitation if the pore throats become blocked. In the following, we propose a framework to integrate these effects in a compositional simulator.

B.1 Single compressibility factor

The bulk volume, V_b, may be divided into three parts, namely pore, reactive solid, and nonreactive solid volumes. The pore space contains the fluid, the reactive solid volume accounts purely for the volumes of the minerals involved in reactions, and the

remainder of the solid volume constitutes the nonreactive rock volume. We thus have

$$V_b = \left(V_{nr} + V_r + V_\phi\right)_p , \tag{B.1}$$

where V_{nr}, V_r, and V_ϕ are the nonreactive solid, reactive solid, and pore volumes respectively, and p indicates pressure. At constant pressure, the nonreactive solid volume is constant, and the pore space changes due to variations in the reactive solid volume only.

By definition:

$$V_r = \sum_{i=1}^{n_m} V_{r,i} = V_b \sum_{i=1}^{n_m} \frac{C_i}{\rho_i^m}, \tag{B.2}$$

where $V_{r,i}$ is the volume of (reactive) mineral i, n_m is the number of (reactive) minerals, C_i is the concentration of mineral i (mass per bulk volume), and ρ_i^m is the density of mineral i (mass per mineral volume). Following the nomenclature in Verma and Pruess [115], we introduce the total porosity, $\tilde{\phi}$, as the sum of fluid-filled (active) porosity and the reactive solid-filled porosity,

$$\tilde{\phi} = \phi + \phi_r = \frac{V_r}{V_b} + \frac{V_\phi}{V_b}. \tag{B.3}$$

Mineral saturation, S_i^m, is assigned with respect to the total porosity:

$$S_i^m = \frac{V_{r,i}}{\tilde{\phi} V_b} = \frac{1}{\tilde{\phi}} \frac{C_i}{\rho_i^m}, \tag{B.4}$$

and the volume balance statement is expressed as follows:

$$\tilde{\phi} \sum_{i=1}^{n_m} S_i^m + \phi = \tilde{\phi}, \tag{B.5}$$

since $\sum_{i=1}^{n_m} S_i^m = \phi_r / \tilde{\phi}$. Note that S_i continues to represent the saturation of fluid phase i.

By definition, the nonreactive volume at initial conditions and reference pressure,

$V_{nr}(p_{ref})$, is given by:

$$V_{nr,ref} = V_{nr}(p_{ref}) = V_b \left(1 - \phi_0 - \sum_i^{n_m} \frac{C_{i,0}}{\rho_i^m(p_{ref})}\right), \tag{B.6}$$

where ϕ_0 is the initial porosity at reference pressure and $C_{i,0}$ is the initial concentration of mineral i. The bulk volume and nonreactive solid mass of individual grid blocks are constant by definition. As a result, $V_{nr,ref}$ is constant throughout the simulation. It follows that total porosity at reference pressure is also constant:

$$\tilde{\phi}_{ref} = 1 - \frac{V_{nr,ref}}{V_b}. \tag{B.7}$$

In the case of a single, small rock compressibility factor, c_r, for both reactive and nonreactive solid volumes, the pore volume is given as:

$$V_\phi(p) = V_\phi(p_{ref})(1 + c_r(p - p_{ref})), \tag{B.8}$$

where $V_\phi(p)$ is the pore volume at block pressure p. Here $V_\phi(p_{ref}) = V_b\phi_0$ initially and it is calculated as follows subsequently:

$$V_\phi(p_{ref}) = V_b \left(\tilde{\phi}_{ref} - \sum_i^{n_m} \frac{C_i}{\rho_i^m(p_{ref})}\right). \tag{B.9}$$

Note that $\phi = \frac{V_\phi(p)}{V_b}$ at any given time.

If required, the total rock volume may be obtained using

$$(V_{nr} + V_r)_p = V_b - V_\phi(p). \tag{B.10}$$

B.2 Multiple compressibility factors

In this section, we discuss an approach to handle distinct compressibility factors for reactive and nonreactive volumes. The nomenclature is as before, and Eqs. (B.1)-(B.7) continue to apply.

Designating $c_{r,nr}$ as the compressibility factor of the nonreactive solid portion of the rock, and observing that $(V_\phi + V_r)_{P_{ref}} = (V_b - V_{nr})_{P_{ref}}$, we have:

$$(V_\phi + V_r)_p = V_b\tilde{\phi}(1 + c_{r,nr}(p - p_{ref})). \tag{B.11}$$

Also, by definition:

$$V_r(p) = V_b \sum_i^{n_m} \frac{C_i}{\rho_i^m(p)}, \tag{B.12}$$

where $\rho_i^m(p)$ takes into account the compressibility of mineral i. The pore volume is now given as follows:

$$V_\phi(p) = (V_b - V_{nr,ref})(1 + c_{r,nr}(p - p_{ref})) - V_b \sum_i^{n_m} \frac{C_i}{\rho_i^m(p)}. \tag{B.13}$$

B.3 Permeability calculations

Based on the updated porosity, permeability may be obtained from the Carman-Kozeny equation:

$$k = \frac{1}{72\tau} \frac{\phi^3 D_p^2}{(1-\phi)^2}, \tag{B.14}$$

where τ stands for tortuosity and D_p represents the dependence on pore size. Alternatively, in the presence of more information, other approaches can be used. For example, in a fractured medium, statistical approaches may be applied to update matrix and fracture permeability values independently [115, 116].